Advances in Materials Science and Engineering

Materials Behaviors and Characterization of Composite Materials for Automotive Application

Lead Guest Editor: RADHA KRISHNAN B
Guest Editors: Lee Chang Chuan, Vijayan V, and A Parthiban

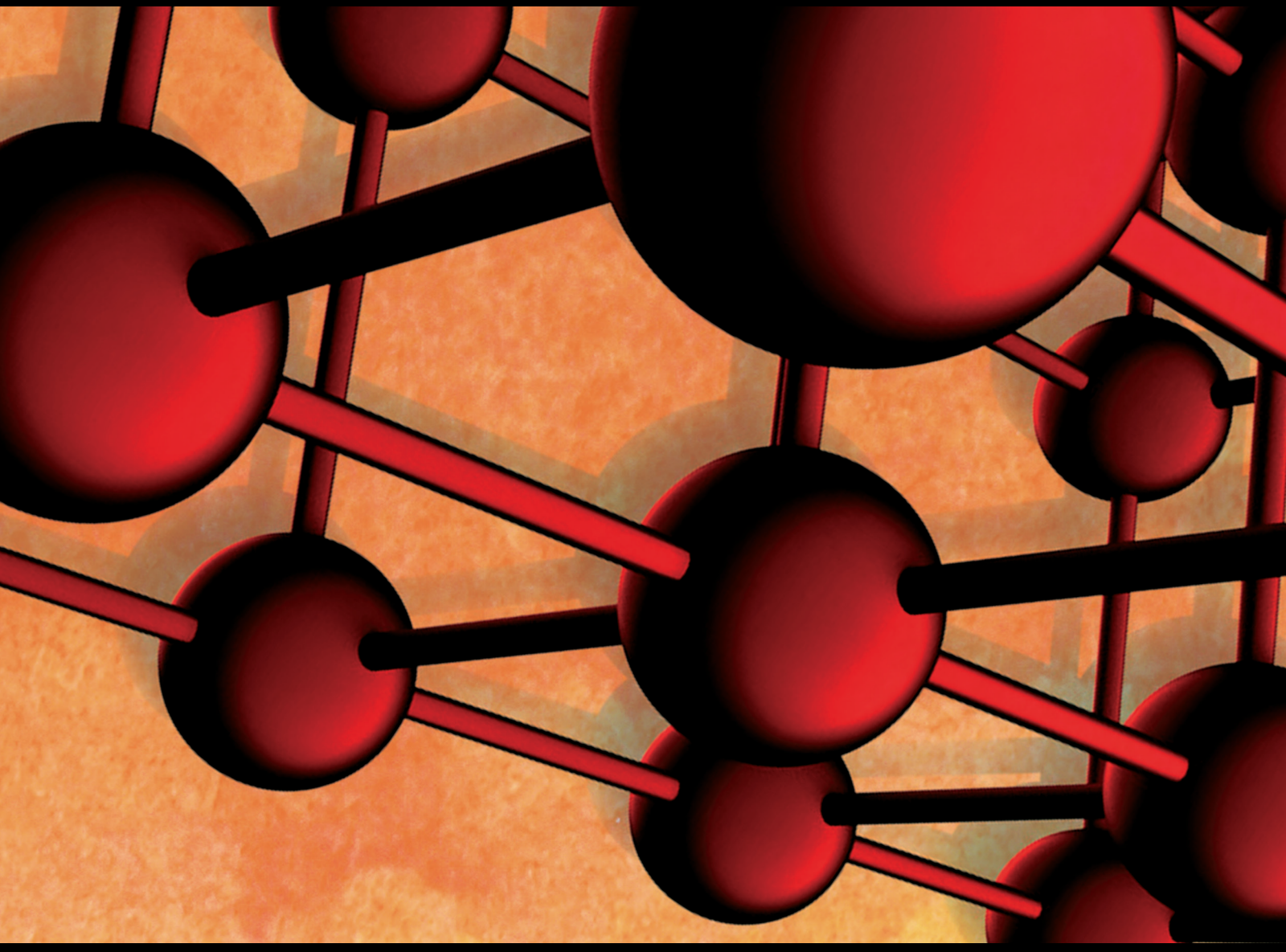

Materials Behaviors and Characterization of Composite Materials for Automotive Application

Advances in Materials Science and Engineering

Materials Behaviors and Characterization of Composite Materials for Automotive Application

Lead Guest Editor: RADHA KRISHNAN B
Guest Editors: Lee Chang Chuan, Vijayan V, and A Parthiban

Contents

Hindawi
Advances in Materials Science and Engineering
Volume 2023, Article ID 5585132, 13 pages
https://doi.org/10.1155/2023/5585132

Research Article

Synthesis and Empirical Analysis of the Thermophysical Characteristics of GO-Ag Aqueous Hybrid Nanofluid Using Environmentally Friendly Reducing and Stabilizing Agents

M. Armstrong,[1] M. Sivasubramanian,[1] N. Selvapalam,[2] R. Pavitra,[2] P. Rajesh Kanna,[3] and Haiter Lenin[4]

[1]*School of Mechanical, Aero, Auto and Civil Engineering, Kalasalingam Academy of Research and Education, Virudhunagar, Tamil Nadu, India*
[2]*School of Advanced Sciences, Kalasalingam Academy of Research and Education, Virudhunagar, Tamil Nadu, India*
[3]*CO_2 Research and Green Technologies Centre, Vellore Institute of Technology, Vellore, Tamil Nadu, India*
[4]*Department of Mechanical Engineering, WOLLO University, Kombolcha Institute of Technology, Post Box No: 208, Kombolcha, Ethiopia*

Correspondence should be addressed to M. Armstrong; mecharmstrong@gmail.com and Haiter Lenin; haiter@kiot.edu.et

Received 20 January 2023; Revised 4 September 2023; Accepted 13 September 2023; Published 4 October 2023

Academic Editor: Ajay Kumar Mishra

The remarkable potential of the carbon allotrope graphene and its derivatives in developing hybrid nanofluids has sparked considerable interest among researchers. These carbon nanoparticles offer excellent opportunities to blend with various metal or metal oxide nanoparticle binders to improve their material properties. This study focuses on investigating the synthesis, characterization, and thermophysical properties of silver- (Ag-) infused GO aqueous hybrid nanofluids with various weight percentages (0.025, 0.05, and 0.1 wt.%) using environmentally friendly reducing and stabilizing agents. Characterization of the hybrid nanofluids was performed using XRD, SEM, EDX, a UV-visible spectrometer, a particle size analyzer, and FTIR techniques. The thermal conductivity and viscosity of the GO-Ag hybrid nanofluids were experimentally determined in the temperature range of 293 K–333 K. Notably, the results indicated that the nanofluids with a concentration of 0.1 wt.% exhibited the most significant enhancement in thermal conductivity, with improvements of 15.22% at 293 K and 31.19% at 333 K compared to the base fluid. A mathematical model was developed based on the thermal conductivity experimental results using the response surface methodology (RSM). Overall, the results suggest that the silver nanoparticles-decorated aqueous graphene oxide hybrid nanofluid has promising potential as an innovative heat transfer fluid in various heat transfer applications.

1. Introduction

The use of graphene-based nanoparticles in both solid metal structures and liquids has created opportunities for various applications such as thermal power generation, clean and renewable energy, heat transfer, electronic cooling, and bioenergy. This is because graphene nanoparticles have better chemical, mechanical, electrical, and thermophysical properties [1–5]. However, there are some challenges associated with graphene nanoparticles, such as difficulties in bulk production and their hydrophobic nature, which leads to low stability with water. These issues led to the development of graphene oxide (GO) as one of the alternatives to graphene. These GO nanoparticles are simple to prepare on a large scale, are cost-effective, have high thermal conductivity, and are hydrophilic towards water molecules, making them an ideal candidate for thermal investigations [1, 6]. To this end, Hajjar et al. [7] studied the thermal conductivity of five different concentrated GO nanofluids (0.05 wt.%–0.25 wt.%) at operating temperatures ranging from 10°C to 40°C. The authors found that at 40°C and 0.25 wt.%, there was a maximum increase in thermal conductivity of 47.54%.

The authors also noted that the thermal conductivity of the GO nanofluid increased with temperature and nanoparticle concentration. In a similar vein, the research conducted by Mei et al. [8] delved into the thermal and rheological characteristics of GO nanofluids with low mass fractions ranging from 0.002% to 0.01% at temperatures between 25°C and 50°C. The authors discovered that at 0.01% and 50°C, the GO nanofluid displayed higher thermal conductivity than other low concentrations. The authors' observations mirrored those of Hajjar et al., and they further reported that an increase in temperature and nanoparticle concentration led to a decrease and increase in nanofluid viscosity, respectively. The literature discussed above indicates that GO nanofluids can substantially enhance the thermal conductivity of base fluids even at low concentrations. GO nanostructures possess multiple characteristics, including a higher surface-to-volume ratio, high charge carrier mobility, high thermal conductivity, tunable porosity and band gap, good catalytic properties as electron acceptors, high elasticity, longer stability duration, and many more, depending on the application requirements [9]. These multiple combinational characteristics make GO nanoparticles suitable for use as mono or hybrid nanoparticles. Several researchers have used GO nanoparticles as a core material and doped them with metal and metal oxide nanoparticles [10–14] to produce novel hybrid nanoparticles or nanofluids. The thermophysical, optical, chemical, and biological properties of the doped nanoparticles were enhanced through this process. For instance, Li et al. [15] prepared an ethylene glycol-based GO-Ag hybrid nanofluid and observed an increase in thermal conductivity of 22% at 45°C with a mass fraction of 0.3 wt.% in the temperature and mass fraction range of 20–45°C and 0.1, 0.2, and 0.3 wt.%, respectively. Later, the researcher Huminic et al. [16] conducted research on a GO-Si aqueous hybrid nanofluid and reported empirical and numerical findings on the nanofluid's viscosity impact at temperatures ranging from 20–50°C. They provided a detailed report indicating that the nanofluid's thermal performance would improve due to the reduction in viscosity at higher temperatures. Singh et al. [17] found a 30% improvement in the thermal conductivity of GO-CuO/DW nanofluids at 0.3 wt.% and 60°C. Taherialekouhi et al. [18] discussed the preparation of aqueous GO-Al_2O_3 hybrid nanofluid at 0.1, 0.25, 0.5, 0.75, and 1% volume fractions from 25–50°C and found 33.9% improvement in the thermal conductivity at 1% and 50°C. The authors also performed mathematical modelling for the experimental thermal conductivity ratio results, influencing the volume fraction and change in temperature of the hybrid nanofluid. El-Shafai et al. [19] investigated the thermal characteristics and ability of ternary GO@CuO/Al_2O_3 hybrid nanofluids in solar applications. The researchers observed a 22.56% improvement in thermal conductivity compared to the aqueous base fluid at 0.2 wt.% and 50°C. As a result, much research has been conducted on using GO as a core material for doping with metal oxides rather than metal nanoparticles and at higher concentrations instead of low concentrations.

This study focuses on the synthesis, characterization, and investigation of the stability and thermophysical characteristics of hybrid nanofluids containing Ag-decorated GO nanoparticles. The nanofluid is prepared with nanoparticle dispersions of less than 0.5 wt.% and at various weight percentages (0.025 wt.%, 0.05 wt.%, 0.1 wt.%) in doubled distilled water (DW). Furthermore, the response surface methodology (RSM) is employed to analyse the experimental thermal conductivity results. The RSM approach is crucial for performing precise regression analysis to forecast the mathematical model using experimental data. Previous studies have used RSM multivariate regression to evaluate the thermal characteristics of different nanofluids associated with input data such as temperatures and weight volume concentrations [20–22].

2. Materials and Procedures

2.1. Graphene Oxide (GO) Nanoparticles Fabrication. In this research, all chemicals purchased were of analytical grade and sourced from Sigma Aldrich, USA; Otto Chemie Private Ltd; Avra Synthesis Private Ltd; and Sisco Research Laboratories Pvt Ltd, India. The graphene oxide nanoparticles were synthesized using Hummer's modified approach [12, 23]. Initially, 3 grams of natural graphite flakes were combined with 3 grams of $NaNO_3$ in a purified 500 mL round-bottom flask. Then, 90 mL of concentrated H_2SO_4 was added with vigorous agitation at 0–5°C. After 3 to 4 hours, 12 g of solid $KMnO_4$ was slowly added in parts at temperatures below 15°C in an ice bath attributable to an exothermic reaction. The addition of chemicals was done at a slow pace. After 2 hours, 184 ml of distilled water was incorporated, and the compound was continuously stirred at room temperature for about two hours. The slurry was then refluxed at 98°C for 15 minutes, cooled to room temperature (RT), and agitated for two hours. The solution turned bright yellow after gently infusing 40 ml of H_2O_2 and was swirled for an hour with 400 ml of distilled water. The upper layer of water was subsequently extracted, followed by the addition of 10% HCl. The mixture was then subjected to centrifugation, and this process was repeated multiple times. The GO nanoparticles were washed with DW until the pH approached neutral, culminating in a gel-like material. The nanoparticles were dried at 60°C in a vacuum hot air oven and preserved in the dark.

2.2. GO-Ag Hybrid Nanoparticles Synthesis. Figure 1 presents a graphical representation of the synthesis process and molecular structure of GO-Ag hybrid nanoparticles. The GO-Ag nano-hybrids were prepared using presynthesized GO nano powder and Ag metal precursor derived from silver nitrate ($AgNO_3$), following established procedures [12, 24]. Silver nanoparticles (AgNPs) were obtained by reducing $AgNO_3$ in an aqueous solution with ascorbic acid as the reducing agent and trisodium citrate as the stabilizing agent to control the size and shape of the silver nanoparticles [25]. The typical process involved sonicating 1 g of GO in 100 ml of the aqueous solution for 2 hours. Subsequently,

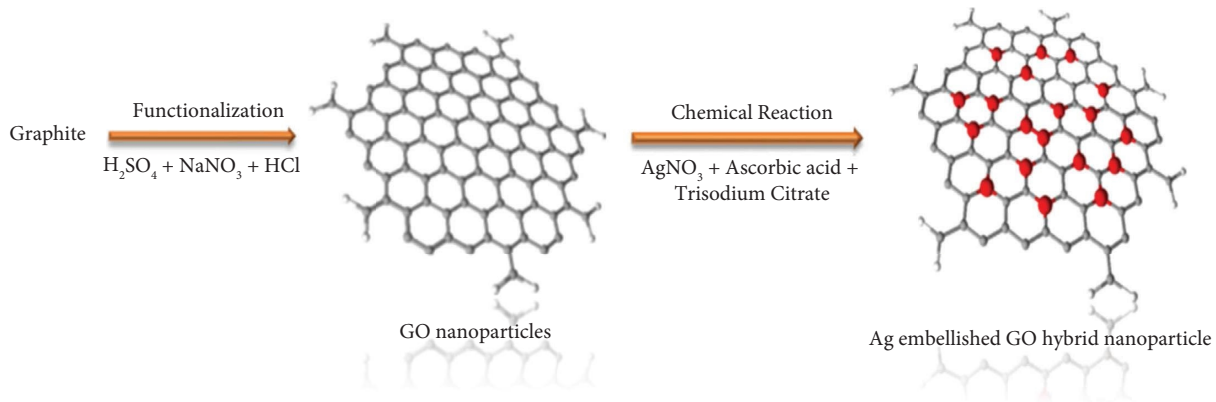

Figure 1: Graphical depiction of the process and molecular structure of GO-Ag hybrid nanoparticles.

6×10^{-2} M $AgNO_3$ dissolved in 100 ml of the aqueous solution, along with an aqueous trisodium citrate solution (1 ml, 10^{-3} M) and freshly prepared ascorbic acid (1 ml, 10^{-3} M), was gradually added to the $AgNO_3$ solution while continuously mixing for 1 hour at room temperature (RT). The resulting solution containing silver nanoparticles was added dropwise to the GO nano-solution while stirring at a constant speed of 90 rpm using a magnetic stirrer. The mixture was then left undisturbed for 48 hours at room temperature in the absence of light and without heating, resulting in the formation of GO-Ag-doped solutions. The GO-Ag solutions underwent centrifugation and were rinsed with DW and ethanol five times. Finally, they were cured at 50°C in a vacuum hot air oven to produce Ag-decorated hybrid nanoparticles.

2.3. GO-Ag Nanofluid Synthesis. A two-step approach was utilized to prepare the GO-Ag hybrid nanofluids from doubled distilled water and the synthesized hybrid nanoparticles of GO-Ag. After fixing the mass of the base fluid (m_{bf}) and the weight percentage of nanoparticles (φ), the mass of the synthesized hybrid nanoparticles was estimated using the following equation:

$$m_{np} = \frac{\varphi . m_{bf}}{1 - \varphi}. \quad (1)$$

The mass (m_{np}) of the synthesized GO-Ag nanohybrids was measured utilizing a high-precision digital balance (0.001 g). To obtain the various weight percentages (0.025%, 0.05%, and 0.1%) of the hybrid nanofluids, the respective known masses of the hybrid nanoparticles and the base fluid were mixed in an ultrasonic device for 30 minutes. Subsequently, constant stirring was carried out in a magnetic stirrer for one hour to achieve better dispersion of the hybrid nanofluids.

2.4. Morphological Characterization of GO-Ag Nanomaterials. Powder X-ray diffraction (XRD-D8 Advance ECO Bruker), scanning electron microscope (SEM, EVO 18, CARL ZEISS, Jena, Germany) at 30 kV, Fourier Transform Infra-Red Spectrophotometer (IR Tracer-100 Shimadzu), particle size analyzer (Horiba SZ-100Z), energy dispersive X-ray spectrometer (EDAX, Quantax 200 with X-Flash), and UV visible spectrometer (SL210, Elico, India) had been used to characterize the topologies of the synthesized GO-Ag nanohybrids.

2.5. Measurement of Thermophysical Properties. A viscometer (LVDVE, Brookfield Engineering Labs, USA) was used to test the viscosities of the nanofluids, which has a precision of ±1%. A KD2 Pro thermal property analyzer (Decagon Devices Inc., USA) employs a KS-1 sensor in a measurement range of 0.02–2 W/m. K and a precision of ±5%.

3. Findings and Critical Analysis

3.1. Findings of XRD. The X-ray diffraction pattern of the Ag deposition on the GO nanosheet is depicted in Figure 2, using the copper anode ($k_{\alpha 1} = 1.54060$). The diffractograms display steep peaks and broad patterns, indicating the presence of crystalline elements. The percentages of crystalline and amorphous phases confirm the deposition of Ag over GO at 36.95% and 63.05%, respectively. The diffracted peaks at Braggs angle $2\theta = 11.1°$ and 16.94° confirm the presence of GO, while the peaks of Ag were observed at scattering angles of 38.1°, 44.3°, 64.5°, and 77.3° with h k l plane indices of (111), (200), (220), and (311). These peaks matched the space group Fm-3m with JCPDS Card no. 07-0783 [24], indicating the successful synthesis of the Ag-decorated GO hybrid nanoparticle.

3.2. Findings of FTIR. The investigation of the associations among all synthesized elements was conducted using the FTIR spectrum analysis. The transmittance proportion and wavenumbers of GO and GO-Ag hybrid nanoparticles were compared. Figure 3 shows that the broad spectral band at 3380.2 cm^{-1} and 1060.78 cm^{-1} corresponds to the O-H bending vibration of carboxylic acid and phenolic acid structural units, which indicates the presence of GO nanosheet [12]. The wavenumber 2360.71 cm^{-1} indicates the C-O bond, representing the bonding of crystalline elements.

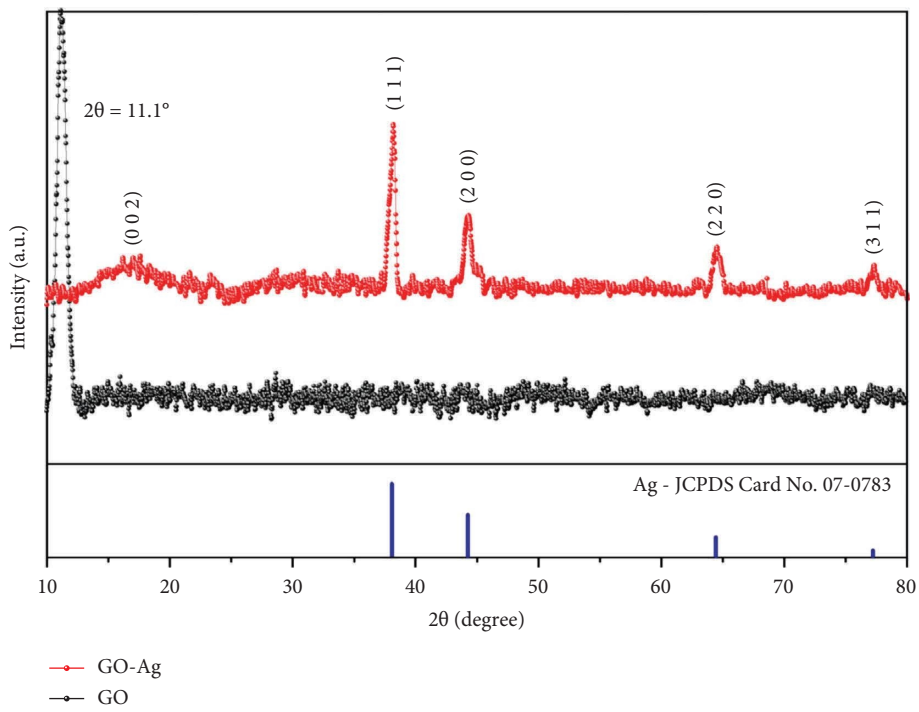

Figure 2: X-Ray diffractogram pattern of GO and GO-Ag hybrid nanoparticles.

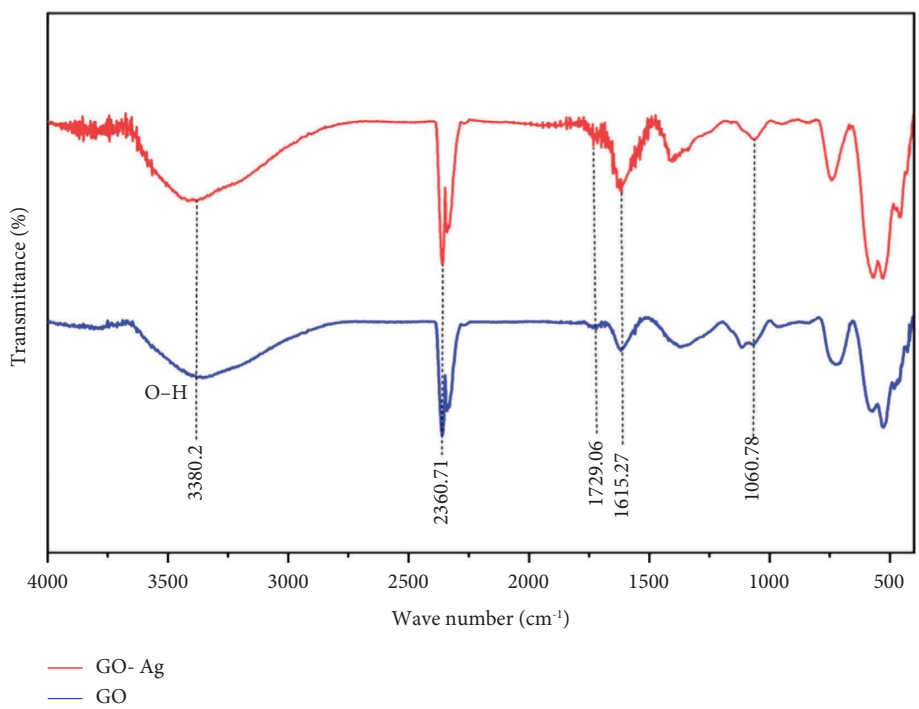

Figure 3: Results on FTIR spectra of GO and GO-Ag hybrid nanoparticles.

The functional bands at 1729.6 cm^{-1} and 1615.27 cm^{-1} are attributed to the asymmetric and symmetric carbonyl stretch vibrations of COOH groups (C=O), respectively. In the GO-Ag spectral bands, the peaks of the GO spectrum were reduced due to the doping of Ag nanoparticles over the GO layer.

The contact between the silver nanoparticles and the GO nanosheets' functional groups encompassing oxygen was stable by reversing the asymmetric and symmetric stretching processes. That is, the depth of the asymmetric –(COO) elongation diminished, while the intensity of the symmetric –(COO) elongation escalated [24].

3.3. Particle Size Analyzer. In order to determine the mean size diameter of the fabricated GO-Ag hybrid nanoparticle observed in Figure 4, the dynamic light scattering (DLS) method was applied. The DLS findings revealed that the synthesized nanocomposite has a mean particle size of 44 nm in precision and a particle size distribution of 30–80 nm.

3.4. Scanning Electron Microscope. Figure 5(a) illustrates the successful synthesis of an amorphous, worm-like structure of graphene oxide nanoparticles, forming silky wrinkled veils [26]. The image also highlights that the single-layer thickness of the GO nanosheet is greater than that of graphene due to the presence of covalently linked oxygen and displaced sp^3 hybridized carbon atoms, situated above and below the original graphene plane [7]. A small section of the image was analysed using ImageJ to determine the surface roughness of the GO nanoparticle, and the results confirmed that the GO nanosheet's surface was smooth, indicating that the formulation procedures and functional units were linked to the chemical process. On the other hand, the evenly distributed quasi-cubical Ag nanoparticles on the GO nano silk veil were found to have a rougher surface than the GO nanosheet (analysed in Image J), which confirms the firm decoration of Ag nanoparticles on the GO, as observed in Figure 5(b) (10 μm), Figure 5(c) (1 μm), and Figure 5(d) (300 nm).

3.5. EDS Analysis. The chemical composition analysis of GO-Ag hybrid nanofluids was conducted utilizing Energy Dispersive Spectroscopy (EDS), revealing weight percentages of carbon (C)—30.4%, oxygen (O)—39.8%, and silver (Ag)—29.8%, as summarized in Table 1. The presence of carbon, oxygen, and silver confirms the existence of graphene oxide and silver nanoparticles, respectively, in its combined form.

The elemental mappings depicted in Figure 6 illustrate the high purity and uniform distribution of Ag nanoparticles anchored over the GO nanosheets. The EDS analysis demonstrates the transmission of carbon and oxygen electrons from the K shell and Ag from the M shell due to their high ionization energies.

3.6. UV Vis Analysis. The UV spectral analysis results, depicted in Figure 7, confirm the successful formation of GO-Ag nanohybrids and are compared to the absorption band of GO nanoparticles. The nanofluids showed a pronounced absorption peak at wavelengths of 234 nm (GO) and 256 nm (GO-Ag), indicating the presence of GO nanoparticles [12]. The broad adsorption spectra at 400 nm (GO-Ag) correspond to the formation of Ag nanoparticles, which are not present in the GO spectrum. This is mainly due to the reflection of the Ag nanoparticle impinging on the surface of the GO nanosheet [12]. This Ag impingement results in a change in the formation of sp^2 polyaromatic carbon, causing a shift in the wavelength from 234 to 256 nm, signifying the partial reduction of GO during the synthesis of the GO-Ag nanohybrids. Moreover, it is associated with a significant reduction in the OH group spectral bands and changes in the asymmetrical and symmetrical spectral bands of GO-Ag, as revealed in the FTIR spectrum.

3.7. Thermal Conductivity. This section presents an investigation into the thermal conductivity of DW (0 wt.%) and GO-Ag hybrid nanofluid with different weight percentages (0.025 wt.%, 0.05 wt.%, 0.1 wt.%). Prior to evaluating the thermal conductivity (K) of the hybrid nanofluids, the K value of DW was measured and assessed using standard data (Incorpera, Dewitt, Bergman, and Lavine) [27], as depicted in Figure 8, which shows a good agreement between the measured and standard parameters.

The precise data was acquired by maintaining the GO-Ag nanofluid samples and the device in a constant-temperature bath for approximately fifteen minutes to achieve equilibrium. The mean of the observed values, with a correlation coefficient exceeding 0.99, was used to determine the sample's K value at a specific weight percentage.

The results indicate that the prepared hybrid nanofluids have a notable improvement in thermal conductivity with a temperature rise from 293 K to 333 K, as shown in Figure 9. This increase is primarily due to the Brownian motion of the dispersed GO-Ag nanoparticles in the base fluid, as the collision of the hybrid nanoparticles leads to the transfer of kinetic energy into thermal energy, resulting in the transfer of energy from the nanoparticles to the water molecules and an increase in the K value of the hybrid nanofluids.

Among the different concentrations and base fluids, the 0.1 wt.% hybrid nanofluid showed the most optimal results at both lower and higher temperatures. For example, at the temperature range of 293 K to 333 K, the thermal conductivity enhancement was about 6.69% to 15.29%, 11.04% to 22.63%, and 15.22% to 31.19% for 0.025 wt.%, 0.05 wt.%, and 0.1 wt.%, respectively, than the base fluid. This demonstrates that the K values increase linearly with temperature.

The thermal conductivity ratio (K_{nf}/K_{bf}) of GO-Ag was observed to be greater than one, signifying its superior performance and efficiency as a heat transfer fluid (Figure 10). Specifically, it was determined that the K_{nf}/K_{bf} increased within the ranges of 1.06–1.15, 1.11–1.22, and 1.15–1.31 for concentrations of 0.025 wt.%, 0.05 wt.%, and 0.1 wt.% over a temperature range of 293 K to 333 K, respectively, in comparison to the base fluid.

3.8. Viscosity. Viscosity (μ) plays a crucial role in influencing the heat flow in nanofluids. The increase in nanoparticle concentration in base fluids causes an increase in viscosity, which ultimately affects the heat transport capabilities. In this study, the viscosity of hybrid nanoparticles with three different weight percentages (0.025%, 0.05%, and 0.1%) was investigated using a Brookfield digital viscometer (LVDV-E, Brookfield, USA).

The viscosity of each sample was determined using spindle S61, which is specifically designed for low-viscosity fluids, while maintaining a consistent shear rate and spindle speed of 30 rpm. The viscosity of each sample was measured in five replicates.

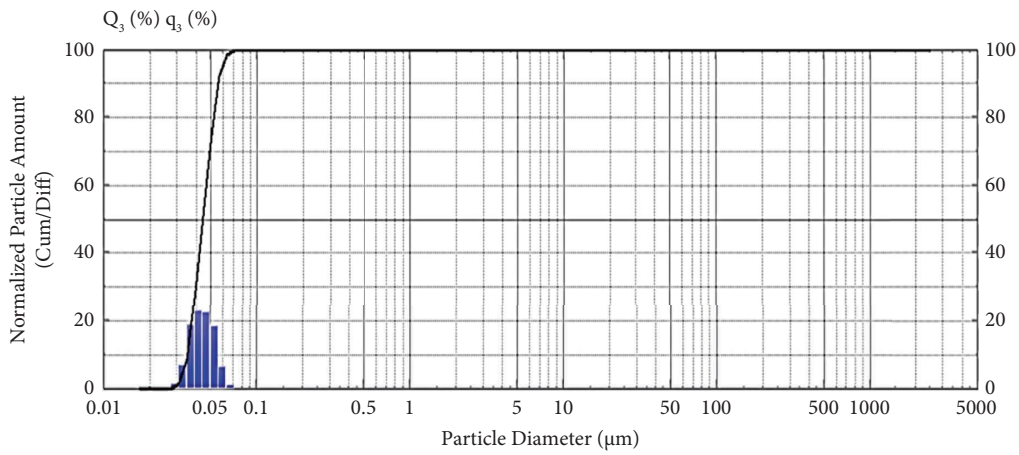

Figure 4: DLS result of GO-Ag hybrid nanoparticles.

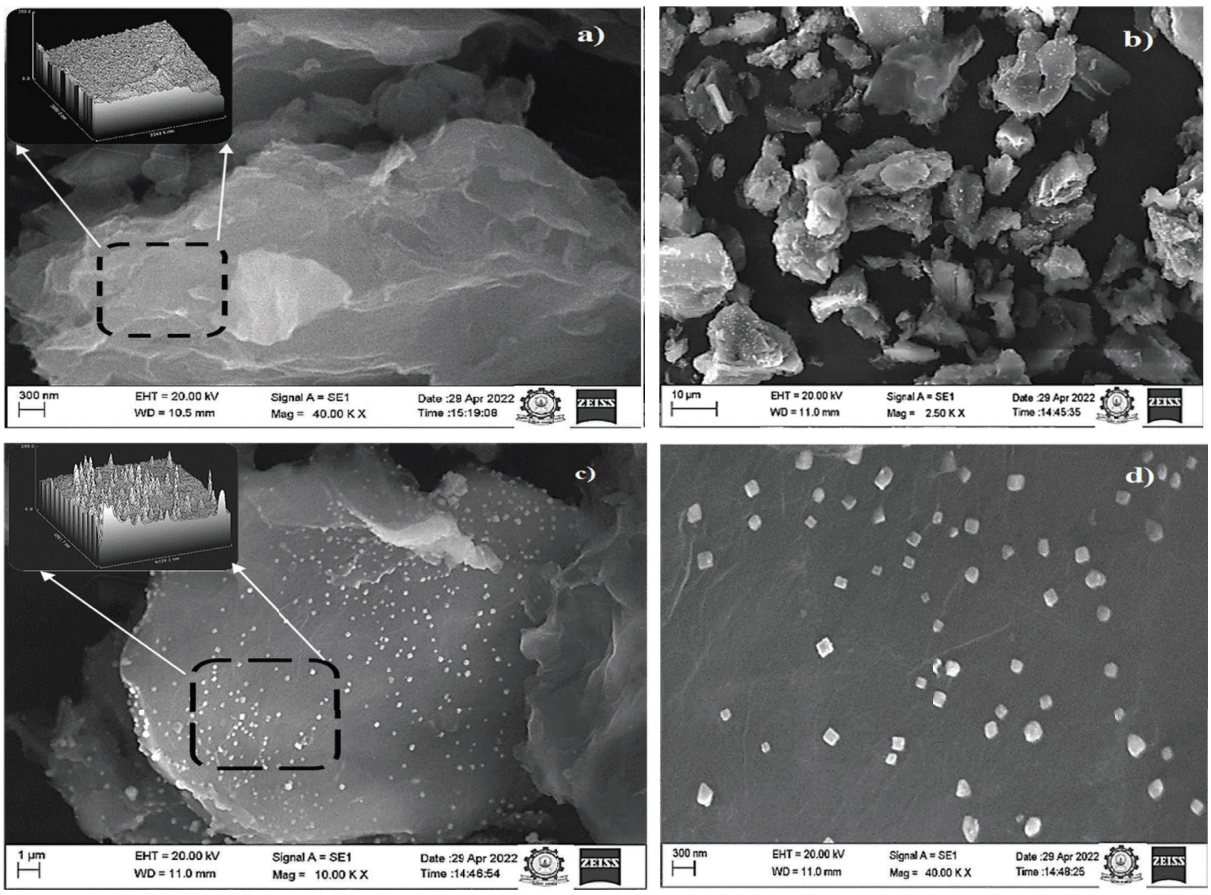

Figure 5: SEM image of (a) GO (300 nm), (b) GO-Ag (10 μm), (c) GO-Ag (1 μm), and (d) GO-Ag (300 nm).

Table 1: EDS analysis.

Elements	Wt. (%)	Atomic (%)	Error (%)	K ratio
C K	30.4	47.8	5.6	0.2067
O K	39.8	46.9	10.5	0.0584
Ag L	29.8	5.2	3.8	0.2475

The results shown in Figure 11 indicate that the viscosity of hybrid nanofluid decreases with increasing temperature. The viscosity of GO-Ag hybrid nanofluids does not vary significantly from that of the base fluid, and the difference in viscosity between GO-Ag nanofluids and the base fluid decreases as the temperature increases. At 293 K, the viscosity of 0.1 wt.% was higher than that of other nanofluid concentrations. However, as the temperature increased, the viscosity of 0.1 wt.% approached that of the base fluid viscosity. The findings suggest that the μ values increase exponentially with an increasing proportion of GO-Ag nanoparticles. However, as the temperature rises with higher concentrations of nanoparticles, viscosity decreases at

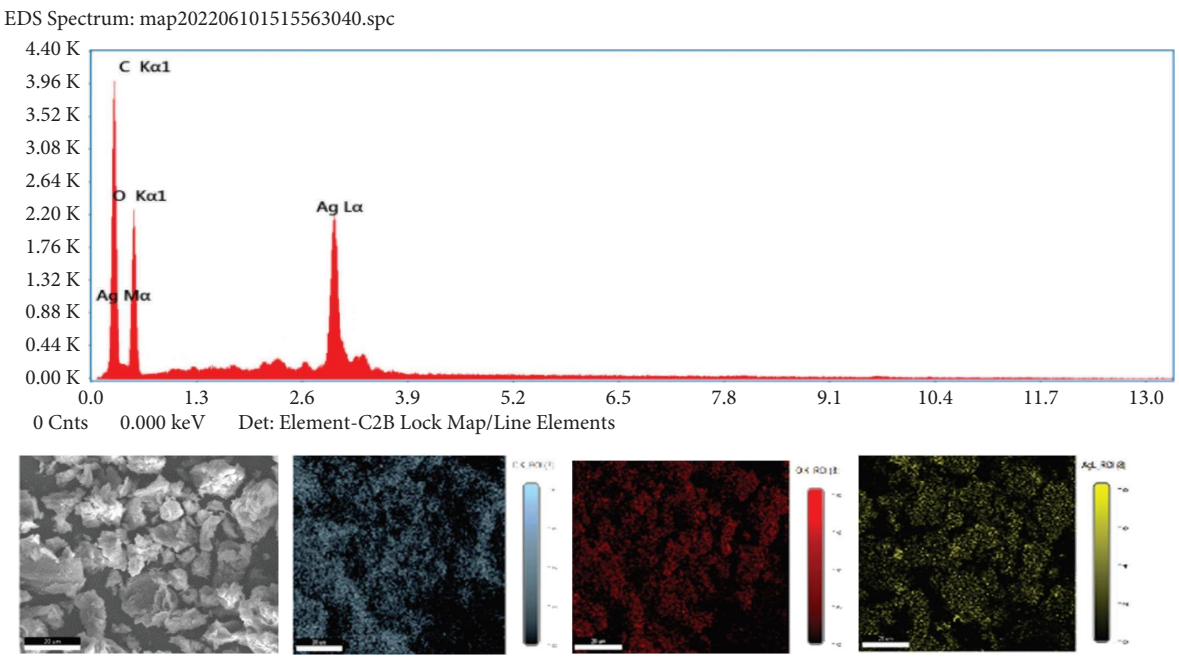

Figure 6: EDS analysis of GO-Ag nanoparticles and elemental mapping of SEM image, C, O, and Ag.

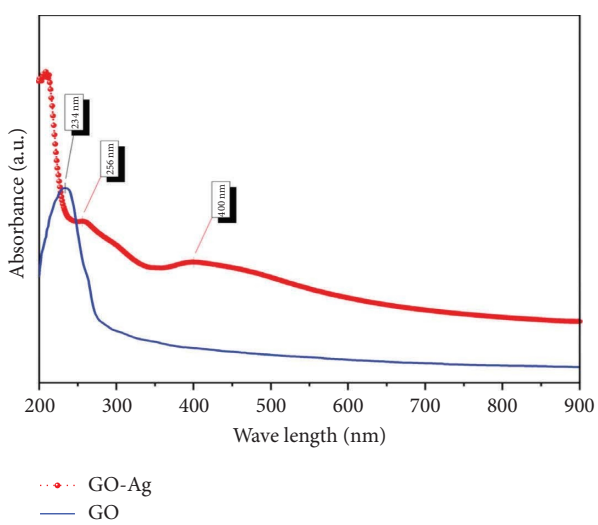

Figure 7: UV-absorbance spectrum of GO and GO-Ag hybrid nanoparticles.

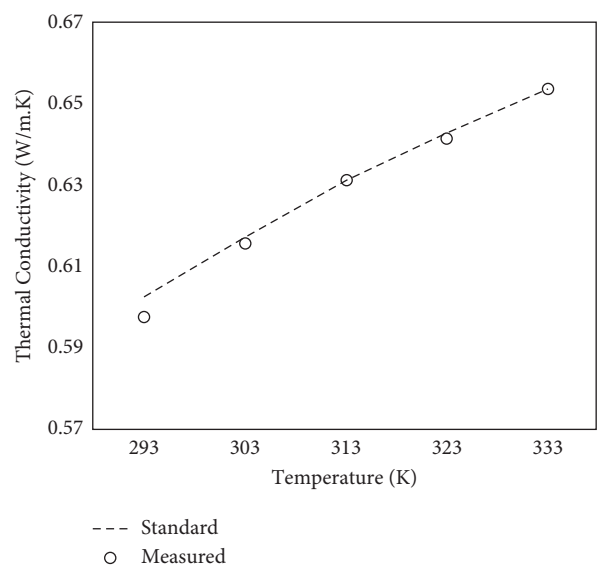

Figure 8: Measured and standard values of DW.

a faster pace. This happens because an increase in temperature reduces the density of the fluid, limiting the shearing force between fluid interfaces.

4. Validation of Results

4.1. Comparison between Experimental Results of (K_{nf}/K_{bf}) and Standard Correlated Models. In order to relate the experimental results (K_{nf}/K_{bf}) to the appropriate correlated standard models, some well-known prominent thermal conductivity models from the past and present were used in this study. Like the Maxwell model [28] in (2), it is the most popular, conventional, and used by many researchers to correlate their experimental findings, where K_{nf} is the thermal conductivity of the nanofluid, K_{bf} is the thermal conductivity of the base fluid, and K_p is the nanoparticle thermal conductivity coefficient.

$$\frac{K_{nf}}{K_{bf}} = \frac{\left(2K_{bf} + K_p + 2\varphi\left(K_p - K_{bf}\right)\right)}{2K_{bf} + K_p - \varphi\left(K_p - K_{bf}\right.}. \quad (2)$$

Furthermore, Timofeeva et al. [29], in equation (3), analysed several nanoparticles and offered a concentration-based thermal conductivity ratio relationship.

$$\frac{K_{nf}}{K_{bf}} = (1 + 3\varphi). \quad (3)$$

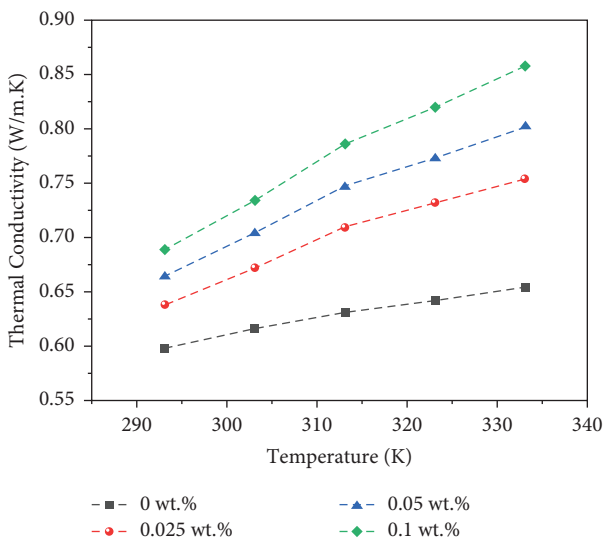

Figure 9: Results on K value of GO-Ag nanofluids.

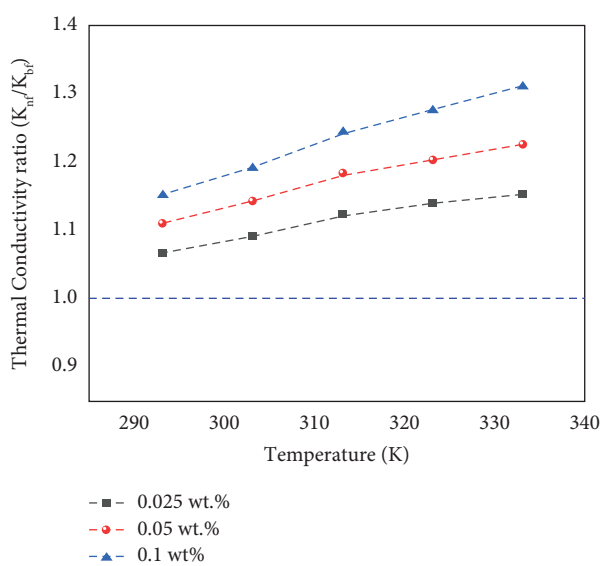

Figure 10: Thermal conductivity ratio (K_{nf}/K_{bf}) of GO-Ag nanofluids.

Later, Lu and Lin [30], in equation (4), similar to Timofeeva et al., postulated a relationship based on nanoparticle concentration.

$$\frac{K_{nf}}{K_{bf}} = \left(1 + 2.25\varphi + 2.27\varphi^2\right). \quad (4)$$

While experimenting with the thermophysical characteristics of graphene oxide and alumina nanoparticles, Taherialekouhi et al. [18], in equation (5), suggested a model between both the concentration and temperature of nanoparticles as dependent elements.

$$\frac{K_{nf}}{K_{bf}} = \left(0.031 * \left(T^{1.185}\right) * \left(\varphi^{0.863}\right) + 1.006\right). \quad (5)$$

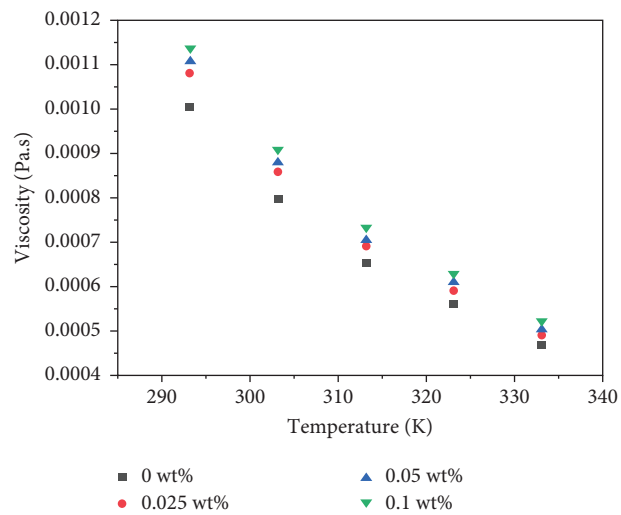

Figure 11: The viscosity of GO-Ag nanofluid.

The empirical thermal conductivity ratio of the GO-Ag nanofluid was compared to various standard models, and the results were presented in Figures 12(a)–12(e). It was observed that the empirical K_{nf}/K_{bf} of the nanofluid performed significantly better than the standard models. For instance, at 333 K, the experimental K_{nf}/K_{bf} of GO-Ag showed a remarkable increase of 12.67% compared to the Taherialekouhi et al. model. Hence, the empirical K-ratio results were found to deviate from the standard relations mentioned earlier. However, to investigate the thermal conductivity of GO-Ag nanofluid, a suitable mathematical model was proposed using the response surface methodology (RSM) approach. We meticulously analysed the experimental thermal conductivity ratio and precisely predicted a mathematical model that fits the experimental data.

4.2. RSM Regression Model. The Response Surface Methodology (RSM) approach was employed to establish a linear correlation in this study. Response surface regression analysis is a well-known technique in design of experiments (DOE) applications [20, 31]. The input data was examined with respect to the experimentally measured results to determine the final output. The primary objective was to create a statistical and mathematical model based on empirical K ratio values of GO-Ag nanofluid. The accuracy and reliability of the created regression model were evaluated using the analysis of variance (ANOVA) approach, as presented in Table 2. A correlation between the predicted and experimental results can only be achieved when the R^2 value is close to one. In this study, the regression analysis of the experimental results produced an R^2 value of 0.99, indicating a better correlation between predicted and empirical values. The quadratic regression analysis was preferred over other analyses such as 2FI, linear, and cubic, as it resulted in a very low p value of 0.0001 and a higher Fisher test value (F-value). The p value should be less than 0.05 to achieve better optimization [20]. The predicted equation for the K

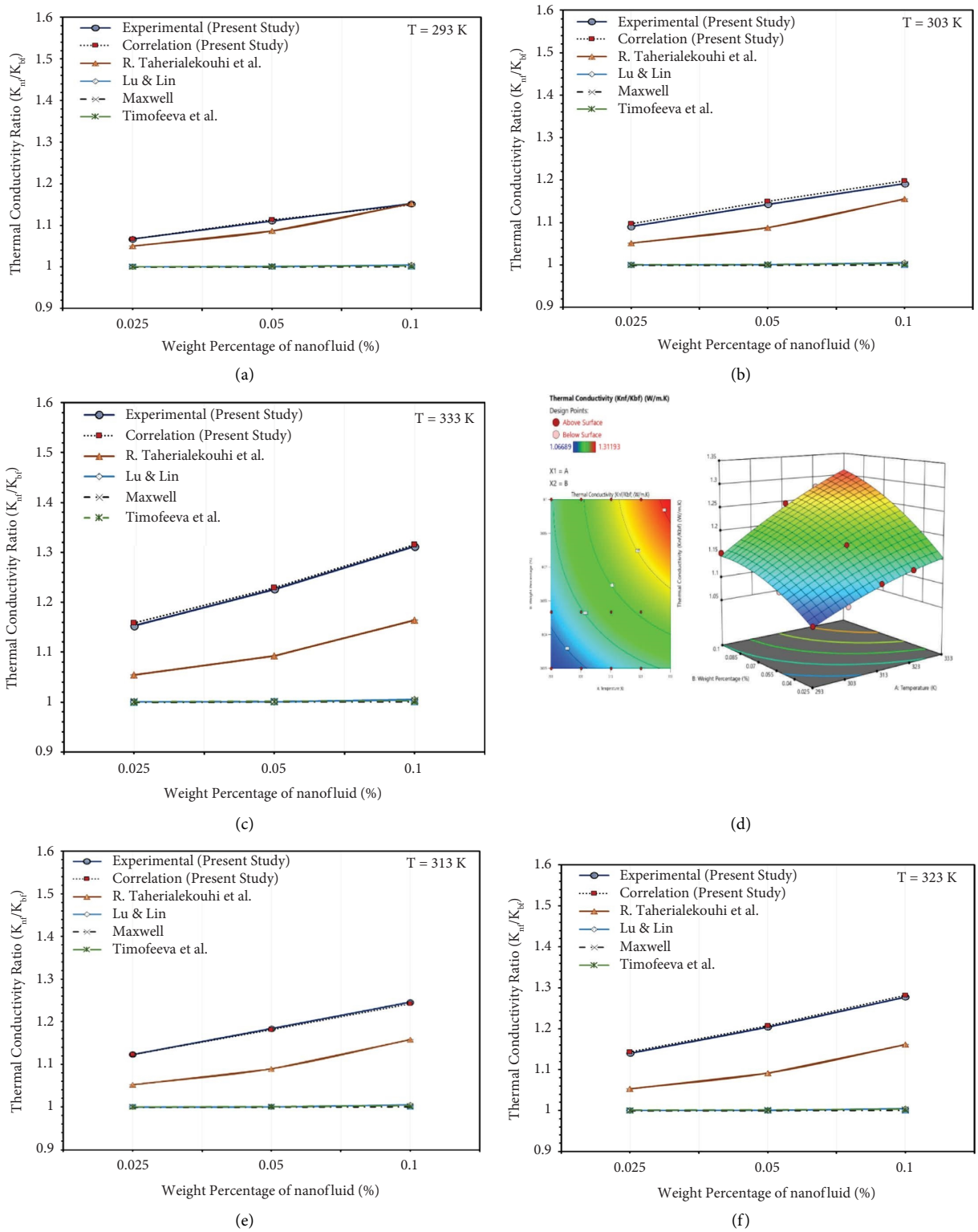

Figure 12: (a–e) Comparison of weight percentage of nanofluids vs thermal conductivity ratio at different temperatures ranging from 293 K–333 K, and (f) contour and three-dimensional diagram of the proposed correlation.

ratio of the GO-Ag nanofluid is provided by equation (6), with temperature (T in K) and weight percentage (φ) as constraint factors at low and higher concentrations ($0.025\,\text{wt.\%} < \varphi < 0.1\,\text{wt.\%}$) of GO-Ag hybrid nanofluids. The nanoparticle concentration factor (φ) in the proposed model was found to be the most significant and preferable factor compared to temperature based on the variance analysis results.

Table 2: ANOVA-type III-partial sum of squares.

Source	Sum of squares	*Df*	Mean square	*F*-value	*p*-value	
Model-K_{nf}/K_{bf}	0.0664	5	0.0133	452.85	<0.0001	Significant
A-Temperature	0.0301	1	0.0301	1027.30	<0.0001	
B-Weight percentage	0.0356	1	0.0356	1212.21	<0.0001	
AB	0.0018	1	0.0018	62.89	<0.0001	
A^2	0.0003	1	0.0003	8.96	0.0151	
B^2	0.0011	1	0.0011	38.58	0.0002	
Residual	0.0003	9	0			
Cor total	0.0667	14				

$$\frac{K_{nf}}{K_{bf}} = 0.017294T - 4.40638\varphi + 0.025153T\varphi - 0.000025T^2 - 15.01048\varphi^2 - 1.91857. \quad (6)$$

The regression model proposed using RSM analysis accurately fits the experimental data, with most of the predicted points being close to the experimental values shown in Figures 12(a)–12(e).

The contour and three-dimensional diagrams of the proposed model are presented in Figure 12(f). It was observed that the K_{nf}/K_{bf} improved with an increase in both T and φ of nanoparticles. Figure 13 compares the empirical and predicted results of K_{nf}/K_{bf}, showing the maximum percentage deviation between empirical and predicted to be ±1.2%. This deviation indicates an acceptable mathematical correlation with the experimental results. Table 3 shows the comparison between the results of the actual and predicted thermal conductivity ratios of GO-Ag hybrid nanofluids with residual errors, leverage, and externally studentized residuals.

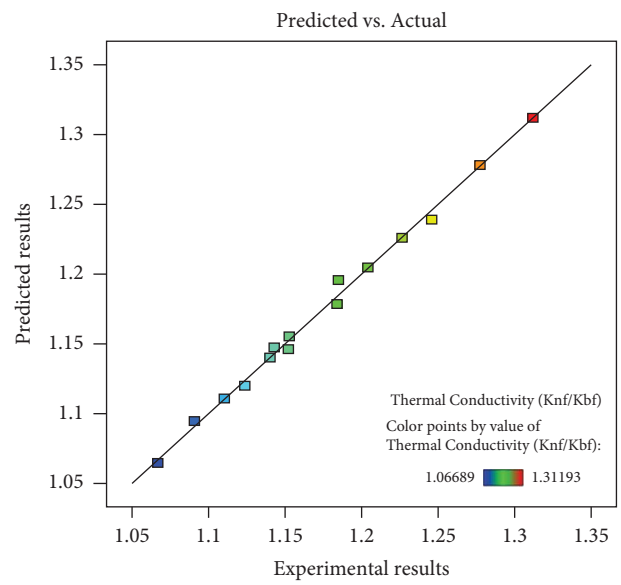

Figure 13: Predicted results vs experimental results.

5. Processes Governing Thermal Conductivity Augmentation in GO-Ag Nanofluid

The impact of several key processes enhanced the K value of GO-Ag hybrid nanofluids. Following are a few contributing factors that impact the improvement of thermal conductivity.

(1) Brownian motion [15, 32]: As the temperature of the hybrid nanofluids increased, the dispersed GO-Ag hybrid nanoparticles began to move randomly due to the excess heat. This resulted in relative lateral motion and collisions between the particles, converting kinetic energy to thermal energy and dissipating it to the base fluid's molecules. This prolonged contact between particles and molecules promoted microconvectional heat transport, enhancing nanoscale conduction and convection heat transfer.

(2) Clustering of nanoparticles [33, 34]: The surface area of GO and Ag nanoparticles is increased due to clustering, as observed in SEM images of Ag nanoparticles clustered on the surface of GO nanosheets. These clusters improve interaction with the fluid layers, enhancing microconvective heat transfer and thermal conductivity. The liquid layers adjacent to the enhanced surface behave like solid surfaces at the solid-liquid interface, improving heat transfer from the nanoparticle to its next liquid layer.

(3) Electron-phonon collision: A relatively high thermal conductivity performance factor was observed at higher temperatures, possibly due to the aforementioned factors. Electron-hole pair excitation and electron-electron collisions may occur in dispersed hybrid nanoparticles due to thermal effects. The presence of external energy results in electron lattice collisions, coupling low-level energy electrons to phonons, and increasing the temperature of metal lattices. Heat produced in the metal lattice dissipates into the surrounding fluid molecules through phonon-phonon scattering [35]. This phenomenon causes the heat to dissipate from the energized nanoparticles into the base fluid, contributing to the increase in thermal conductivity.

(4) Other factors, including surface chemical effects, atomic force, crystalline nature, and nanoscale rotation of nanoparticles due to temperature increase, also contribute to the development of the K value of the hybrid system.

Table 3: Comparison of actual and predicted thermal conductivity ratios.

Wt. (%)	Temperature (K)	Actual K-ratio	Predicted K-ratio	Percentage of deviation (%)	Residual	Leverage	Externally studentized residuals
0.025	293	1.0669	1.0674	0.0519	0.002	0.581	0.54
	303	1.0909	1.0977	0.6194	−0.004	0.295	−0.867
	313	1.1236	1.1228	−0.0718	0.0037	0.295	0.792
	323	1.1402	1.1430	0.2451	0.0003	0.295	0.061
	333	1.1529	1.1581	0.4494	−0.0019	0.581	−0.531
0.05	293	1.1104	1.1135	0.2819	−0.0006	0.438	−0.127
	303	1.1429	1.1498	0.6116	−0.0044	0.26	−0.924
	313	1.1838	1.1814	−0.2059	0.0053	0.295	1.198
	323	1.2041	1.2078	0.3140	−0.0007	0.26	−0.145
	333	1.2263	1.2293	0.2467	0.0003	0.438	0.066
0.1	293	1.1522	1.1666	1.2497	0.0055	0.667	2.021
	303	1.1851	1.1982	1.1121	−0.0105	0.317	−3.522
	313	1.2456	1.2424	−0.2637	0.0062	0.295	1.439
	323	1.2773	1.2814	0.3253	−0.001	0.317	−0.212
	333	1.3119	1.3153	0.2574	−0.0002	0.667	−0.049

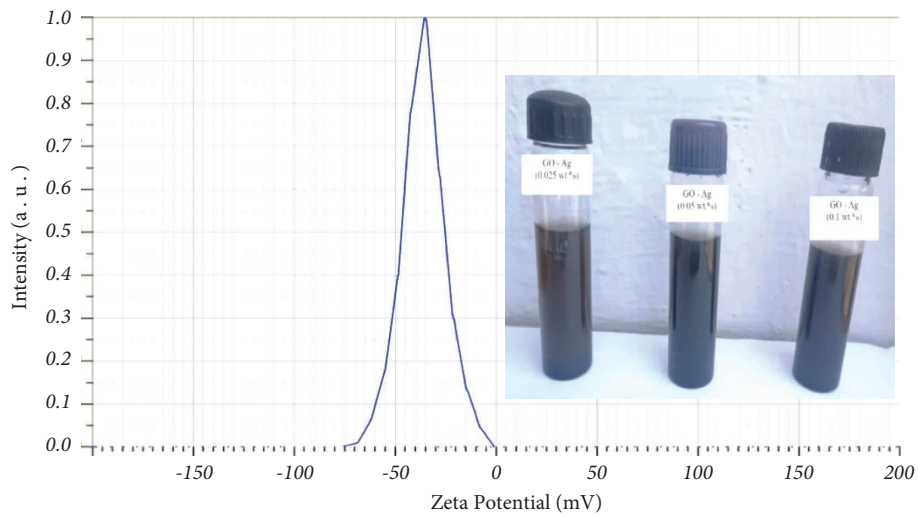

Figure 14: Zeta potential analysis and pictorial view of prepared samples.

6. Stability

The dissemination of hybrid nanoparticles in the base fluid was confirmed by conducting zeta potential [34] and UV-visible spectra [15] analyses using nanofluids at all concentrations of GO-Ag (0.025 wt.%, 0.05 wt.%, and 0.1 wt.%). The electrokinetic potential (zeta potential) value was measured to indicate the repulsive force and stability of the nanoparticles in the base fluid. The greater the values of the zeta potential (either positive or negative), the greater the stability of the nanofluids.

Nanofluids with a value greater than ±30 mV were considered to possess higher repulsive forces between particle suspensions, resulting in less agglomeration and good stability [34]. The zeta potential result of the GO-Ag hybrid nanofluid sample, as shown in Figure 14, had a mean value of −35.6 mV, indicating that the nanofluid was highly stable with a considerable negative repellent potential.

Furthermore, the UV absorbance of the silver nanoparticles at $\lambda = 400$ nm in GO-Ag hybrid nanofluids was analysed in Figure 15. The observed results showed hardly any changes in wavelength or absorbance value after 25 days of measurements in the UV-visible spectrometer, demonstrating the high stability of the hybrid nanofluids. This stability might be due to the functional group on the interface of the GO nanoparticles, which anchored the strong bond with the Ag nanoparticles, and the influence of reducing and stabilizing agents on the Ag nanosurface decreased the agglomeration of nanoparticles to settle down and in reaction with water molecules. Therefore, it is presumed that the prepared hybrid nanofluids are stable in all applications.

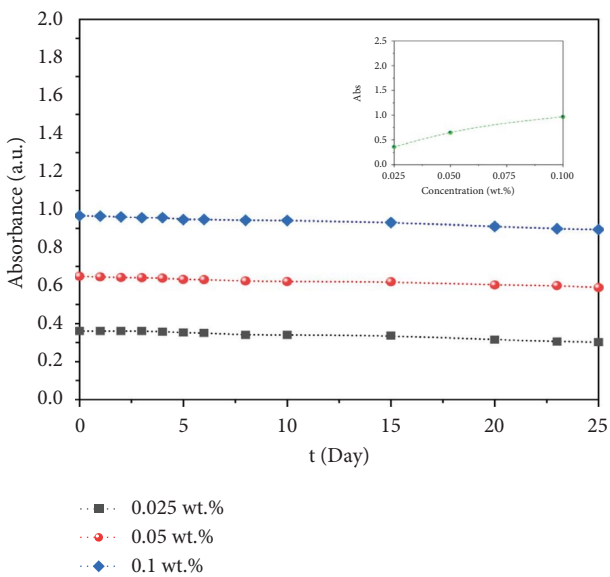

Figure 15: UV absorbance spectrum of GO-Ag nanofluids at $\lambda = 400$ nm.

7. Conclusion

The low-cost chemical reduction technique was utilized to synthesize the GO-Ag hybrid nanoparticles. A detailed experimental investigation was conducted on the preparation, characterization, and thermophysical properties of the GO-Ag hybrid nanofluids at different weight percentages. The following findings were established:

(1) The particle size analyzer, XRD, FTIR, UV, SEM, and EDX analyses demonstrated that the hybrid structure comprised significant molecular linkages of all elements (GO and Ag).

(2) The K and μ values of the hybrid nanofluids were found to be in agreement and increased with increasing concentrations of the nanoparticles.

(3) At 333 K temperature in 0.1 wt.%, the GO-Ag nanofluid exhibited the highest thermal conductivity enhancement of 31.19% compared to the base fluid.

(4) The K ratio of GO-Ag hybrid nanofluids was evaluated by comparing it to standard models. A mathematical relationship was derived using RSM methodology based on the empirical values of the thermal conductivity of GO-Ag hybrid nanofluids as a function of temperature and weight percentage. Compared to other standard equations discussed, the derived equation showed a better correlation with the empirical results.

(5) Zeta potential and UV visible spectrum analyses confirmed the stability of the nanofluids. Due to their improved thermophysical properties, GO-Ag nanofluids could be an excellent choice for heat transport fluids in applications such as solar-thermal and heat exchanging equipment.

Data Availability

The data used to support the findings of this study are available from the corresponding author upon request.

Conflicts of Interest

The authors declare that there are no conflicts of interest.

Authors' Contributions

M. Armstrong conceptualised the study, was responsible for nanoparticles selection, synthesis, characterization, and experimentation, and was responsible for Software, data curation, and manuscript preparation. M. Sivasubramanian performed supervision, experimental testing, and manuscript verification. N. Selvapalam and R. Pavitra were responsible for cosupervision and guidance in nanoparticle preparation. P. Rajesh KAnna and Haiter Lenin cosupervised the study and verified the manuscript.

Acknowledgments

The authors expressed their gratitude to the Department of Mechanical Engineering and the International Research Centre at the Kalasalingam Academy of Research and Education for allowing them to use all the laboratories.

References

[1] M. Asim and F. R. Siddiqui, "Hybrid nanofluids—next-generation fluids for spray-cooling-based thermal management of high-heat-flux devices," *Nanomaterials*, vol. 12, no. 3, p. 507, 2022.

[2] A. T. Smith, A. M. LaChance, S. Zeng, B. Liu, and L. Sun, "Synthesis, properties, and applications of graphene oxide/reduced graphene oxide and their nanocomposites," *Nano Materials Science*, vol. 1, pp. 31–47, 2019.

[3] C. Rajaganapathy, D. Vasudevan, and N. Selvakumar, "Investigation on Tribological and mechanical behaviour of AA6082- graphene based composites with Ti particles," *Materials Research Express*, vol. 7, Article ID 076514, 2020.

[4] K. K. Jha, M. Armstrong, S. S. Kumar, M. V. Kumar, and G. S. S. Charan, "A recent examination on the performance of heat pipes in nanofluids in enhancing the thermodynamic properties," *Materials Today: Proceedings*, vol. 60, pp. 1920–1926, 2022.

[5] A. S. Manirathnam, M. Dhanush Manikandan, R. Hari Prakash, B. Kamesh Kumar, and M. Deepan Amarnath, "Experimental analysis on solar water heater integrated with Nano composite phase change material (SCi and CuO)," *Materials Today: Proceedings*, vol. 37, pp. 232–240, 2021.

[6] P. Majumder and R. Gangopadhyay, "Evolution of graphene oxide (go)-based nanohybrid materials with diverse compositions: an overview," *RSC Advances*, vol. 12, pp. 5686–5719, 2022.

[7] Z. Hajjar, A. M. Rashidi, and A. Ghozatloo, "Enhanced thermal conductivities of graphene oxide nanofluids," *International Communications in Heat and Mass Transfer*, vol. 57, pp. 128–131, 2014.

[8] X. Mei, X. Sha, D. Jing, and L. Ma, "Thermal conductivity and rheology of graphene oxide nanofluids and a modified

predication model," *Applied Sciences*, vol. 12, no. 7, p. 3567, 2022.

[9] W. Raza and S. B. Krupanidhi, "Retraction of: Engineering defects in graphene oxide for selective ammonia and enzyme-free glucose sensing and excellent catalytic performance for para-nitrophenol reduction," *ACS Applied Materials and Interfaces*, vol. 11, no. 2, p. 2560, 2019.

[10] M. C. Mbambo, M. J. Madito, T. Khamliche, C. B. Mtshali, Z. M. Khumalo, and I. G. Madiba, "Thermal conductivity enhancement in gold decorated graphene nanosheets in ethylene glycol based nanofluid," *Scientific Reports*, vol. 10, no. 1, Article ID 14730, 2020.

[11] M. Armstrong, M. Sivasubramanian, and N. Selvapalam, "A review on the enhancement of heat exchanging process using TiO_2 Nanofluids," *Lecture Notes in Mechanical Engineering*, Springer, Singapore, 2020.

[12] M. Cobos, I. De-La-pinta, G. Quindós, M. D. Fernández, and M. J. Fernández, "Graphene oxide–silver nanoparticle nanohybrids: synthesis, characterization, and antimicrobial properties," *Nanomaterials*, vol. 10, 2020.

[13] K. Elsaid, M. A. Abdelkareem, H. M. Maghrabie et al., "Thermophysical properties of graphene-based nanofluids," *International Journal of Thermofluids*, vol. 10, Article ID 100073, 2021.

[14] M. Armstrong, M. Sivasubramanian, N. Selva Palam, M. Adam Khan, and C. Rajaganapathy, "A recent examination on the nano coating techniques in heat transfer applications," *Materials Today: Proceedings*, vol. 46, pp. 7942–7947, 2021.

[15] D. Li, Y. Wang, M. Guo, M. Song, and Y. Ren, "Preparation and thermophysical properties of graphene oxide-silver hybrid nanofluids," *Bulletin of Materials Science*, vol. 43, no. 1, p. 147, 2020.

[16] G. Huminic, A. Vărdaru, A. Huminic, C. Fleacă, F. Dumitrache, and I. Morjan, "Water-based graphene oxide–silicon hybrid nanofluids—experimental and theoretical approach," *International Journal of Molecular Sciences*, vol. 23, no. 6, p. 3056, 2022.

[17] J. Singh, R. Kumar, M. Gupta, and H. Kumar, "Thermal conductivity analysis of GO-CuO/DW hybrid nanofluid," *Materials Today: Proceedings*, vol. 28, pp. 1714–1718, 2020.

[18] R. Taherialekouhi, S. Rasouli, and A. Khosravi, "An experimental study on stability and thermal conductivity of water-graphene oxide/aluminum oxide nanoparticles as a cooling hybrid nanofluid," *International Journal of Heat and Mass Transfer*, vol. 145, Article ID 118751, 2019.

[19] N. M. El-Shafai, R. Ji, M. Abdelfatah et al., "Investigation of a novel (GO@CuO.γ-Al2O3) hybrid nanocomposite for solar energy applications," *Journal of Alloys and Compounds*, vol. 856, 2021.

[20] R. Vidhya, T. Balakrishnan, and B. S. Kumar, "Experimental and theoretical investigation of heat transfer characteristics of cylindrical heat pipe using Al2O3–SiO2/W-EG hybrid nanofluids by RSM modeling approach," *Journal of Engineering and Applied Science*, vol. 68, no. 1, p. 32, 2021.

[21] M. Armstrong, M. Sivasubramanian, N. Selvapalam, and C. Rajaganapathy, "Revving up heat transfer performance of double pipe heat exchanger using diverse molar Ag-GO hybrid nanofluids: an Empirical and Numerical study using Central Composite Design," *Journal of Enhanced Heat Transfer*, vol. 30, 2023.

[22] M. Behrouz, S. Dinarvand, M. E. Yazdi, H. Tamim, I. Pop, and A. J. Chamkha, "Mass-based hybridity model for thermo-micropolar binary nanofluid flow: first derivation of angular momentum equation," *Chinese Journal of Physics*, vol. 83, pp. 165–184, 2023.

[23] W. S. Hummers and R. E. Offeman, "Preparation of graphitic oxide," *Journal of the American Chemical Society*, vol. 80, no. 6, p. 1339, 1958.

[24] K. S. Hui, K. N. Hui, D. A. Dinh et al., "Green synthesis of dimension-controlled silver nanoparticle-graphene oxide with in situ ultrasonication," *Acta Materialia*, vol. 64, pp. 326–332, 2014.

[25] Y. Qin, X. Ji, J. Jing, H. Liu, H. Wu, and W. Yang, "Size control over spherical silver nanoparticles by ascorbic acid reduction," *Colloids and Surfaces A: Physicochemical and Engineering Aspects*, vol. 372, no. 1-3, pp. 172–176, 2010.

[26] M. Mehrali, E. Sadeghinezhad, M. A. Rosen et al., "Experimental investigation of thermophysical properties, entropy generation and convective heat transfer for a nitrogen-doped graphene nanofluid in a laminar flow regime," *Advanced Powder Technology*, vol. 27, no. 2, pp. 717–727, 2016.

[27] P. Frank Incorpera, P. David Dewitt, L. Theodeore Bergman, and S. Adrienne Lavine, *Fundamentals of Heat and Mass Transfer*, John Wiley & Sons, River Street, HB, USA, 6th edition, 2007.

[28] C. M. James, *A Treaties on Electricity and Magnetism*, Clarendon Press, Oxford, England, 1873.

[29] E. V. Timofeeva, A. N. Gavrilov, J. M. McCloskey, Y. V. Tolmachev, S. Sprunt, and L. M. Lopatina, "Thermal conductivity and particle agglomeration in alumina nanofluids: experiment and theory," *Physical Review*, vol. 76, no. 6, Article ID 061203, 2007.

[30] S. Y. Lu and H. C. Lin, "Effective conductivity of composites containing aligned spheroidal inclusions of finite conductivity," *Journal of Applied Physics*, vol. 79, pp. 6761–6769, 1996.

[31] P. A. Karthick, S. R. Kumar, P. Prathap, K. Ragul, and K. S. Raghul, "Optimization of reaming parameters to improve surface roughness of En1A leaded material with the approach of particle swarm optimization," *Materials Today Proceedings*, vol. 37, pp. 1003–1008, 2020.

[32] M. F. Nabil, W. H. Azmi, K. A. Hamid, N. N. M. Zawawi, G. Priyandoko, and R. Mamat, "Thermo-physical properties of hybrid nanofluids and hybrid nanolubricants: a comprehensive review on performance," *International Communications in Heat and Mass Transfer*, vol. 83, pp. 30–39, 2017.

[33] I. Gonçalves, R. Souza, G. Coutinho et al., "Thermal conductivity of nanofluids: a review on prediction models, controversies and challenges," *Applied Sciences*, vol. 11, no. 6, p. 2525, 2021.

[34] M. Armstrong, S. Mahadevan, N. Selvapalam, C. Santulli, S. Palanisamy, and C. Fragassa, "Augmenting the double pipe heat exchanger efficiency using varied molar Ag ornamented graphene oxide (GO) nanoparticles aqueous hybrid nanofluids," *Frontiers in Materials*, vol. 10, Article ID 1240606, 2023.

[35] D. Mateo, J. L. Cerrillo, S. Durini, and J. Gascon, "Fundamentals and applications of photo-thermal catalysis," *Chem Soc Rev.*, vol. 50, pp. 2173–2210, 2021.

Hindawi
Advances in Materials Science and Engineering
Volume 2023, Article ID 9387016, 20 pages
https://doi.org/10.1155/2023/9387016

Review Article

Chitosan Biopolymer and Its Nanocomposites: Emerging Material as Adsorbent in Wastewater Treatment

Indran Suyambulingam,[1] Lekshmi Gangadhar,[2] Siva Sankar Sana,[3] Divya Divakaran,[1] Suchart Siengchin,[1] Lekshmi A. Kurup,[4] Jenish Iyyadurai,[5] and K. E. Albert Bernad Noble[6]

[1]*Natural Composites Research Group Lab, Department of Materials and Production Engineering, The Sirindhorn International Thai-German School of Engineering (TGGS), King Mongkut's University of Technology North Bangkok (KMUTNB), Bangkok 10800, Thailand*
[2]*Department of Nanotechnology, Nanodot Research Private Limited, Nagercoil, Kanyakumari, India*
[3]*School of Chemical Engineering and Technology, North University of China, Taiyuan 030051, China*
[4]*School of Chemistry and Physics, Queensland University of Technology, Brisbane, QLD 4000, Australia*
[5]*Department of Applied Mechanics, Seenu Atoll School, Hulhu-medhoo, Addu City, Postal Code 19060, Maldives*
[6]*Department of Physics, Hamad School, Laamu Atoll, Maldives*

Correspondence should be addressed to K. E. Albert Bernad Noble; albert.bernad@hamadschool.edu.mv

Received 3 November 2022; Revised 24 December 2022; Accepted 31 March 2023; Published 24 July 2023

Academic Editor: V. Cijayan

Water pollution is a global issue because of potentially lethal toxins. Polymeric nanomaterials are making their way into water treatment processes and are being utilized to efficiently remove a variety of pollutants. Polymeric nanomaterials are a popular option for a solution because they have a high adsorption capacity and a high surface charge. Nanocomposites have recently come to the attention of those working in the field of water treatment in order to more effectively remove contaminants. Polymeric composites are based on biopolymers and are being developed. These all quickly reached the industrial standards because of their low impact on the natural world. Chitosan is one of the biopolymers that are used extensively. Moreover, it is one of the most highly preferred biopolymers. It is simple to scale up and is readily available. The incorporation of nanomaterials into the biopolymer enables better control over the shape, size, and morphology of the particle, as well as an increase in the efficiency with which contaminants are removed. This is an excellent review that examines recent developments in the formation of chitosan-based polymeric nanocomposites and their performance in removing various contaminants including heavy metals, dyes, pesticides, pharmaceutical waste, and radionuclides from water.

1. Introduction

The increased globalization and industrialization have led to many different contaminants polluting our water sources. As the demand for pure drinking water increases day by day, the depletion of water resources leaves mankind with no other option other than the use-reuse cycle. But this gets a bit complicated as the water is polluted by many different kinds of pollutants [1, 2]. The main pollutants in water not only damage the health of people but also affect the organisms present in the water bodies [3]. Pollutants affect the plants too in the water; the presence of pollutants, or specifically dyes, hinders the penetration of sunlight, which results in less photosynthetic activity [4]. There have been many research studies carried on discussing the harmful effects of pollutants in water. Water gets polluted due to a variety of contaminants such as detergents, fertilizers, pesticides, dyes, pharmaceuticals, and heavy metals [5]. Apart from these organic pollutants such as hydrocarbons, phenols, oils, and greases are also part of the contaminants. The role of hospitals and industries in polluting the water sources are worth mentioning, leading to microbial contamination. There are

studies to date revealing the presence of microplastics in marine water [6]. And the removal of these harmful pollutants is the need of the hour. This is achieved by many different water treatment methods.

Earlier, many different processes such as ion-exchange, ultrafiltration, reverse osmosis, oxidation, flocculation, and adsorption are used. The use of membranes for the removal of pathological contaminants is also carried out. But the adsorption technique is the widely used process to remove organic, anionic, or cationic pollutants [7]. With increasing pollutants, the already present methods for water treatment have become inefficient, resulting in the need for new treatment methods. Nanotechnology with nanomaterials of innumerable characteristics can be used for the treatment of groundwater, surface water, wastewater, and other water sources contaminated by toxic pollutants [8]. The size of nanoparticles plays a crucial role in the adsorption and desorption of nanomaterials [9]. With the advent of nanotechnology, nanofiltration, nanofiber filters, and carbon nanotubes are used for remediation allowing the detoxification of contaminants [10]. Cellulosic nanomaterials are utilized as efficient nanosorbents due to its renewability, low cost, sustainability, and biodegradability [11]. The metal and metal oxide nanomaterials have also found their way into wastewater treatment and have been used for some time. Metal nanoparticles of silver, gold, and metal oxide nanoparticles of titanium dioxide, zinc oxide, and aluminum oxide are also used in disinfection and decontamination processes. The other nanoparticles used are magnetic nanoparticles, having high surface area, high reactivity, and strong adsorption capacities [12]. Magnetic nanoparticles are mostly employed for the removal of heavy metals. Nanoparticles are also used as nanoadsorbents and as components of core-shell structures [13]. Nano zero-valent iron particles are used for the remediation of groundwater which is mostly contaminated with perchlorates and hydrocarbon fluids. The advancement of nanotechnology into wastewater treatment is also visualized in the form of nanofiltration membranes [14], created from thin polymer films. Nanofiltrations are characterized by the charge-based repulsion mechanism and are applied mostly to reduce hardness, odor, color, and heavy metal ions from groundwater. Another advent of nanotechnology is the use of nanocomposite membranes, which are based on the membrane structure and location of nanomaterials. These nanocomposites are classified into conventional nanocomposites thin-film nanocomposites [10], and surface-located nanocomposites. Research is underway to enhance the use of nanotechnological products in removing micro- and nanoplastic from the drinking water [15].

Polymers gained much importance in wastewater treatment owing to its properties and versatility. Today, polymer-based nanocomposites are applied for the removal of toxic substances. Both natural and synthetic polymers are playing a key role in wastewater treatment, but natural polymers garnered much of the attention as they are cheap and more effective [10]. Natural polymers/biopolymers have specific structure, physiochemical properties, chemical stability, and high reactivity. The presence of functional groups helps in the synthesis of new bioadsorbents which shows higher affinity towards hydrocarbons and metals. Among the biopolymers, polysaccharides are put into much use due to their ecofriendly nature, biodegradability, non-toxicity, and so on. They are also capable of binding to different molecules through physical and chemical interactions [16]. This adsorption capacity makes them an ideal candidate for water treatment. Chitin and chitosan are the most studied and experimented polysaccharides for the removal of pollutants, especially water-soluble pollutants, metal ions, and organic pollutants [17]. Chitin and chitosan are also cost-effective, and hence, there is much focus on the use of these polymers.

2. Chitin

Chitin and chitosan are the second most abundant polysaccharide with distinctive chemical, physical, and biological properties. Chitin, a poly (β-(1–4)-N-acetyl-D-glucosamine), was first identified during 1884 [18]. Chitin is white, hard, and inelastic in nature. It is found as crystalline microfibrils that form certain crustaceans' structural components and on yeast and fungi [19]. It is also found in other lower-living organisms such as house cricket (Brachytrupes portentosus) [20]. Even though chitin occurs in other living forms, it is widely extracted from crustaceans' shell. Newer extraction processes from other living organisms are much researched due to the growing demand. Chitin, the homopolymer, occurs in 3 forms, namely, chitin-α (antiparallel chains), chitin-β (parallel chains with intrasheet H-bonding), and chitin-γ (both parallel and antiparallel chains) [21]. The third form γ-chitin is rather seen as a combination of both α and β forms. α-Chitin is mostly found in the exoskeleton of crustaceans, yeast cells, and arthropod cuticles and is the most abundant polymorph, while β-chitin is extracted from squid pens. β-Chitin can be easily converted to its α-form [22]. Chitin is insoluble in inorganic and organic solvents due to the strong inter- and intramolecular hydrogen bonding network. As chitin is insoluble, chitosan, the deacetylated product of chitin, has garnered attention and is used in most industries.

3. Chitosan

Chitosan is one of the most important derivatives of chitin and is obtained through deacetylation. Chitin is abundant in nature, but chitosan is only present in trace amounts and is derived from chitin [23]. Chitosan is a linear polymer of D-glucosamine and N-acetyl-D-glucosamine. Chitosan contains many functional groups such as amino and hydroxyl groups, the reason for its flexibility and being a choice of different applications. Morphologically, chitosan is found in many different forms like crystalline, semicrystalline, and unorganized. Its molecular weight is between 300 and 1000 kDa [24], which depends on the source of chitin.

3.1. Structure. Chitin and chitosan are similar to cellulose but differ in their properties. The molecular formula is depicted as $(C_6H_{11}NO_4)n$ [25]. Deacetylation of α-chitin

results in removing acetyl groups from chitin, thereby leading to the formation of amino groups, the end product being chitosan. Chitosan is a co-polymer of β-(1⟶4)-2-acetamido-D-glucose and β-(1⟶4)-2-amino-D-glucose N-acetyl glucosamine and glucosamine, the two usual sugars, whose proportion depends on alkaline treatment. It contains one primary amine and two hydroxyl groups for each monomer [26]. Chitosan is chemically active due to repeated primary and secondary hydroxyl groups, and an amine group on the deacetylated unit. D-glucosamine contains a free amino group, and they take up a positive charge. This attributes to the properties like antimicrobial property and solubility [26].

In solid state, chitosan is a semicrystalline polymer which is white or slightly yellow in appearance. In solid state, chitosan molecules are crystallites of high order containing two major crystalline polymorphs. Chitosan is crystalline, which makes it accessible to reagents [27]. Chitosan has two forms, namely, the hydrated form named "tendon chitosan" and the anhydrated form named "annealed chitosan." These chitosan forms contain two antiparallel chitosan molecules accommodating a two-fold helix conformation, which is stabilized by the hydrogen bonds. Water molecules present in between the crystal cells stabilize the structure by multiple hydrogen bonds. The tendon form of chitosan can be transformed into an annealed form by heating, which is reversible [3].

Chitosan exhibits four crystalline polymorphs. The structural properties of chitosan are similar to that of chitin. As it is polycationic, it allows the formation of various complexes. Chitosan is nonthermoplastic; it degrades before melting [28]. Chitosan is insoluble in water and most organic solvents, but soluble in aqueous acid solutions such as citric, formic, acetic, and lactic acids and also in solvents like 10-camphor sulfonic acid, p-toluene sulfonic acid, and dimethyl sulfoxide. Chitosan is mainly characterized by the degree of deacetylation and molecular weight [29]. These affect the biological and physiochemical properties of chitosan. Chitosan is differentiated from chitin by its degree of N-acetylation and the presence of amino groups. When the acetylation degree is less than 50%, the polymer is chitosan [28].

4. Properties of Chitosan

Certain specific properties of chitin and chitosan make it a versatile substance for application in different fields. As chitosan is a deacetylate product, most researchers consider the product as chitosan when the degree of deacetylation is greater than 70% [28]. There is a need for a precise method to evaluate the physicochemical properties of chitosan. Most properties of chitosan are affected by the molecular weight and the degree of deacetylation. Chitosan is susceptible to chemical modifications [30]. The high charge density is pH 6.5. As chitosan has varied applications, the properties have a vital role to play on the same.

4.1. Physicochemical Properties

4.1.1. Structure. Chitosan molecules are mostly organized in highly ordered crystallites in amorphous regions. As mentioned above, two kinds of crystalline polymorphs exist: the tendon chitosan and the annealed chitosan [19]. There are reports of up to four crystalline polymorphs of chitosan with organic and inorganic acids. In these polymorphs, the anhydrous Type I salts, in the chitosan backbone chain, retain the twofold helix of the unmodified chitosan molecule. This is the Type I form, and when conformational changes occur by salt formations of types II, IIa, and III, the chains get arranged in antiparallel helicoids of the differentiated fold [30].

4.1.2. Molecular Weight. The molecular weight determines most functional properties of chitosan. Molecular weight and degree of acetylation form the most significant characteristic of chitin and chitosan. Both these make an impact on the functional properties on chitosan either in solid state or solution. Molecular weight mostly affects the hydrated colloidal forms and the viscoelastic properties of solutions [19]. Research shows that high-molecular-weight chitosan exhibits better elongation and stability than others; membrane crystallinity and molecular interactions are higher than low-molecular-weight chitosan. The molecular weight of chitosan is determined using viscometry, light scattering method, HPLC, and so on. As chitosan's molecular weight influences the properties, chitosan may be available in the molecular weight range of 3-4 orders. The molecular weight of chitosan can be reduced by chemical, physical, or enzymatic hydrolysis [19].

4.1.3. Degree of Acetylation. The degree of acetylation determines most properties of chitosan. The most notable change is that chitosan becomes polycationic in acidic media as the amino groups are ionizable. The degree of acetylation determines most functional properties such as the extent of swelling, solubility, biocompatibility, biodegradation, and bioactivity. As the degree of acetylation is a very important criterion, it is important to determine it to analyze chitosan quality [19]. The degree of Acetylation is mostly characterized by UV spectroscopy, potentiometry, and ^{1}H-NMR infrared spectroscopy [19].

4.1.4. Functional Properties. The above-mentioned chemical properties of chitosan contribute to distinctive properties. The N-acetyl glucosamine groups of chitosan for form hydrophobic interactions and hydrogen bonds which in turn stabilizes the molecule with supplementing rigidity and reinforcing the structure. Some functional properties of chitosan are given as follows.

4.1.5. Solubility. Chitosan is soluble in aqueous media; it is considered a weak base. This is because the amino groups distributed in the chitosan molecule are protonated, getting a charge density as high as one cationic charge per

glucosamine unit. Diluted inorganic acids except sulfuric acid are suitable solvents for chitosan [19]. Chitosan is insoluble in nonpolar organic solvents. Chitosan thermally degrades before attaining the glass transition phase, and hence, the preparation of gels, sponges, films, fibers, and so on is carried out through chitosan solutions [19].

4.1.6. Adsorption Capacity. The process involving ionic, hydrogen, hydrophobic bonding, or Van der Waals force is known as adsorption. The functional groups of chitosan generate interactions with various molecules. Adsorption capacity depends on its physicochemical characteristics and the characteristic of the adsorbate. Chitosan is known for its adsorption capacity towards metal ions and is hence used in various waste management systems [31].

4.1.7. Viscosity. Viscosity determines the extent of penetration, and the molecular weight plays a significant role in determining the viscosity. Viscosity increases with the degree of acetylation. It decreases with storage time and temperature and also in the presence of an electrolyte. When the particle size is lesser, the viscosity is lower [32].

4.2. Biological Properties. The biological properties exhibited by chitosan are mostly due to the physicochemical properties. They are nontoxic, biodegradable, and biocompatible and have high humidity adsorption. Chitosan is biodegradable naturally by enzymes such as chitinases and chito biases which are found in prokaryotes and higher animals. Chitosan is considered biocompatible as it does not hamper the living systems which come in close contact to it. The toxicity LD50 is about 16 g/kg similar to salt and sugar toxicity [28]. The biocompatibility of chitosan attributes to the presence of N-acetyl glucosamine which is structurally similar to glycosaminoglycans. The bioactivity of chitosan is another aspect of interest. Chitosan exhibits varied biological activities including antibacterial, antiviral, and antifungal, which are of biomedical interest [33].

5. Extraction of Chitin and Chitosan

5.1. Extraction of Chitin. Chitin and chitosan are extracted mainly by two methods: chemical and biological methods. The factors and conditions that control chitin's characteristics are purity, degree of deacetylation, polydispersity index, and molecular weight [28]. The major sources for the production of chitin and chitosan are the crustaceans mainly crab and shrimp. Also, they are found in the cell wall of certain fungi and insects. The chemical extraction method is highly applied for commercial purpose even though it affects the properties of chitin and is hazardous to the environment. The chemical extraction method is given in Figure 1.

The chemical extraction method involves the following steps: deproteination, demineralization, and discoloration. Deproteination involves the depolymerization of the biopolymer using chemicals to break the chemical bond between the protein and the chitin [34]. Many types of chemicals such as NaOH, KOH, and Na_2CO_3, and are used as deproteinizing agents, and the reaction condition may vary for each of them. NaOH is most commonly used, resulting in partial deacetylation of chitin and lowers the molecular weight by the biopolymer's hydrolysis. The next step is the demineralization, where minerals mainly calcium carbonate is removed by the treatment of strong acids. The acids commonly used are H_2SO_4, HNO_3, HCl, HCOOH, and CH_3COOH [35]. This process release of carbon dioxide occurs by the decomposition of calcium carbonate into calcium salts by treating with hydrochloric acid [36]. Following this is the discoloration process, which is the additional step in the extraction process. This is done to remove the pigments such as β-carotene and astaxanthin from the extraction source to get the colorless product. Organic or inorganic solvents such as sodium hypochlorite, hydrogen peroxide, and acetone are used for this purpose.

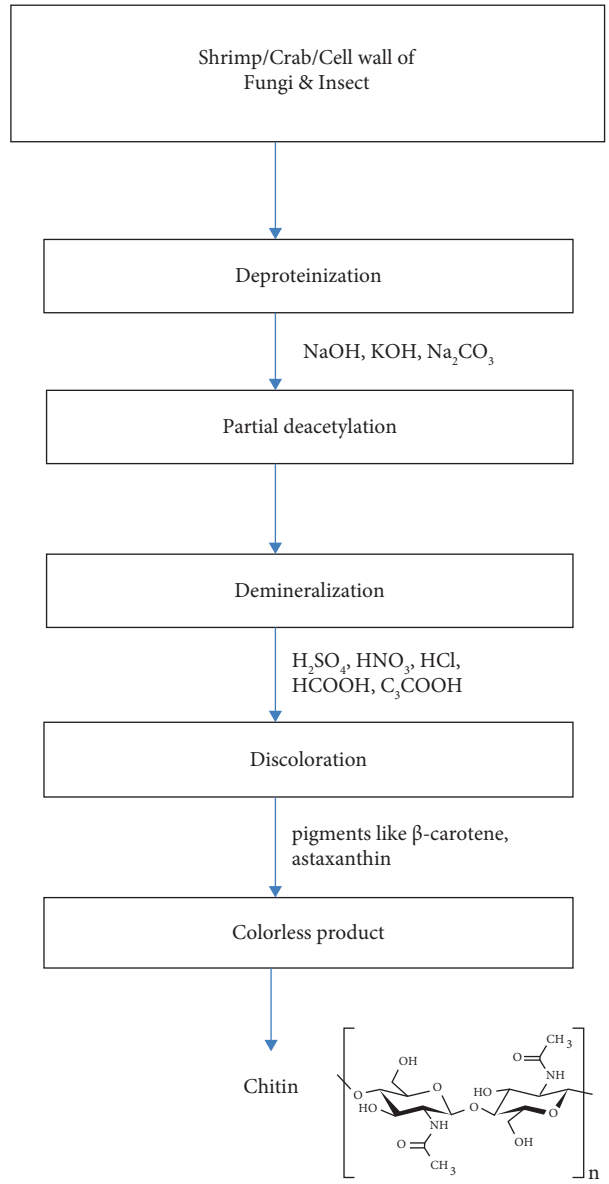

Figure 1: Schematic representation of chemical extraction of chitin.

Due to certain drawbacks in the chemical extraction process, the biological method thrives more attention in selecting the utilization of enzymes and microorganisms to extract chitin [37]. This method is ecofriendly and does not alter the structure of chitin. In this method, deproteination is employed by using proteolytic microorganism (Figure 2). The most widely employed methods for chitin extraction are enzymatic deproteinization and fermentation using microbes [38]. Enzymatic deproteination involves removing protein during the extraction of chitin using the proteolytic enzyme such as proteases. The primary sources of proteolytic enzymes are plants, animals, and microbes. In this process, various proteases are pepsin, alkalize, trypsin, papain, pancreatin, and so on [39].

Fermentation using microorganism is another process involved in this method of extraction. Here, the specific microbe can be selected and used for this process, and involves two types of approaches: lactic acid fermentation and nonlactic acid fermentation. In lactic acid fermentation, Lactobacillus sp. strain is used where lactic acid is acquired by modifying the glucose with a subsequent decrease in pH that prohibits the growth of spoilage microorganisms.

Lactic acid thus reacts with calcium carbonate and forms calcium lactate precipitate, recovered and washed with water. Many factors such as the carbon source and its concentration, temperature, amount of the inoculums, and initial and progress in pH are responsible for this process's productivity [40]. In nonlactic acid fermentation, both fungi and bacteria such as *Aspergillus spp.*, *Bacillus spp.*, and *Pseudomonas spp.* are involved. Various features may influence the fermentation process, thereby increasing deproteination and demineralization efficiencies [33].

6. Conversion of Chitin to Chitosan

Chitosan is the polymers' family obtained by the deacetylation of chitin using acid solution treatment and alkaline hydrolysis. Here to chitin can be converted to chitosan by either chemical or enzymatic [41]. In the chemical deacetylation process, chitin is deacetylated with the help of alkali or acids. Since glycosidic bonds are susceptible to acids, alkali deacetylation is more commonly used [42]. The deacetylation process is accomplished either by homogeneous or heterogeneous methods. In the heterogeneous method, chitin is added with hot concentrated NaOH for a few hours, and thereby the insoluble chitosan is obtained, which is deacetylated up to 85%–99%. In the homogeneous method, chitin is dispersed in concentrated NaOH at about 25°C for about 3 hours to prepare alkali chitin and then suspended in crushed ice at 0°C. Here, soluble chitosan, which is deacetylated up to 48–55% is obtained. The alteration in chitosan preparation may result in changes in viscosity, acetyl group distribution along the chain, molecular weight, etc. [43]. In the enzymatic deacetylation process, chitin is deacetylated with the help of the enzyme chitin deacetylase. This enzyme hydrolyses the N-acetamido bonds in chitin to form chitosan. Nevertheless, this enzyme was less effective in the naturally occurring chitin, which is crystalline and insoluble. To overcome this, crystalline chitin undergoes certain pretreatments such as grinding, heating, and sonication. The carbon and hydrogen structures are given in Figure 3(a) and the mechanism of chitin is given in Figure 3(b).

6.1. Chitosan Modification. Chitosan is a unique cationic polysaccharide which can be easily functionalized to different derivatives by chemical, radiation, and enzymatic methods (Figure 4). Of these various modification techniques, chemical modification technique is more widely employed. Even though chitosan has many functional properties and other biological activities, its application is limited due to its low solubility owing to its rigid crystalline structure. This problem can be overcome by modifying chitosan by chemical or other enzymatic methods to produce new derivatives. The molecular weights, degree of deacetylation, and crystallinity are the main features in chitosan, where the modification could be done to form a difference in their physiochemical properties [29].

The chemical modification could enhance the physical and chemical properties because of the hydroxyl and amino groups in chitosan. The most commonly used chemical alteration of chitosan is N-substitution, where the functional group of chitosan that reacts is the amino group. Also, O-substitution is often employed. The chemical reactions involved in this modification are quaternization, acylation, alkylation, phosphorylation, hydroxylation, graft copolymerization, and so on [45]. A chemical modification also retains the essential properties of chitosan and increases the chitosan derivatives' application.

The most commonly used chemical modifications of chitosan are as follows: (i) N-substitutions without protective agents, where the amino group is transformed to quaternary ammonium salts through the chemical reaction with quaternary phosphonium or quaternary ammonium compounds, resulting in the formation of derivatives with enhanced water solubility and biological properties due to the positive charge which is permanent on the polymer. N, N, N-Trimethyl chitosan chloride (TMC) is one of the most crucial quaternary chitosan derivatives [46]. The additional method applied is N-alkylation and N-arylation accomplished by the Schiff base intermediates between the amino group of chitosan and the aldehyde and ketone accompanied by Schiff's reduction base intermediates. N-phosphorylation is also another crucial reaction for improving the chemical and biological property of chitosan. (ii) N-substitution using protective agents, where the -OH groups are protected by the chemoselective methods to synthesize homogeneous N-quaternarized chitosan derivatives [46]. (iii) O-substitution using protective agents, here, chemical modification intrudes with the amino group of chitosan which would influence the bioactive properties. In such a manner, N-phthaloylation with phthalic anhydride enables chemical modification because of the phthaloyl group becomes deprotected efficiently to rejuvenate the free amino groups, enhancing the solubility of chitosan [47]. (iv) N, O substitutions, where the process involved is carboxylation, which is performed in two ways i.e., C6-hydroxyl oxidation and C2-amino substitution to make the insoluble chitosan to

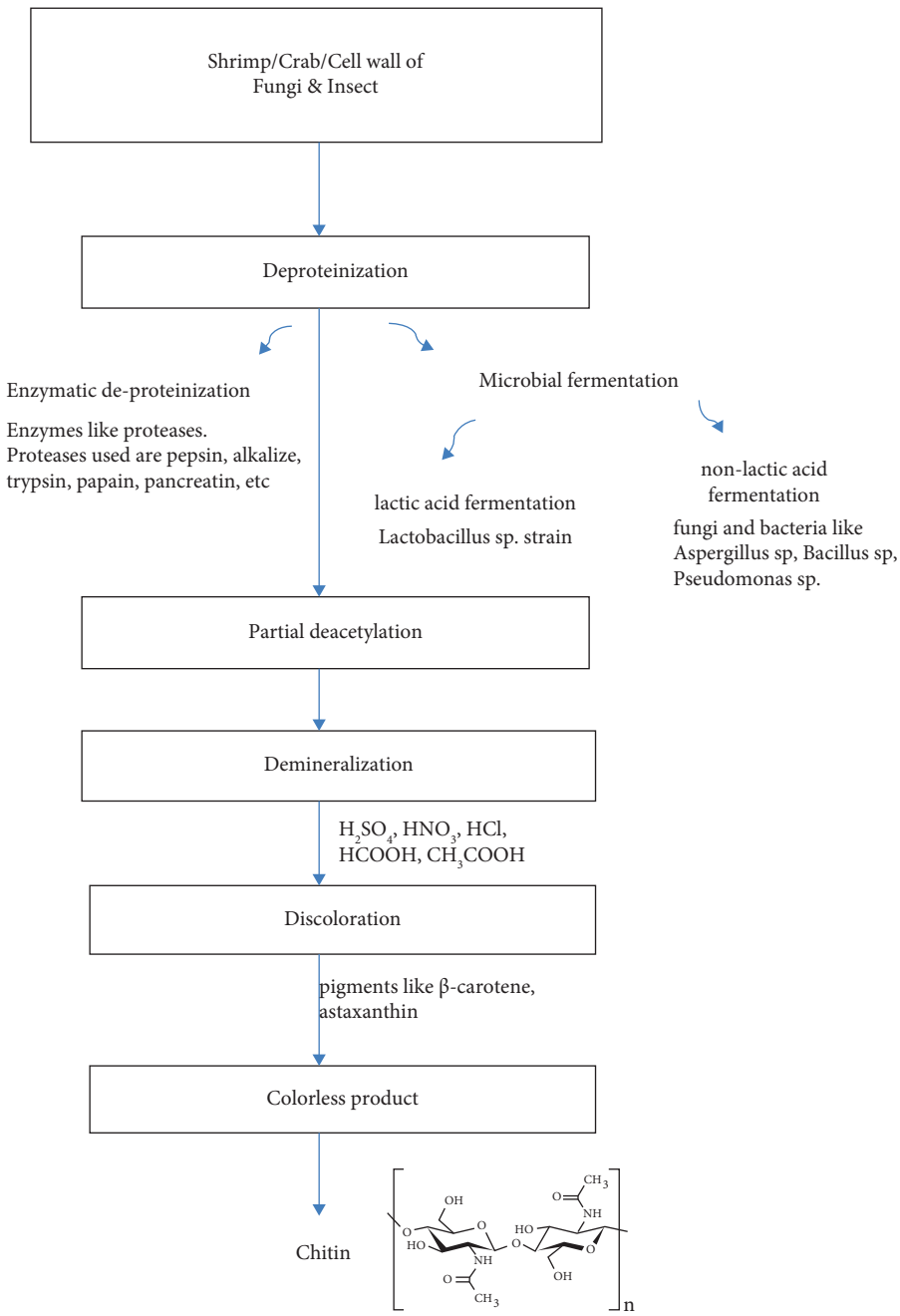

Figure 2: Schematic representation of biological extraction of chitin.

soluble ones. (v) Cross-linking reaction of chitosan, where the cross-linking agents generate ionic bonds or physical cross-linking resulting in a strong three-dimensional structure. Low-molecular-weight chitosan is subjected to cross-linking to obtain appropriate structural, thermal, and mechanical properties [48].

Chitosan is chemically modified by attaching photosensitizers, sugars, dendrimers, crown ethers, and cyclodextrins onto the polymer backbone. Photosensitizers are utilized when the light of a certain wavelength which is not readily available is required for a reaction. Even though synthetic polymers are mostly employed, in the year 1980, Tanaka et al. have reported the first synthesized photosensitive polymer derived from chitosan and from then, several studies were reported about its production [49]. The photoactive biopolymer can be employed as a biomineralization tool exploiting their photoexcitation mechanism in dental/bone repair. Dendrimers are members of polymers which are symmetrical macromolecules and are highly branched with multifunctional properties. The polymers could be dendronized through two approaches; they are attached to the to-process and macromonomer process. Dendronized chitosan was found to be very effective as a nonviral gene delivery vector [50]. Modifications of chitosan using

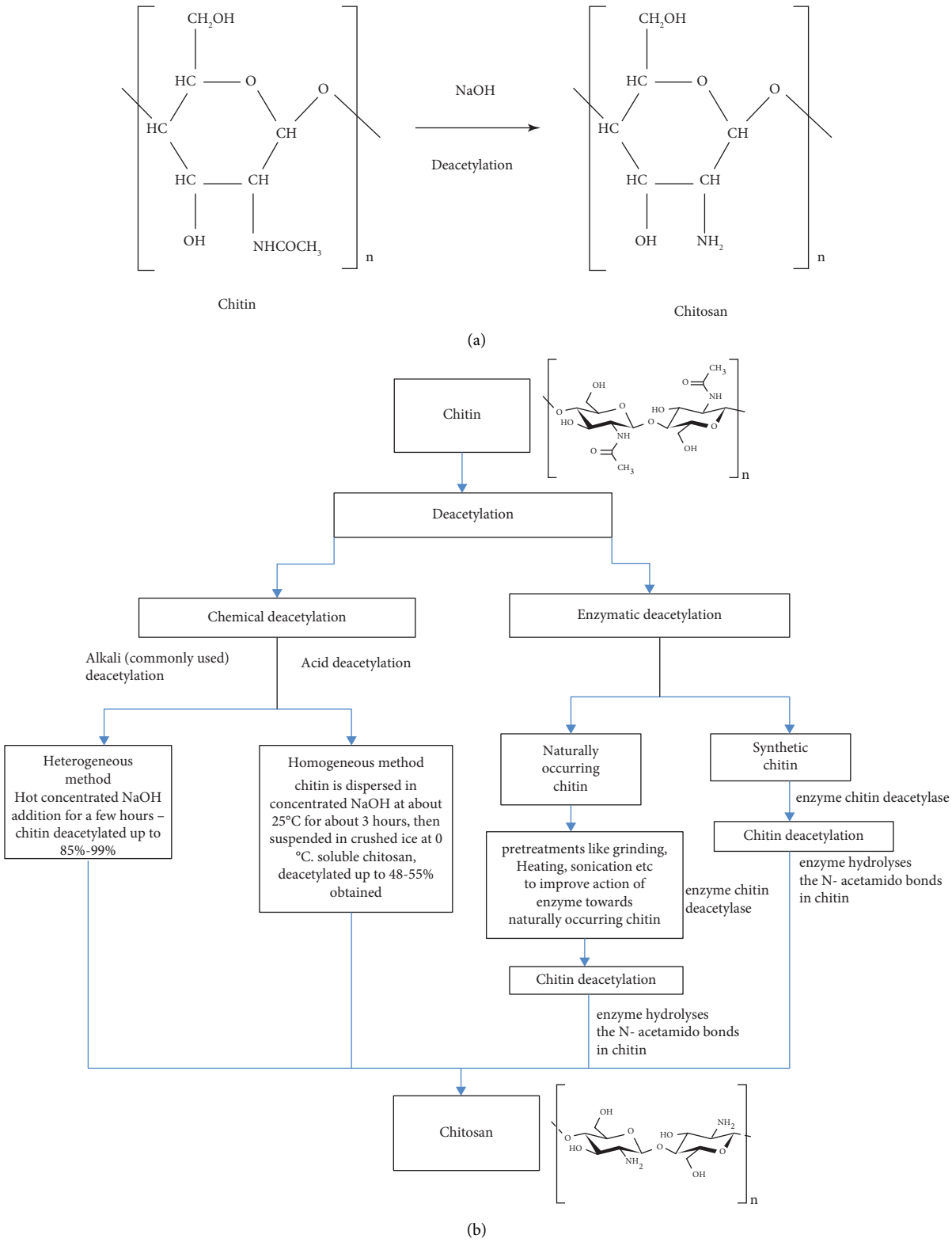

FIGURE 3: (a) Conversion of chitin to chitosan (molecular structural representation) [44]. (b) Pictorial representation of mechanism of chitin to chitosan conversion.

cyclodextrins are done to combine the chitosan characters and properties of cyclodextrins altering their physical and chemical properties. Moreover, the modification of chitosan achieved by radiation includes radiation-induced polymerization, radiation cross-linking, and changes in the polymers' morphology. Various other modifications are

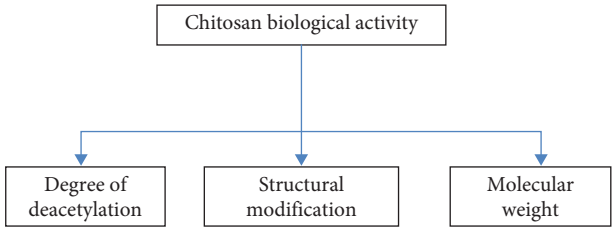

Figure 4: Pictorial representation of key factors influencing activity of chitosan and its derivatives.

enzymatic modification, plasma-induced modification, etc. [28].

Chitosan and the modified derivatives are utilized in various fields. Due to the lack of toxicity, biodegradability, biocompatibility, and low allergenicity, chitosan derivatives are applied for various purposes. Due to these biological properties, they are utilized in drug delivery, and this nanoparticulate drug delivery is well suited for the treatment of various types of cancer [51]. Chitosan and its derivatives can also be utilized as an essential element in tissue engineering due to their ease of chemical modification, porous structure, and gel formation [4]. It is also employed in cosmetics for oral health care, hair care, and skin. They may also exhibit antimicrobial, antioxidant, and anti-inflammatory activities [52].

7. Chitosan Nanocomposites

Nanocomposites are multiphasic materials, where at least one phase has a dimension in the range of 10–100 nm. In short, nanocomposites are building blocks with dimensions in the nanometer range with unprecedented flexibility and improvement in their physical properties. Nanocomposites' properties have substantial improvements due to the dissimilarities of the structure and chemistry [53]. Nanocomposites show increased thermal stability, mechanical properties, permeability, electrical conductivity, enhanced optical clarity, surface appearance, and increased chemical resistance. Nanocomposites are produced by blending fullerenes, inorganic nanoclusters, metal oxides, semiconductors, or clays with biological molecules, organic polymers, organometallic compounds, and sol-gel-derived polymers [54]. Nanocomposites are classified into polymer-based nanocomposites and nonpolymer-based nanocomposites. Polymer nanocomposites are further divided as ceramic, organic/inorganic, organic/inorganic-hybrid, and layered silicate. Nonpolymer-based nanocomposites are further classified as metal nanocomposite, ceramic nanocomposite, and ceramic-ceramic nanocomposite [34].

Recent improvements have led to the emergence of chitosan-based nanocomposites, wherein both the polymer and nanoparticle contribute to specific properties. The presence of nanoparticle in the chitosan polymeric matrix improves its intrinsic properties such as mechanical, chemical, and physical stability. It also endows chitosan with extraordinary physicochemical properties and high surface area. Chitosan nanocomposites are mostly created between chitosan and carbon, clay, polymer, metal/metal oxide materials through chemical or physical interactions [32]. The nanocomposite classification is given in Figure 5.

Chitosan nanocomposites are synthesized through both wet and dry methods. Most metal-chitosan nanocomposites are synthesized using related reducing salts. The physical method of polymer modification is the easiest process, where two or more polymers are blended to form a new material showcasing different physical properties [32]. Different physical methods such UV, radiolysis, and sonochemistry are employed for physical methods. Under chemical methods, electrochemical irradiation, chemical reduction, thermal decomposition, and green chemistry are the approaches undertaken to create chitosan nanocomposites [30]. Biosynthesis of chitosan nanocomposites is also much appreciated and used method due to the cons of physical and chemical methods. Nanocomposite preparation and their application are given in Figures 6 and 7.

8. Chitosan Nanocomposites for Wastewater Treatment

Chitosan by itself was used in water purification processes for many years. Chitosan effectively removes heavy metals, oil spills, and fine particulate matter from wastewater [19]. Also, chitosan and its derivatives have higher adsorbing and chelating effects and can adsorb or capture heavy metals. Chitosan also effectively adsorbs radioactive elements. And, chitosan is a natural polymer flocculant which helps in flocculating the active ingredients for reuse [11]. This led to chitosan being used along with nanoparticles to form nanocomposites for wastewater treatment. Chitosan-based materials are of much focus as the functional nanoparticles in them are used in both environmental and other applications. Chitosan nanocomposites are used in wastewater treatment from the removal of different pollutants which cause harmful effects to the environment and the population. Some aspects of chitosan nanocomposite and the different pollutants they remove are discussed here, along with the recent advancements in the particular area.

8.1. Heavy Metals. Heavy metals also known as trace elements or metallic elements, are elements that have an atomic density of 6 g/cm^3 or greater. The most toxic heavy metals that pose serious risk to the environment present in the wastewater are lead, arsenic, cadmium, chromium, copper, nickel, zinc, silver, and so on [55]. Along with causing environmental and health issues, it also creates an upsurge in the treatment costs of wastewater. Many different adsorbents are used for effective removal of heavy metals, but with the recent trends in nanotechnology, and the modifications of natural polymers, chitosan nanocomposites are used effectively to remove heavy metals. This is because chitosan is nontoxic and alkali- and corrosion-resistant. The presence of active groups of chitosan effectively adsorbs the heavy metals, and when coupled with nanoparticles, chitosan composites can be recycled.

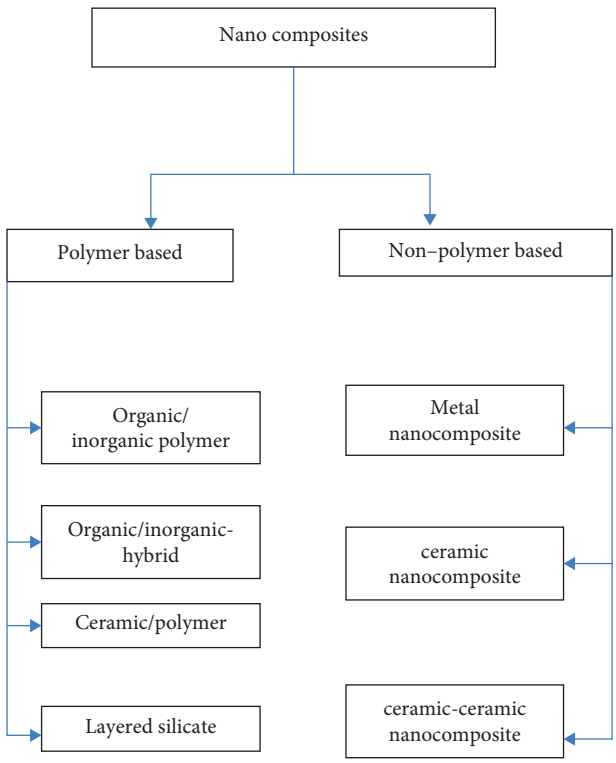

Figure 5: Pictorial representation of nanocomposite classification.

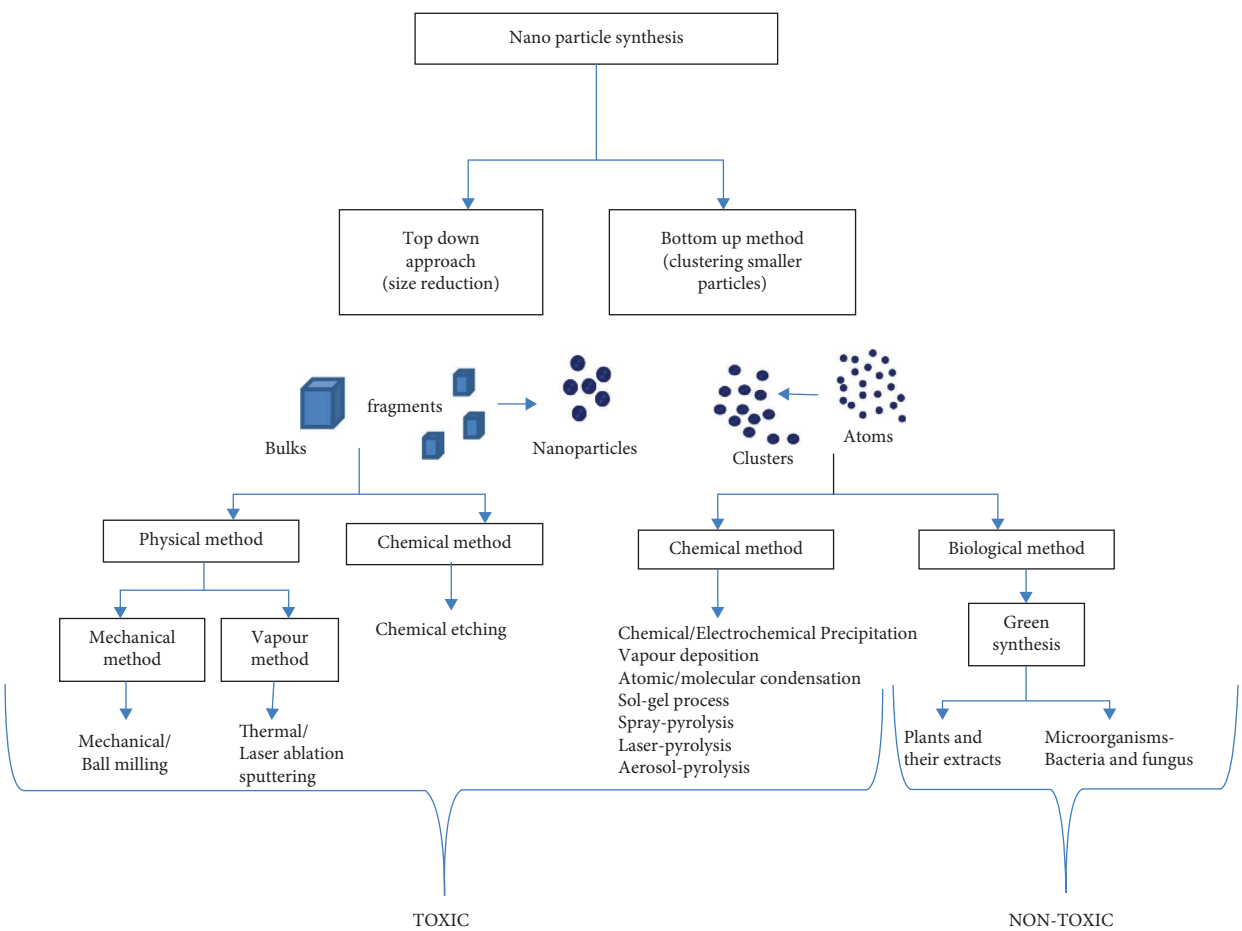

Figure 6: Pictorial representation of various methods of chitosan nanocomposites preparation.

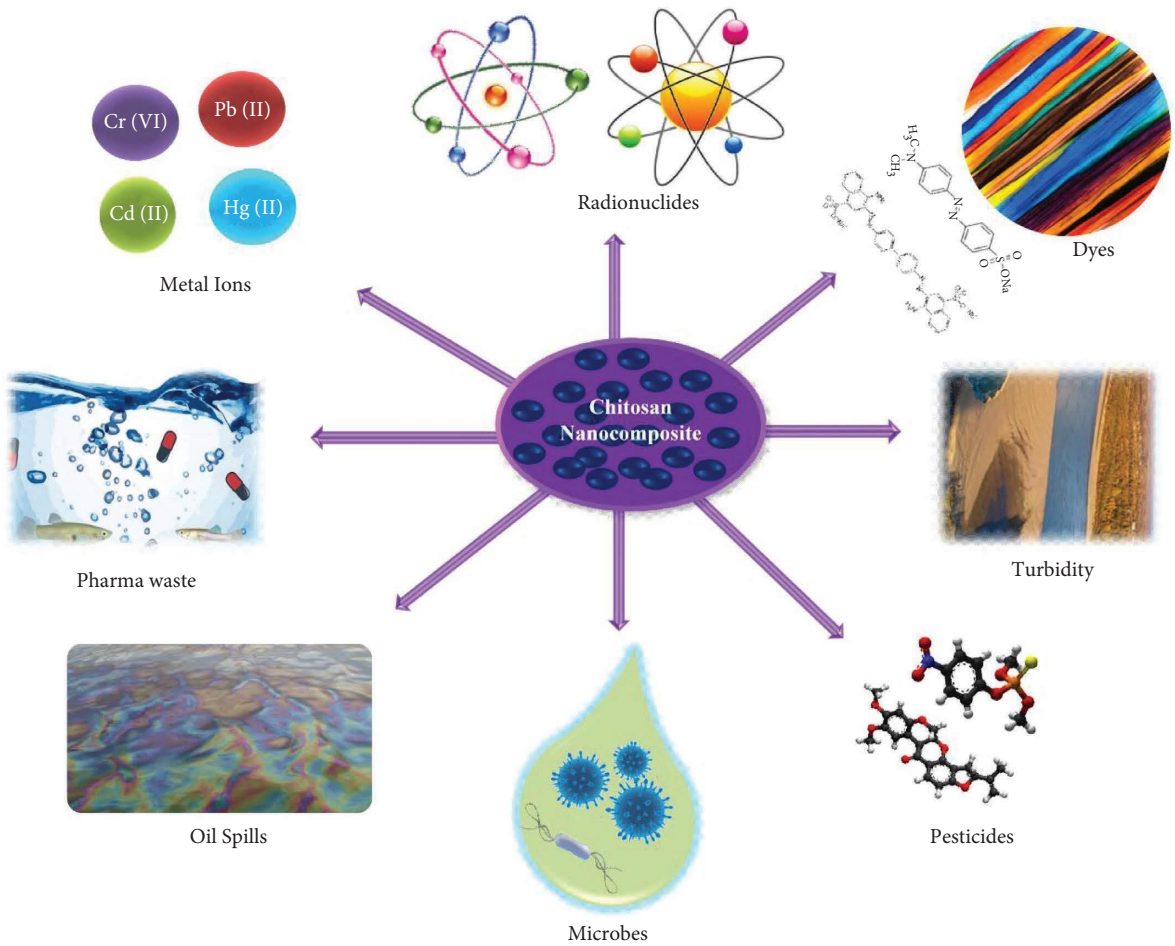

Figure 7: Various application domains of chitosan nanocomposites.

Lead, which is widely used in the electroplating and metallurgy industries, and also other industries contaminates the water and remains in the environment indefinitely. Hence, there is a need to recover lead from contaminated water. Lead remains in the environment [56]. While combining polyacrylic acid along with chitosan, the acidity resistance increases and with the incorporation of a magnetic nanoparticle, a magnetic nanocomposite is formed. This magnetic nanocomposite formed showed higher adsorption activity with a maximum adsorption capacity of 204.89 mg/g. The reaction followed a pseudo-second-order kinetics and fitted the Langmuir isotherm model [11]. Removal of lead, cadmium, and mercury ions from continuous flowing wastewater was a challenge, and this was made possible with taking inspiration from nacre. A multilayered hydroxyapatite/chitosan composite had high mechanical strength and could with stand high pressure while effectively adsorbing the heavy metal ions. Efficient removal of lead ions was noticed in this study [11].

Hexavalent chromium is mutagenic. Chromium also causes diarrhea, kidney dysfunction, and stomach cramps. It also affects the aquatic life. Effective adsorption of chromium was noticed while using chitosan-MnO_2 nanocomposite with a maximum adsorption capacity of 61.56 mg/g. Chromium adsorption includes both monolayer and multilayer adsorptions. Effective adsorption of chromium is due to the electrostatic attraction between the positive charge on the surface of the nanocomposite and the anions of chromium [57]. Effective removal of chromium was also observed while using two different functionalized nanocomposites with an adsorption capacity of 61.35 mg/g and 58.14 mg/g [58]. Removal of chromium was also facilitated using triethylenetetramine-modified hollow Fe_3O_4/SiO_2/chitosan magnetic nanocomposites which were created the facile way. The adsorption capacity exhibited was notable and was higher than most adsorbents [58]. Removal of different heavy metal ions such as Pb (II), Cd (II), and Hg (II) were carried out with chitosan-boehmite desiccant nanocomposite which was synthesized using one pot sol-gel route. This particular nanocomposite is reusable and has excellent adsorption capacities [58]. Arsenic causes many health hazards and constant inhalation of Arsenic leads to skin cancer. Effective adsorption of Arsenic from aquatic environment was observed while using a goethite/graphene oxide/chitosan nanocomposite with a maximum adsorption capacity of 289.42 mg/g, as given in Table 1.

Table 1: Various chitosan nanocomposite data for removal of metal ions.

Nanocomposite	Metal ion	Adsorption capacity	Isotherm model	Kinetics	Adsorption equilibrium time	References
Polyacrylic acid grafted magnetic chitosan nanocomposite	Pb (II)	204.89 mg/g	Langmuir model	Pseudo-second-order	70 min	[59]
Chitosan-MnO_2 nanocomposite	Cr (VI)	61.56 mg g1	Langmuir model	Intra diffusion model	120 min	[60]
Modified chitosan cinnamaldehyde nanocomposite	Cr (VI)	61.35 mg/g	Langmuir model	Pseudo-second-order	35 min	[61]
$NTiO_2$-chitosan@$NZrO_2$-chitosan nanocomposite	Sm (III)	650 μg/mol	Langmuir-freundlich	Pseudo-first-order	30 min	[62]
Triethylenetetramine-modified hollow Fe_3O_4/SiO_2/chitosan magnetic nanocomposites	Cr (VI)	254.6 mg	Langmuir	Pseudo-second-order	15 min	[63]
Chitosan-boehmite desiccant composite	Pb (II), Cd (II), Hg (II)	—	Langmuir	Pseudo-second-order	—	[64]
Chitosan modified molybdenum disulfide composites	Eu (III)	0.86 mmol/g	Langmuir	—	240 min	[65]
Magnetite modified chitosan cinnamaldehyde nanocomposite	Cr (VI)	58.14 mg/g	Langmuir model	Pseudo-second-order	80 min	[61]
Nacre-inspired hydroxyapatite/chitosan layered composites	Pb (II), Cd (II), Hg (II)	—	Elovich	Pseudo-first and second-order	6 days	[22]
Goethite/graphene oxide/chitosan nanocomposite	As (III)	289.42 mg/g	Freundlich and sips models	Pseudo-second-order	3000 min	[51]
$NTiO_2$-chitosan@$NZrO_2$-chitosan nanocomposite	Gd (III)	450 μg/mol	Langmuir-Freundlich	Pseudo-first-order	20 min	[62]
Chitosan modified molybdenum disulfide composites	Cr (IV)	3.04 mmol/g	Langmuir	—	180 min	[65]
Melamine grafted chitosan-montmorillonite nanocomposite	Fe^{3+}	125.79 mg/g	Freundlich	Pseudo-second-order	120 min	[66]
Chitosan modified molybdenum disulfide composites	U (VI)	0.71 mmol/g	Langmuir		120 min	[65]

This was due to the presence of O–NHCO-, C-O, O-H, and Fe-O groups, but the major contributor was the complexation between as (III) ions and hydroxyl iron oxide [67]. Removal of trivalent gadolinium and samarium ions was done effectively by green synthesized novel $NTiO_2$-Ch@ $NZrO_2$-chitosan nanocomposite. This nanocomposite has good sorption properties [62]. Ferric ion adsorption with the help of melamine grafted nanocomposite synthesized through graft polymerization showed effective adsorption capacities. Water contaminated with uranium causes deformity of bones and chronic kidney disease. Effective removal of U (VI), Eu (III), and Cr (VI) were carried out using chitosan modified molybdenum disulfide prepared through disulfide method. The removal of the metal ions is mainly due to the electrostatic attraction between the hydroxyl and the amidogen group [65].

8.2. Dye Removal. Dyes are used in many industries such as printing, textile, and painting which are the root causes for contaminating the water [68]. Most of the dyes that enter the water environment are toxic and may affect the photosynthetic activity by reducing the sunlight penetration that negatively affects the aquatic life and human life. So, it is essential to remove these dyes and protect the environment. For this, several physical, chemical, and biological methods are employed. Of these methods, adsorption is considered to be the most common physiochemical method used for this purpose. Various adsorbents are used for the dye removal; among them, chitosan is used due to the presence of its functional group and an abundant biopolymer in nature. It also undergoes several modifications and combines with other nanoparticles to form nanocomposite to overcome its various limitations.

Remazol brilliant blue R dye (RBBR) is a harmful dye from the textile industry which affects the aquatic life, and therefore, it is necessary to remove it from the contaminated water. For this, a desired and recoverable bioadsorbent was developed that is a new magnetic Schiff's base-chitosan-benzil/zinc oxide/Fe_3O_4 nanocomposite. In addition to various adsorption parameters, parametric optimization by Box-Behnken design was done to optimize the synthesis condition. Here, the maximum adsorption capacity was found to be 620.5 mg/g, and the kinetic and isotherm models were the pseudo-second-order kinetic model and Freundlich model [65]. Acid blue 25 is an anionic dye that could be removed from the contaminated water with chitosan polymeric nanocomposite (CS-PVA@CuO). Here, the adsorption kinetics fits into the pseudo-second-order model and the maximum adsorption capacity are 171.4 mg/g. Also, the adsorption isotherm fits the Langmuir model [69].

Direct red 81 is a toxic sulphonated azo dye present in the contaminated water removed with the help of the adsorbent chitosan/zero-valent nanocomposite (CS-nZVI). The adsorption isotherm fits into the Freundlich model, and the kinetics are the pseudo-first-order [70]. Congo red is another dye that is present in the water that is very toxic to human, on entering the human body. This dye gets metabolized to benzidine, a carcinogen to humans and should be removed from the water. The adsorbent ZnO/chitosan nanocomposite was created by the in-situ precipitation method. When coming in contact with the dye, the adsorbent gets adsorbed in a single monolayer, and its maximum adsorption capacity was found to be 227.3 mg/g. It was also found that the Congo red adsorption was better exhibited by the Langmuir model [71]. Reactive red 120(RR120) dye is another dye found in the aqueous environment and could be removed with the help of a bio adsorbent hybrid cross-linked chitosan-epichlorohydrin/ TiO_2 nanocomposite (CTS-ECH/TNC) which is an inorganic-organic hybrid nanocomposite. The adsorption data are finely demonstrated by pseudo-second-order kinetic and the Langmuir isotherm model. The maximum adsorption capacity of CTS-ECH/TNC for the dye RR120 was found to be 210 mg/g [72]. Malachite green is a cationic dye which is eluted from the contaminated water with the help of the adsorbent chitosan–zinc oxide composite. The isotherm model fits into Langmuir model and shows an adsorption capacity of 11 mg/g. The adsorption kinetics was found to be a pseudo-second-order model [73]. Methyl orange is one of the most stable azo dye presents in the wastewater. The removal of this dye is done with the help of chitosan-silica nanocomposite. The process of adsorption best fits with the Langmuir model with the maximum adsorption capacity of 7 mg/g [74]. Methylene blue is a cationic dye which on the accumulation in wastewater causes many adverse effects to both human and the water environment. Chitosan/silica/ZnO nanocomposite is an adsorbent used to remove this dye from the contaminated water. Here, the adsorption isotherm fit with the Langmuir model and the followed adsorption kinetics are the pseudo-second-order model. The maximum adsorption capacity is 293.3 mg/g [75]. Rose Bengal is an anionic dye which is present in the industrial wastewater. This dye is removed with the help of molecularly imprinted polymer (MIP) and chitosan-TiO_2 nanocomposite (CTNC). Here, the maximum adsorption capacity of the dye was found to be 79.369 mg/g. Also, the equilibrium data best fit to the Langmuir model and follows pseudo-second-order kinetics [76]. Direct blue 71 (DB71) and reactive blue 19 (RB19) are the two dyes that are adsorbed from the aqueous environment with the help of magnetic nanocomposite of chitosan/SiO2/CNTs (MNCSC). It was analyzed that the isotherm model is well fitted with the Langmuir model, and the kinetics are the pseudo-second-order model. The adsorption capacity of MNCSC for DB71 is 61.35 mg/g and for RB19 is 97.08 mg/g (Table 2) [78].

9. Other Contaminants

9.1. Pesticides. Pesticides used for plant and crop protection have resulted in yielding healthy and fruitful crops while polluting the environment [56]. The presence of pesticides poses adverse effects that vary with the concentration, contact time, and amount. These contaminants cause severe health hazards for humans too such as cancer, malformation, infertility, and DNA mutation [79]. Pesticides include insecticides, fungicides, biocides, and rodenticides [7]. The

Table 2: Different chitosan nanocomposites for removal of harmful dyes.

Nanocomposite	Dye	Adsorption capacity	Isotherm model	Kinetics	References
Chitosan-benzil/zinc oxide/Fe_3O_4 nanocomposite	Remazol brilliant blue *R* (RBBR)	620.5 mg/g	Freundlich model	Pseudo-second-order	[77]
Chitosan polymeric nanocomposite (CS-PVA@CuO)	Acid blue 25	171.4 mg/g	Langmuir model	Pseudo-second-order	[69]
Chitosan/zero-valent nanocomposite (CS-nZVI)	Direct red 81	61.35 mg/g	Freundlich model	Pseudo-first-order	[70]
ZnO/chitosan nanocomposite	Congo red	227.3 mg/g	Langmuir model	—	[71]
Chitosan-epichlorohydrin/TiO_2nanocomposite (CTS-ECH/TNC)	Reactive red 120	210 mg/g	Langmuir model	Pseudo-second-order	[72]
Chitosan-ZnO composite	Malachite green	11 mg/g	Langmuir model	Pseudo-second-order	[73]
Chitosan-silica nanocomposite	Methyl orange	7 mg/g	Langmuir model	—	[74]
Chitosan/Silica/ZnO nanocomposite	Methylene blue	293.3 mg/g	Langmuir model	Pseudo-second-order	[75]
Molecularly imprinted polymer (MIP) chitosan-TiO_2nanocomposite (CTNC)	Rose bengal	79.365 mg/g	Langmuir model	Pseudo-second-order	[76]
Magnetic nanocomposite of chitosan/SiO_2/CNTs (MNCSC)	Direct blue 71 (DB71) reactive blue 19 (RB19)	97.08 mg/g	Langmuir model	Pseudo-second-order	[78]

presence of residues and metabolites of the pesticides impacts the water environment adversely. Many different processes show different approaches for the removal of these contaminants. Recently, there is much focus on the use of biopesticides for plant growth, but most botanicals are hydrophobic in nature, and using large amounts of organic pollutants to dissolve them again pollutes the environment. Adsorption is the most widely used process for pesticide removal. The use of chitosan nanocomposite is one such effective process for pesticide removal owing to chitosan's high adsorption capacity due to the open groups present [80].

Rotenone, a colorless, odorless, and isoflavone is a broad-spectrum insecticide. This insecticide is also toxic to fish and humans. The toxicity of rotenone is more significant depending on the particle's size, if the particle is smaller in size higher is the toxicity. Chitosan-graphene oxide nanocomposites exhibited better adsorption through the interactions between the hydrogen bonds of CS-GO nanocomposites and rotenone [7]. Organophosphate pesticides are used worldwide. They are toxic and work by damaging the enzyme system, which controls the nerve signals of the body. Adsorption of organophosphate pesticides with MIL-88(Fe) anchored TiO_2-chitosan (2D/2D) hybrid nanocomposite was achieved, where the reaction was oxidation reaction involved [81]. Methyl parathion, an organophosphate insecticide, can target organ damage on repeated exposure and is much toxic to aquatic life. Effective adsorption of methyl parathion pesticide was carried out using the two-hybrid polymers of bentonite intercalated with chitosan [82]. Organic herbicides are mostly nonselective; they kill fish and plants that come into contact while in a water body. An ionic liquid modified chitosan/metal-organic framework composite was used to adsorb organic herbicides effectively. The adsorption process was found to be facilitated with the help of hydrogen bonding and electrostatic interaction [83]. Tricyclazole, a fungicide is used to protect rice but causes increased organ weight and decreased body weight. Chitosan-based magnetic molecularly imprinted polymer selectively recognizes and adsorbs tricyclazole from the water sample. This polymer was highly selective and specific [84, 85].

9.2. Pharmaceutical Wastes. Water contamination with many pharmaceutical wastes is becoming one of the significant environmental issues caused due to their ecotoxicity accompanied by several health issues. The most commonly present pharmaceuticals in the wastewater are antibiotics, steroids, antidepressants, tranquillizers, analgesics, stimulants, and so on. Among the various removal methods, adsorption is found to be more effective for the removal of these compounds. Recently, chitosan-based nanocomposite is used as an ecofriendly biopolymer that shows effective adsorption of these pharmaceutical materials.

Ofloxacin is an antibiotic present in the wastewater mainly from the hospital wastes and may cause toxicity and affect the biological environment. Therefore, it is essential to remove this ofloxacin with the adsorbent horseradish peroxide immobilized chitosan graphene oxide nanocomposite (HRP-CsGOn). Here, the adsorption kinetics and isotherm model fits the pseudo-second-order and Langmuir model with the maximum adsorption capacity of 378 mg/g [86]. Metronidazole is another antibiotic present in the water which is effectively adsorbed with the help of Fe_3O_4-chitosan nanoadsorbent. Here, the adsorption maximum was 97.06 mg/g with Freundlich isotherm and pseudo-second-order kinetics [87]. Tetracycline is a commonly used antibiotic and is frequently found in the aquatic environment. This could be removed using a magnetic nanocomposite that is fabricated using chitosan, thiobarbituric acid, malondialdehyde, and Fe_3O_4 nanoparticles (CTM@Fe_3O_4). The nanocomposite shows an adsorption maximum of about 215.31 mg/g and the follows kinetic and isotherm are pseudo-second-order kinetic and Langmuir isotherm models [51].

Estradiol, one of the steroid hormones present in the wastewater, could be removed with the help of the chitosan/Al_2O_3-HA (hydroxyapatite) composite beads. The adsorbent shows a maximum adsorption capacity of about 39.78 mg/g which fits into Langmuir and pseudo-second-order kinetics [1]. Diclofenac sodium is a nonsteroidal anti-inflammatory drug which could be adsorbed from the contaminated water with the AmCS@Fe_3O_4 composite (amine-functionalized chitosan (amino chitosan; AmCS) and Fe_3O_4). The corresponding isotherm is Langmuir, and the kinetics is the pseudo-second-order model with the maximum adsorption of 469.48 mg/g [29].

9.2.1. Fluoride. Fluoride ions are essential for the normal functioning of the human body, but exposure to the same beyond the recommended levels results in various health disorders. Excess fluoride can cause structural damage and to ligaments. Removal of fluoride was carried out with different physical and chemical methods earlier [88]. Recently, naturally occurring materials like clay and zeolites combined with biopolymers are used for removing the same. Glauconite clay-functionalized chitosan nanocomposites prepared through simple blending and cross linking method showed effective adsorption of fluoride ions through physisorption process [89]. Chitosan-based magnetic nanocomposites containing Fe_3O_4@TiO_2 nanoparticles also exhibited effective adsorption of fluoride ions from water through the electrostatic and hydrogen bonding interactions [90]. The removal of groundwater fluoride with the help of chitosan-modified ZnO/$ZnFe_2O_4$ nanocomposites showed excellent adsorption properties. The process was spontaneous and endothermic. The morphology and the structural properties of the nanocomposites play a major role in adsorption [91].

9.2.2. Radionuclides. Radionuclides are radioactive atoms and are released from nuclear power plants. The most commonly found radionuclides in water are uranium, radon, and radium. Exposure to this ionizing radiation causes many different forms of cancer such as stomach, lung, and bone. Chitosan nanocomposites for adoring different

Table 3: Different chitosan nanocomposites used to remove oil spills.

Nanocomposite	Contaminant	Kinetics	Isotherm model	Adsorption capacity	References
Chitosan-graphene oxide nanocomposites	Rotenone (pesticide)	Pseudo-first-order	Langmuir	92.59 mg/g	[93]
MIL-88(Fe) anchored TiO_2-chitosan(2D/2D) hybrid nanocomposite	Organophosphate (pesticide)	Pseudo-first-order	Langmuir–Hinshelwood	—	[81]
Chitosan and 2-hydroxyethyl methacrylate/methyl methacrylate-bentonite-based nanocomposite	Methyl parathion (pesticide)	Pseudo-first-order	Freundlich	868.5 mg/g	[82]
Chitosan/metal-organic framework composite	Organic pesticides (pesticide)	Pseudo-second-order	Temkin	—	[83]
Chitosan-based magnetic molecularly imprinted polymer	Tricyclazole (pesticide)	Pseudo-second-order	Freundlich	4579.9 μg/g	[84]
Horseradish peroxidase immobilized onto CsGOn (HRP-CsGOn)	Ofloxacin (antibiotic)	Pseudo-second-order	Langmuir model	378 mg/g	[86]
Fe_3O_4-chitosan nanoadsorbent	Metronidazole (antibiotic)	Pseudo-second-order	Freundlich model	97.06 mg/g	[87]
CTM@Fe_3O_4 nanocomposite	Tetracycline (antibiotic)	Pseudo-second-order	Langmuir model	215.31 mg/g	[51]
chitosan/Al_2O_3-HA composite beads	Estradiol (steroid)	Pseudo-second-order	Langmuir model	39.78 mg/g	[1]
AmCS@Fe_3O_4composite	Diclofenac sodium (nonsteroidal anti-inflammatory drug)	Pseudo-second-order	Langmuir model	469.48 mg/g	[29]
Silica-chitosan nanocomposite	$^{152+154}$Eu (radionuclide)	Pseudo-second-order	Langmuir - Freundlich models	160 mg/g	[92]
Chitosan-acrylic acid-1-vinyl-2-vinylpyrrolidone/ multiwalled carbon nanotubes composite	$^{152+154}$ Eu (radionuclide)	Pseudo-second-order	Langmuir	321.77 mg/g	[94]
Chitosan-acrylic acid-1-vinyl-2-vinylpyrrolidone/ multiwalled carbon nanotubes composite	^{60}Co (radionuclide)	Pseudo-second-order	Langmuir	369.91 mg/g	[94]
Chitosan-acrylic acid-1-vinyl-2-vinylpyrrolidone/ multiwalled carbon nanotubes composite	^{134}Cs (radionuclide)	Pseudo-second-order	Langmuir	456.46 mg/g	[94]
Glauconite clay-functionalized chitosan nanocomposites	Fluoride ions	Pseudo-second-order	Langmuir	9.03 mg/g	[89]
Chitosan-based magnetic nanocomposite containing Fe_3O_4–TiO_2	Fluoride ions	Pseudo-second-order	Langmuir	15.385 mg/g	[90]
Chitosan-modified ZnO/$ZnFe_2O_4$ nanocomposites	Fluoride	Pseudo-first-order	Langmuir	10.54–3.03 mg/g	[91]
Superparamagnetic chitosan nanocomposite	Oil spill	Pseudo-second-order	Langmuir	157.739 mg/g	[95]

radionuclides are used as treatment method these days. A nanocomposite of chitosan-silica is used for the removal of $^{152+154}$Eu radionuclide from water. ^{154}Eu and ^{152}Eu is produced as a fission product and has half-life from 5 to 13 years. This is a main concern for health of living organisms and in humans particularly affects liver and bone cancer. The use of silica-chitosan nanocomposite is low-cost and ecofriendly. The radionuclides were effectively adsorbed and the process is endothermic chemisorption [92]. The use of multiwalled carbon nanotube nanocomposites for removal of radionuclides like $^{152+154}$Eu, ^{60}Co, ^{134}Cs is reported where the nanocomposite shows removal capacity (Table 3) [94].

9.2.3. Microbes. Waterborne diseases are a major concern in many countries and to address this problem, there is an urgent need to devise effective water purification process. As UV radiation is not always suitable, filtration is the next sought-after process. The use of nanoparticles in a polymer matrix is a breakthrough in water treatment process. Chitosan-TiO_2 nanocomposite for effective removal of *E.coli* from water was reported [96, 97]. The bacterial removal was due to the cell membrane damage caused by attaching to the composite. Oxidative stress and ROS are also important aspects that helped removal of *E.coli* [98].

9.2.4. Turbidity. Turbidity of wastewater is one concern during the purification of water. Flocculation is one method which is applied widely to remove the turbidity of water. Flocculants enhances removal of turbidity by flocking the suspended materials together and helps them settle down. Inorganic flocculants were used earlier, and recently, natural polymers are used as flocculants. Nanocomposites are used recently as flocculants. montmorillonite/chitosan/ammonium acrylate composites developed through gamma irradiation showed excellent flocculation activity in river water [58].

9.2.5. Oil Spills. Oil pollution is a universal disaster caused by the spilling of oil during transportation of the petroleum products or from oil and gas industrial discharges. This may cause dreadful effect to the aquatic environment which may leads to ecotoxicity and also loss of life [99]. The polyhydrocarbons present in the oil may cause direct or indirect effect to the aquatic life-forms which includes stunned growth, suffocation, anoxia, and hormonal imbalance. This may also cause trouble in the food chain and web of the marine biota. To overcome this pollution, many technologies such as dispersants, skimmers, and adsorbents are used. Nanotechnology offers the latest method to rectify this problem [100]. For this, a superparamagnetic nanocomposite of Fe_3O_4/chitosan was created using the co-precipitation method. This nanocomposite was utilized for the adsorption of oil from the polluted aquatic environment which follows the kinetics of pseudo-second-order and fits into the Langmuir isotherm model. The maximum adsorption capacity of the nanocomposite in removing the oil spills is found to be 157.739 mg/g [101].

10. Future Perspective

The use of chitosan nanocomposites proves a boon for the removal of different contaminants from water, but all these research studies are in the initial stage. Large-scale implementation still needs to take shape. Different other aspects of using chitosan nanocomposites like membrane filters and as sensors for sensing different contaminants can be looked into. Even though the composites are regarded ecofriendly, not much research had been undergone to evaluate the toxicity of the nanocomposites introduced into the environment. Effective methods for the same need to be devised.

11. Conclusion

Water is an essential component; consequently, improvements in technology are required so that pure drinking water can be supplied to meet the growing demand for it. The utilization of polymeric nanocomposites in water treatment ensures not only the retention of particulate matter but also the removal of contaminants from the water. The presence of nanoparticles guarantees a high surface area, which in turn guarantees a higher level of efficiency in the process. However, the most significant limitation that can occur with polymeric nanomaterials is the implementation of these processes on a large scale, which makes them only rarely adaptable for the treatment process. Recently, the use of biogenic nanomaterials has shown excellent adsorption properties, and these materials are biorenewable in their natural state. When utilizing polymeric nanomaterials for the treatment of water, certain aspects such as toxicity concerns, cost-effectiveness, and the nanomaterials' potential contribution to secondary pollution need to be taken into consideration. The use of polymeric nanocomposites for the treatment of wastewater is a novel approach; consequently, a great number of additional studies need to be carried out in order to compare the performance of these different approaches and to develop improved strategies for locating low-cost, high-selectivity, and recyclable fabricated nanomaterials and nanocatalysts.

Data Availability

The data used to support the findings of this study are not included within the article.

Conflicts of Interest

The authors declare that there are no conflicts of interest regarding the publication of this article.

Acknowledgments

This research was funded by the National Science, Research and Innovation Fund (NSRF) and King Mongkut's University of Technology North Bangkok with Contract no. KMUTNB-FF-66-01.

References

[1] L. Li, J. Iqbal, Y. Zhu et al., "Chitosan/Al2O3-HA nanocomposite beads for efficient removal of estradiol and chrysoidine from aqueous solution," *International Journal of Biological Macromolecules*, vol. 145, pp. 686–693, 2020.

[2] T. K. Zhelev and N. Bhaw, "Combined water-oxygen pinch analysis for better wastewater treatment management," *Waste Management*, vol. 20, no. 8, pp. 665–670, 2000.

[3] Z. Rahman, "An overview on heavy metal resistant microorganisms for simultaneous treatment of multiple chemical pollutants at co-contaminated sites, and their multipurpose application," *Journal of Hazardous Materials*, vol. 396, Article ID 122682, 2020.

[4] H. D. Ponce-Rodríguez, J. Verdú-Andrés, R. Herráez-Hernández, and P. Campíns-Falcó, "Exploring hand-portable nano-liquid chromatography for in place water analysis: determination of trimethylxanthines as a use case," *The Science of the Total Environment*, vol. 747, Article ID 140966, 2020.

[5] P. Westerho and M. Pinney, "Dissolved organic carbon transformations during laboratory-scale groundwater recharge using lagoon-treated wastewater," *Waste Management*, vol. 20, pp. 75–83, 2000.

[6] M. Sivagami, M. Selvambigai, U. Devan et al., "Extraction of microplastics from commonly used sea salts in India and their toxicological evaluation," *Chemosphere*, vol. 263, Article ID 128181, 2021.

[7] M. Sharma, M. Joshi, S. Nigam et al., "Efficient oil removal from wastewater based on polymer coated superhydrophobic tetrapodal magnetic nanocomposite adsorbent," *Applied Materials Today*, vol. 17, pp. 130–141, 2019.

[8] S. Iravani, "Nanomaterials and nanotechnology for water treatment: recent advances," *Inorganic and Nano-Metal Chemistry*, vol. 51, no. 12, pp. 1–31, 2020.

[9] F. Lu and D. Astruc, "Nanocatalysts and other nanomaterials for water remediation from organic pollutants," *Coordination Chemistry Reviews*, vol. 408, Article ID 213180, 2020.

[10] Y. Yang, Y. Li, K. Goh, C. H. Tan, and R. Wang, "Liposomes-assisted fabrication of high performance thin film composite nanofiltration membrane," *Journal of Membrane Science*, vol. 620, Article ID 118833, 2021.

[11] A. Le Duigou, D. Correa, M. Ueda, and M. Castro, "A review of 3D and 4D printing of natural fibre biocomposites," *Materials & Design*, vol. 194, 2020.

[12] S. T. Khan, F. Ahmad, M. Shahadat, W. U. Rehman, and A. M. Khan, "Metal and metal oxide nanoparticles for water decontamination and purification," *Environmental Nanotechnology for Water Purification*, pp. 151–186, 2020.

[13] R. Bhateria and R. Singh, "A review on nanotechnological application of magnetic iron oxides for heavy metal removal," *Journal of Water Process Engineering*, vol. 31, Article ID 100845, 2019.

[14] X. L. Cao, J. Guo, J. Cai et al., "The encouraging improvement of polyamide nanofiltration membrane by cucurbituril-based host–guest chemistry," *AIChE Journal*, vol. 66, no. 4, 2020.

[15] A. Arulrajah, M. M. Disfani, V. Suthagaran, and M. Imteaz, "Select chemical and engineering properties of wastewater biosolids," *Waste Management*, vol. 31, no. 12, pp. 2522–2526, 2011.

[16] D. Gomez-Maldonado, I. B. V. Erramuspe, and M. S. Peresin, "Natural polymers as alternative adsorbents and treatment agents for water remediation," *Bioresources*, vol. 14, no. 4, Article ID 10093, 2019.

[17] D. R. Johnson, M. M. Methner, A. J. Kennedy, and J. A. Steevens, "Potential for occupational exposure to engineered carbon-based nanomaterials in environmental laboratory studies," *Environmental Health Perspectives*, vol. 118, no. 1, pp. 49–54, 2010.

[18] G. Crini, "Historical review on chitin and chitosan biopolymers," *Environmental Chemistry Letters*, vol. 17, no. 4, pp. 1623–1643, 2019.

[19] P. S. Bakshi, D. Selvakumar, K. Kadirvelu, and N. S. Kumar, "Chitosan as an environment friendly biomaterial – a review on recent modifications and applications," *International Journal of Biological Macromolecules*, vol. 150, pp. 1072–1083, 2020.

[20] E. B. Ibitoye, I. H. Lokman, M. N. M. Hezmee, Y. M. Goh, A. B. Z. Zuki, and A. A. Jimoh, "Extraction and physicochemical characterization of chitin and chitosan isolated from house cricket," *Biomedical Materials*, vol. 13, no. 2, Article ID 025009, 2018.

[21] R. Parhi, "Drug delivery applications of chitin and chitosan: a review," *Environmental Chemistry Letters*, vol. 18, no. 3, pp. 577–594, 2020.

[22] C. P. Jiménez-Gómez and J. A. Cecilia, "Chitosan: a natural biopolymer with a wide and varied range of applications," *Molecules*, vol. 25, pp. 3981–4017, 2020.

[23] M. L. Verma, S. Kumar, A. Das, J. S. Randhawa, and M. Chamundeeswari, "Chitin and chitosan-based support materials for enzyme immobilization and biotechnological applications," *Environmental Chemistry Letters*, vol. 18, no. 2, pp. 315–323, 2020.

[24] M. A. Mohammed, J. T. M. Syeda, K. M. Wasan, and E. K. Wasan, "An overview of chitosan nanoparticles and its application in non-parenteral drug delivery," *Pharmaceutics*, vol. 9, no. 4, p. 53, 2017.

[25] K. Ahmed Ahmed, M. Ibrahim mahmoud, and H. Mohammed Mounes, "Effect of using low molecular weight Chitosan on water quality, quality indices and stress reduction of Nile tilapia," *Egyptian Journal for Aquaculture*, vol. 10, no. 2, pp. 47–65, 2020.

[26] N. Reddy and Y. Yang, "Chitosan fibers," *Innovative Biofibers from Renewable Resources*, pp. 99–109, Springer, Heidelberg, Germany, 2015.

[27] K. R. Shoueir, N. El-Desouky, M. M. Rashad, M. K. Ahmed, I. Janowska, and M. El-Kemary, "Chitosan based-nanoparticles and nanocapsules: overview, physicochemical features, applications of a nanofibrous scaffold, and bioprinting," *International Journal of Biological Macromolecules*, vol. 167, pp. 1176–1197, 2021.

[28] H. El Knidri, R. Belaabed, A. Addaou, A. Laajeb, and A. Lahsini, "Extraction, chemical modification and characterization of chitin and chitosan," *International Journal of Biological Macromolecules*, vol. 120, pp. 1181–1189, 2018.

[29] X. X. Liang, A. M. Omer, Z. H. Hu, Y. Wang, D. Yu, and X. K. Ouyang, "Efficient adsorption of diclofenac sodium from aqueous solutions using magnetic amine-functionalized chitosan," *Chemosphere*, vol. 217, pp. 270–278, 2019.

[30] A. Ali and S. Ahmed, "A review on chitosan and its nanocomposites in drug delivery," *International Journal of Biological Macromolecules*, vol. 109, pp. 273–286, 2018.

[31] G. Z. Kyzas, D. N. Bikiaris, and A. C. Mitropoulos, "Chitosan adsorbents for dye removal: a review," *Polymer International*, vol. 66, no. 12, pp. 1800–1811, 2017.

[32] S. Kumar, F. Ye, S. Dobretsov, and J. Dutta, "Chitosan nanocomposite coatings for food, paints, and water treatment applications," *Applied Sciences*, vol. 9, pp. 2409–2412, 2019.

[33] X. Gong, W. Tian, J. Bai, K. Qiao, J. Zhao, and L. Wang, "Highly efficient deproteinization with an ammonifying bacteria Lysinibacillus fusiformis isolated from brewery spent diatomite," *Journal of Bioscience and Bioengineering*, vol. 127, no. 3, pp. 326–332, 2019.

[34] T. C. Yadav, P. Saxena, A. K. Srivastava et al., "Potential applications of chitosan nanocomposites: recent trends and challenges," *Advanced Functional Textiles and Polymers*, pp. 365–403, 2019.

[35] M. Ali, M. Shakeel, and K. Mehmood, "Extraction and characterization of high purity chitosan by rapid and simple techniques from mud crabs taken from Abbottabad," *Pakistan journal of pharmaceutical sciences*, vol. 32, no. 1, pp. 171–175, 2019.

[36] S. Kumari, S. H. Kumar Annamareddy, S. Abanti, and P. Kumar Rath, "Physicochemical properties and characterization of chitosan synthesized from fish scales, crab and shrimp shells," *International Journal of Biological Macromolecules*, vol. 104, pp. 1697–1705, 2017.

[37] J. Chakravarty, C. L. Yang, J. Palmer, and C. J. Brigham, "Chitin extraction from lobster shell waste using microbial culture-based methods," *Appl. Food Biotechnol.*vol. 5, no. 3, pp. 141–154, 2018.

[38] M. N. Marzieh, F. Zahra, E. Tahereh, and K. N. Sara, "Comparison of the physicochemical and structural characteristics of enzymatic produced chitin and commercial chitin," *International Journal of Biological Macromolecules*, vol. 139, pp. 270–276, 2019.

[39] J. Zamora-Sillero, A. Gharsallaoui, and C. Prentice, "Peptides from fish by-product protein hydrolysates and its functional properties: an overview," *Marine Biotechnology*, vol. 20, no. 2, pp. 118–130, 2018.

[40] S. Abirami and D. Nagarajan, "Extraction of chitin from shrimp shell wastes by using Bacillus licheniformis and Lactobacillus plantarum," *International Journal of Recent Research Aspects*, vol. 12, pp. 307–315, 2018.

[41] T. Philibert, B. H. Lee, and N. Fabien, "Current status and new perspectives on chitin and chitosan as functional biopolymers," *Applied Biochemistry and Biotechnology*, vol. 181, no. 4, pp. 1314–1337, 2017.

[42] P. F. P. Barbosa, L. R. Cumba, R. D. A. Andrade, and D. R. do Carmo, "Chemical modifications of cyclodextrin and chitosan for biological and environmental applications: metals and organic pollutants adsorption and removal," *Journal of Polymers and the Environment*, vol. 27, no. 6, pp. 1352–1366, 2019.

[43] I. Bano, M. Arshad, T. Yasin, M. A. Ghauri, and M. Younus, "Chitosan: a potential biopolymer for wound management," *International Journal of Biological Macromolecules*, vol. 102, pp. 380–383, 2017.

[44] S. Xia, L. Zhang, A. Davletshin, Z. Li, J. You, and S. Tan, "Application of polysaccharide biopolymer in petroleum recovery," *Polymers*, vol. 12, no. 9, pp. 1860–1936, 2020.

[45] M. O. Abd El-Magied, A. A. Galhoum, A. A. Atia et al., "Cellulose and chitosan derivatives for enhanced sorption of erbium(III)," *Colloids and Surfaces A: Physicochemical and Engineering Aspects*, vol. 529, no. Iii, pp. 580–593, 2017.

[46] F. Luan, L. Wei, J. Zhang et al., "Preparation and characterization of quaternized chitosan derivatives and assessment of their antioxidant activity," *Molecules*, vol. 23, no. 3, p. 516, 2018.

[47] S. Pokhrel and P. N. Yadav, "Functionalization of chitosan polymer and their applications," *Journal of Macromolecular Science, Part A*, vol. 56, no. 5, pp. 450–475, 2019.

[48] C. Ryan, E. Alcock, F. Buttimer et al., "Synthesis and characterisation of cross-linked chitosan composites functionalised with silver and gold nanoparticles for antimicrobial applications," *Science and Technology of Advanced Materials*, vol. 18, no. 1, pp. 528–540, 2017.

[49] H. Tanaka, C. Azuma, K. Sanui, and N. Ogata, "Synthesis of photosensitive polymers from chitosan," *Polymer Journal*, vol. 12, no. 1, pp. 63–66, 1980.

[50] A. Pistone, D. Iannazzo, C. Celesti et al., "Chitosan/PAMAM/Hydroxyapatite engineered drug release hydrogels with tunable rheological properties," *Polymers*, vol. 12, pp. 754–4, 2020.

[51] T. Ahamad, M. Naushad, T. Al-Shahrani, N. Al-hokbany, and S. M. Alshehri, "Preparation of chitosan based magnetic nanocomposite for tetracycline adsorption: kinetic and thermodynamic studies," *International Journal of Biological Macromolecules*, vol. 147, pp. 258–267, 2020.

[52] M. E. Abd El-Hack, M. T. El-Saadony, M. E. Shafi et al., "Antimicrobial and antioxidant properties of chitosan and its derivatives and their applications: a review," *International Journal of Biological Macromolecules*, vol. 164, pp. 2726–2744, 2020.

[53] B. D. Malhotra and M. A. Ali, "Nanocomposite materials," *Nanomaterials for Biosensors*, pp. 145–159, Trans Tech Publications Limited, Stafa-Zurich, Switzerland, 2nd edition, 2018.

[54] M. A. Aizat and F. Aziz, *12-Chitosan Nanocomposite Application in Wastewater Treatments*, Elsevier Inc, Amsterdam, Netherlands, 2018.

[55] A. Maalouf and M. El-Fadel, "Effect of a food waste disposer policy on solid waste and wastewater management with economic implications of environmental externalities," *Waste Management*, vol. 69, pp. 455–462, 2017.

[56] B. C. Cerri, L. M. Borelli, I. M. Stelutti, M. R. Soares, and M. A. da Silva, "Evaluation of new environmental friendly particulate soil fertilizers based on agroindustry wastes biopolymers and sugarcane vinasse," *Waste Management*, vol. 108, pp. 144–153, 2020.

[57] Y. Ding, T. A. Kuhlbusch, M. Van Tongeren et al., "Airborne engineered nanomaterials in the workplace—a review of release and worker exposure during nanomaterial production and handling processes," *Journal of Hazardous Materials*, vol. 322, pp. 17–28, 2017.

[58] O. A. Ghazy, S. A. Khalil, and M. M. Senna, "Synthesis of montmorillonite/chitosan/ammonium acrylate composite and its potential application in river water flocculation," *International Journal of Biological Macromolecules*, vol. 163, pp. 1529–1537, 2020.

[59] D. Hu, Z. Lian, H. Xian et al., "Adsorption of Pb(II) from aqueous solution by polyacrylic acid grafted magnetic chitosan nanocomposite," *International Journal of Biological Macromolecules*, vol. 154, pp. 1537–1547, 2020.

[60] V. P. Dinh, M. D. Nguyen, Q. H. Nguyen et al., "Chitosan-MnO2 nanocomposite for effective removal of Cr (VI) from aqueous solution," *Chemosphere*, vol. 257, Article ID 127147, 2020.

[61] T. E. Khalil, A. F. Elhusseiny, A. El-dissouky, and N. M. Ibrahim, "Functionalized chitosan nanocomposites for

removal of toxic Cr (VI) from aqueous solution," *Reactive and Functional Polymers*, vol. 146, Article ID 104407, 2020.

[62] M. E. Mahmoud, G. M. Nabil, and S. M. T. Elweshahy, "Novel NTiO2-chitosan@NZrO2-chitosan nanocomposite for effective adsorptive uptake of trivalent gadolinium and samarium ions from water," *Powder Technology*, vol. 378, pp. 246–254, 2021.

[63] X. Wang, X. Liu, C. Xiao et al., "Triethylenetetramine-modified hollow Fe3O4/SiO2/chitosan magnetic nanocomposites for removal of Cr(VI) ions with high adsorption capacity and rapid rate," *Microporous and Mesoporous Materials*, vol. 297, Article ID 110041, 2020.

[64] M. Rajamani and K. Rajendrakumar, "Chitosan-boehmite desiccant composite as a promising adsorbent towards heavy metal removal," *Journal of Environmental Management*, vol. 244, pp. 257–264, 2019.

[65] J. Wang, R. Ma, L. Li, P. Gu, and X. Wang, "Chitosan modified molybdenum disulfide composites as adsorbents for the simultaneous removal of U(VI), Eu(III), and Cr(VI) from aqueous solutions," *Cellulose*, vol. 27, no. 3, pp. 1635–1648, 2020.

[66] I. M. M. Kenawy, M. M. Eldefrawy, R. M. Eltabey, and E. G. Zaki, "Melamine grafted chitosan-montmorillonite nanocomposite for ferric ions adsorption: central composite design optimization study," *Journal of Cleaner Production*, vol. 241, Article ID 118189, 2019.

[67] W. Wang, C. Xue, and X. Mao, "Chitosan: structural modification, biological activity and application," *International Journal of Biological Macromolecules*, vol. 164, pp. 4532–4546, 2020.

[68] G. De Gioannis, L. F. Diaz, A. Muntoni, and A. Pisanu, "Two-phase anaerobic digestion within a solid waste/wastewater integrated management system," *Waste Management*, vol. 28, no. 10, pp. 1801–1808, 2008.

[69] S. K. Lakkaboyana, K. Soontarapa, Vinaykumar, R. K. Marella, and K. Kannan, "Preparation of novel chitosan polymeric nanocomposite as an efficient material for the removal of Acid Blue 25 from aqueous environment," *International Journal of Biological Macromolecules*, vol. 168, pp. 760–768, 2021.

[70] Z. Abootorabi, M. R. Sohrabi, and S. Mortazavinik, "Removing diazo direct red 81 using chitosan/zero-valent iron nanocomposite from aqueous solutions and process Optimization," *International Journal of Environmental Analytical Chemistry*, vol. 103, no. 5, pp. 1168–1185, 2021.

[71] N. T. Nguyen, N. T. Nguyen, and V. A. Nguyen, "In situ synthesis and characterization of ZnO/chitosan nanocomposite as an adsorbent for removal of Congo red from aqueous solution," *Advances in Polymer Technology*, vol. 2020, Article ID 3892694, 8 pages, 2020.

[72] A. H. Jawad, N. S. A. Mubarak, and A. S. Abdulhameed, "Hybrid crosslinked chitosan-epichlorohydrin/TiO2 nanocomposite for reactive red 120 dye adsorption: kinetic, isotherm, thermodynamic, and mechanism study," *Journal of Polymers and the Environment*, vol. 28, no. 2, pp. 624–637, 2020.

[73] V. M. Muinde, J. M. Onyari, B. Wamalwa, and J. N. Wabomba, "Adsorption of malachite green dye from aqueous solutions using mesoporous chitosan–zinc oxide composite material," *Environmental Chemistry and Ecotoxicology*, vol. 2, pp. 115–125, 2020.

[74] M. I. Mohammed, M. K. Ismael, and M. Gönen, "Synthesis of chitosan-silica nanocomposite for removal of methyl orange from water: composite characterization and adsorption performance," *IOP Conference Series: Materials Science and Engineering*, vol. 745, no. 1, Article ID 012084, 2020.

[75] H. Hassan, A. Salama, A. K. El-ziaty, and M. El-sakhawy, "New chitosan/silica/zinc oxide nanocomposite as adsorbent for dye removal," *International Journal of Biological Macromolecules*, vol. 131, pp. 520–526, 2019.

[76] M. A. Ahmed, N. M. Abdelbar, and A. A. Mohamed, "Molecular imprinted chitosan-TiO2 nanocomposite for the selective removal of Rose Bengal from wastewater," *International Journal of Biological Macromolecules*, vol. 107, pp. 1046–1053, 2018.

[77] A. Reghioua, D. Barkat, A. H. Jawad, A. S. Abdulhameed, A. A. Al-Kahtani, and Z. A. Alothman, "Parametric optimization by Box-Behnken design for synthesis of magnetic chitosan-benzil/ZnO/Fe3O4nanocomposite and textile dye removal," *Journal of Environmental Chemical Engineering*, vol. 9, no. 3, Article ID 105166, 2021.

[78] M. Abbasi, "Synthesis and characterization of magnetic nanocomposite of chitosan/SiO2/carbon nanotubes and its application for dyes removal," *Journal of Cleaner Production*, vol. 145, pp. 105–113, 2017.

[79] R. M. de Souza, D. Seibert, H. B. Quesada, F. de Jesus Bassetti, M. R. Fagundes-Klen, and R. Bergamasco, "Occurrence, impacts and general aspects of pesticides in surface water: a review," *Process Safety and Environmental Protection*, vol. 135, pp. 22–37, 2020.

[80] M. Nadporozhskaya, N. Kovsh, R. Paolesse, and L. Lvova, "Recent advances in chemical sensors for soil analysis: a review," *Chemosensors*, vol. 10, no. 1, p. 35, 2022.

[81] S. Vigneshwaran, P. Sirajudheen, P. Karthikeyan, M. Nikitha, K. Ramkumar, and S. Meenakshi, "Immobilization of MIL-88(Fe) anchored TiO2-chitosan(2D/2D) hybrid nanocomposite for the degradation of organophosphate pesticide: characterization, mechanism and degradation intermediates," *Journal of Hazardous Materials*, vol. 406, Article ID 124728, 2021.

[82] M. R. Abukhadra, A. M. El-Sherbeeny, M. A. El-Meligy, and M. Luqman, "Insight into carbohydrate polymers (chitosan and 2- hydroxyethyl methacrylate/methyl methacrylate) intercalated bentonite-based nanocomposites as multifunctional and environmental adsorbents for methyl parathion pesticide," *International Journal of Biological Macromolecules*, vol. 167, pp. 335–344, 2021.

[83] X. Huang, S. Feng, G. Zhu et al., "Removal of organic herbicides from aqueous solution by ionic liquid modified chitosan/metal-organic framework composite," *International Journal of Biological Macromolecules*, vol. 149, pp. 882–892, 2020.

[84] N. Laskar, D. Ghoshal, and S. Gupta, "Chitosan-based magnetic molecularly imprinted polymer: synthesis and application in selective recognition of tricyclazole from rice and water samples," *Iranian Polymer Journal (English Edition)*, vol. 30, no. 2, pp. 121–134, 2021.

[85] Z. Zhao, L. Xu, Y. Wang, B. Li, W. Zhang, and X. Li, "Toxicity mechanism of silver nanoparticles to Chlamydomonas reinhardtii: photosynthesis, oxidative stress, membrane permeability, and ultrastructure analysis," *Environmental Science & Pollution Research*, vol. 28, no. 12, Article ID 15032, 2021.

[86] A. Suri, V. Khandegar, and P. J. Kaur, "Ofloxacin exclusion using novel HRP immobilized chitosan cross-link with graphene-oxide nanocomposite," *Groundwater for Sustainable Development*, vol. 12, Article ID 100515, 2021.

[87] E. Asgari, A. Sheikhmohammadi, and J. Yeganeh, "Application of the Fe3O4-chitosan nano-adsorbent for the adsorption of metronidazole from wastewater: optimization, kinetic, thermodynamic and equilibrium studies," *International Journal of Biological Macromolecules*, vol. 164, pp. 694–706, 2020.

[88] M. C. Lavagnolo, F. Girotto, O. Hirata, and R. Cossu, "Lab-scale co-digestion of kitchen waste and brown water for a preliminary performance evaluation of a decentralized waste and wastewater management," *Waste Management*, vol. 66, pp. 155–160, 2017.

[89] M. M. Sobeih, M. F. El-Shahat, A. Osman, M. A. Zaid, and M. Y. Nassar, "Glauconite clay-functionalized chitosan nanocomposites for efficient adsorptive removal of fluoride ions from polluted aqueous solutions," *RSC Advances*, vol. 10, no. 43, Article ID 25567, 2020.

[90] A. Abri, M. Tajbakhsh, and A. Sadeghi, "Adsorption of fluoride on a chitosan-based magnetic nanocomposite: equilibrium and kinetics studies," *Water Supply*, vol. 19, no. 1, pp. 40–51, 2019.

[91] G. K. Sarma, R. Sharma, R. Saikia et al., "Facile synthesis of chitosan-modified ZnO/ZnFe2O4 nanocomposites for effective remediation of groundwater fluoride," *Environmental Science & Pollution Research*, vol. 27, no. 24, Article ID 30067, 2020.

[92] G. A. Dakroury, S. F. Abo-Zahra, H. S. Hassan, and N. A. Fathy, "Utilization of silica–chitosan nanocomposite for removal of152+154Eu radionuclide from aqueous solutions," *Journal of Radioanalytical and Nuclear Chemistry*, vol. 323, no. 1, pp. 439–455, 2020.

[93] M. S. Muda, A. Kamari, S. A. Bakar et al., "Chitosan-graphene oxide nanocomposites as water-solubilising agents for rotenone pesticide," *Journal of Molecular Liquids*, vol. 318, Article ID 114066, 2020.

[94] I. M. Abdelmonem, E. Metwally, T. E. Siyam, F. Abou El-Nour, and A. R. M. Mousa, "Gamma radiation-induced preparation of chitosan-acrylic acid-1-vinyl-2-vinylpyrrolidone/multiwalled carbon nanotubes composite for removal of 152+154Eu, 60Co and 134Cs radionuclides," *International Journal of Biological Macromolecules*, vol. 164, pp. 2258–2266, 2020.

[95] H. Singh, A. Jain, J. Kaur, S. K. Arya, and M. Khatri, "Adsorptive removal of oil from water using SPIONs–chitosan nanocomposite: kinetics and process optimization," *Applied Nanoscience*, vol. 10, no. 4, pp. 1281–1295, 2020.

[96] V. D. Rajput, T. Minkina, A. Kumari et al., "A review on nanobioremediation approaches for restoration of contaminated soil," *Eurasian J. Soil Sci.*vol. 11, no. 1, pp. 43–60, 2022.

[97] C. Jiang and Q. Chen, "Effect of long-term low concentrations of TiO2 nanoparticles on dewaterability of activated sludge and the relevant mechanism: the role of nanoparticle aging," *Environmental Science & Pollution Research*, vol. 29, no. 8, Article ID 12188, 2022.

[98] Z. Xu, G. Huang, C. An et al., "Low-cost microbiological purification using a new ceramic disk filter functionalized by chitosan/TiO2 nanocomposites," *Separation and Purification Technology*, vol. 248, Article ID 116984, 2020.

[99] F. Di Maria and F. Sisani, "A sustainability assessment for use on land or wastewater treatment of the digestate from biowaste," *Waste Management*, vol. 87, pp. 741–750, 2019.

[100] N. Kumar and H. Raheman, "Thermal and environmental performance of CI engine using CeO2 nanoparticles as additive in water–diesel–biodiesel fuel blend," *International journal of Environmental Science and Technology*, vol. 19, no. 4, pp. 3287–3304, 2022.

[101] A. Singh, S. Chaudhary, and B. S. Dehiya, "Fast removal of heavy metals from water and soil samples using magnetic Fe3O4 nanoparticles," *Environmental Science & Pollution Research*, vol. 28, no. 4, pp. 3942–3952, 2021.

Hindawi
Advances in Materials Science and Engineering
Volume 2023, Article ID 3085478, 11 pages
https://doi.org/10.1155/2023/3085478

Research Article

Investigation on the Mechanical Properties of Powder Metallurgy-Manufactured AA7178/$ZrSiO_4$ Nanocomposites

R. Srinivasan,[1] S. Karunakaran,[2] M. Hariprabhu,[3] R. Arunbharathi,[4] S. Suresh,[5] S. Nanthakumar,[6] S. K. H. Ahammad,[7] S. Mayakannan,[8] and Mani Jayakumar[9]

[1]*Sri Krishna College of Technology, Coimbatore, Tamilnadu, India*
[2]*Department of Chemical Engineering, KPR Institute of Engineering and Technology, Coimbatore, Tamilnadu, India*
[3]*Department of Electrical and Electronics Engineering, M. Kumarasamy College of Engineering, Karur, Tamilnadu, India*
[4]*Department of Mechanical Engineering, Sri Krishna College of Engineering and Technology, Coimbatore, Tamilnadu, India*
[5]*Department of Chemistry, St. Martin's Engineering College, Secunderabad, Telangana, India*
[6]*Department of Mechanical Engineering, PSG Institute of Technology and Applied Research Neelambur, Coimbatore, Tamilnadu, India*
[7]*Department of Electronics and Communication Engineering, Koneru Lakshmaiah Education Foundation, Vijayawada 522302, India*
[8]*Department of Mechanical Engineering, Vidyaa Vikas College of Engineering and Technology, Tiruchengode, Namakkal, Tamilnadu, India*
[9]*Department of Chemical Engineering, Haramaya Institute of Technology, Haramaya University, P.B. No. 138, Dire Dawa, Ethiopia*

Correspondence should be addressed to Mani Jayakumar; drjayakumarmani@haramaya.edu.et

Received 13 January 2023; Revised 7 April 2023; Accepted 4 May 2023; Published 22 May 2023

Academic Editor: V. Vijayan

The versatility of metal matrix composites (MMCs) makes them a promising material for various industrial applications. The current study used a ball milling to mechanically AA7178 powder and strengthened with zirconium silicate ($ZrSiO_4$) nanoparticles. In addition, the AA7178 matrix was ball-milled to distribute the $ZrSiO_4$ nanoparticles throughout the material. The AA7178 reinforced with $ZrSiO_4$ nanoparticles was compacted and consolidated using two distinct powder metallurgy (PM) sequences: double pressing, double sintering, and hot pressing. In tests measuring microhardness, compression strength, and elongational break, the new nanocomposites surpassed the AA7178. The adequate interfacial bonding and even distribution of $ZrSiO_4$ nanoparticles throughout the AA7178 matrix were essential to the strengthening mechanism. With the use of hot pressing, the mechanical characteristics of the nanocomposites were enhanced. As reinforcement concentration increased beyond 2.5% by weight, mechanical properties drastically degraded due to $ZrSiO_4$ nanoparticles clumping and unequal distribution. Improved mechanical parts attain through the uniform distribution of $ZrSiO_4$ nanoparticles in the AA7178 and the maintenance of their mechanical properties.

1. Introduction

Due to naturally enhanced mechanical capabilities and exceptional weight, $ZrSiO_4$ nanoparticles have been the focus of research and development in the scientific and industrial communities over the past decade [1]. Applications in transportation and security, where the combination of lighter materials with improved mechanical qualities is desirable, show great promise for the use of $ZrSiO_4$ nanoparticles as reinforcing material for the fabrication of MMC [2]. Close connections developed between the matrix and the scattered $ZrSiO_4$ nanoparticles, which helped to fine-tune the grain and boost the mechanical characteristics of the materials. The mechanisms of grain refining, load transfer,

and Orowan looping provide the basis of the reinforcement contributions [3, 4]. $ZrSiO_4$ nanoparticles are often researched as reinforcing materials due to their higher efficiency and simplicity of manufacture. However, $ZrSiO_4$ nanoparticles offer better mechanical characteristics (from 60 to 160 GPa) and high elastic modulus (1.9 TPa) [5].

The latest review by the authors [6] indicates that several studies discuss using powder methods to reinforce aluminum or aluminum alloys. However, effective nanoaluminum alloy composites with state-of-the-art properties continue to be hampered by various obstacles brought on by the features of $ZrSiO_4$ nanoparticles [7]. The most urgent issues to be addressed include clustering, minimal wettability of $ZrSiO_4$ nanoparticles with aluminum, and the development of numerous distinct phases at 450°C, such as aluminum carbide (Al_4C_3) or aluminum oxides [8–10]. Aluminum-$ZrSiO_4$ nanoparticles interfacial bond strength, $ZrSiO_4$ aspect ratio, and nano $ZrSiO_4$ quality all play a vital role in the mechanical characteristics of $ZrSiO_4$-reinforced aluminum alloys [11–13].

Many different chemical pretreatments have been applied to the $ZrSiO_4$ nanoparticles, and conditions have been used in the $ZrSiO_4$ nanoparticle powder combination (like nanoparticles or graphite) to enhance the original shape and surface qualities of metal powders [14, 15]. Ball milling is frequently used, but because of the lengthy milling process substantial damage to $ZrSiO_4$ nanoparticles, the Nano $ZrSiO_4$/Al composite's mechanical characteristics are typically subpar [16, 17]. Composite aluminum alloy reinforced with $ZrSiO_4$ nanoparticles can be made using a wide variety of powder consolidation techniques, such as cold pressing, hot pressing, hot extrusion, and spark plasma sintering (SPS) [18].

The research reports the fabrication of AA7075-based hybrid composites using TiO_2 and fly ash as reinforcements via stir casting and hot forging. The mechanical behavior of the composites was studied through compression tests, showing increased compressive strength with higher weight fractions of TiO_2. The coefficient of thermal expansion decreased with the addition of TiO_2 and fly ash, while a slight decrease in thermal conductivity was observed compared to AA7075 [19].

The study reports on the development of A357 alloy composite reinforced with dual size SiC particles by stir casting. Different weight fractions of dual size SiC particles were investigated for their influence on mechanical properties and wear resistance of A357 composites. The composites showed improvement in hardness, yield, and tensile strength compared to A357 alloy, with 4 wt. % of fine and 2 wt. % of large SiC particles displaying the highest tensile strength and 4 wt. % of large and 2 wt. % of fine SiC particles exhibiting high hardness and wear resistance [20].

Aluminum alloy composites with graphene nanoplates were produced by ball milling and stir casting. The addition of graphene nanoplates reduced grain size and increased the strength of the composites. T6 heat treatment improved the strength of the composites, but at higher graphene content, agglomerates on grain boundaries facilitated crack growth [21].

Aluminum hybrid composites were produced using powder metallurgy with varying weight fractions of graphene and fixed CNT content. Wear tests were conducted with varying applied load, and worn surface analysis was done using SEM. Increasing graphene content increased bulk hardness and reduced wear rate due to the formation of a lubricating layer [22]. Aluminum hybrid composites were developed using powder metallurgy technique with Si_3N_4 and CNT as reinforcements. Scanning electron microscope studies showed uniform dispersion of both reinforcements. Microhardness increased with CNT content, electrical conductivity decreased, and coefficient of friction decreased due to the lubricating nature of CNTs [22, 23].

This research successfully produced AA7178 reinforced with $ZrSiO_4$ nanoparticles using milling, mechanical alloying, and two distinct compaction and sintering processes. The proposed manufacturing processes use commercial technologies that could enable mass production of high-value AA7178/$ZrSiO_4$ nanocomposites for use in demanding lightweight constructions, including armored assault vehicles. The goal was to minimize structural failure of the $ZrSiO_4$ nanoparticles while achieving a homogeneous dispersion of the nanoparticles in the metal matrix using powder technology approaches that could eventually lead to commercial mass production. Al7075 nanocomposites with varying B4C contents were produced using powder metallurgy technique. Microstructure, grain size, and wear behavior were analyzed. Dry sliding wear test was conducted using Taguchi L9 approach, and the most influential parameter on wear volume was found to be the B4C nanoparticle content.

2. Methods and Materials

The AA7178 created through mechanical alloying, and its nominal composition is 2% copper, 2.7% magnesium, 6.8% zinc, and aluminum balance. The Sigma/Aldrich firm obtained all the materials mentioned previously. The AA7178 mix matrix was created in a high-energy, vertically agitated ball mill for three hours at 500 revolutions per minute to avoid oxidation during production. Powder agglomeration was avoided by adding a small amount of ethanol to the mixture. Stearic acid was added to the mix at a 1 wt. % to ensure uniformity throughout the manufacturing process [24, 25]. The researcher used a 10 : 1 ball-to-powder ratio in our mechanical alloying technique involving stainless-steel balls.

Ball milling was also employed to create the nanocomposite material. The previously milled AA7178 powder was combined with various amounts of $ZrSiO_4$ nanoparticles (1.5, 2.5, 3.5, 4.5, 5.5, and 6.5 wt. %) in a planetary ball mill with the same milling conditions. To avoid damaging the $ZrSiO_4$ nanoparticles, the milling speed was reduced to 250 rpm, and the milling time was extended to 60 minutes.

"A stainless-steel cylinder mold with an internal radius of 9 mm was used to perform uniaxial compression on milled powder combinations of AA7178 and $ZrSiO_4$ nanoparticles. Graphene oxide was used as an additive to

reduce the effects of friction. Hot-pressing (HP) and double pressing and sintering techniques (DPST) were used for compaction. The powder used to create the AA7178 for this investigation is shown in Figure 1(a)."

After being heated and compacted under 250 MPa of pressure for 10 minutes at a specific temperature of 400°C, the milled composite powder mixes were presintered in a low vacuum furnace for 60 minutes at 520°C. Green compacts were lightly sprayed with a graphite spray to reduce resistance to the mold before being pressed for a second time. After 10 minutes at 400°C and 550 MPa, the second hot compaction was completed. After preheating to 590°C, the green compacts were sintered for 120 minutes in a low vacuum.

For the HP process, hot pressing was done for 60 minutes at 400 MPa under 550°C on mixtures of milled composite powders. The green compacts were heated to 590°C for 120 minutes in a low vacuum environment. Milled AA7178 were hot-pressed, and sintered AA7178 were both processed for this study.

Both sintered composite samples and milled composite powders have their crystal structures evaluated using X-ray diffraction (XRD). During this sintering process, a TA Instruments DSC 25 differential scanning calorimeter was used to determine the phase transition from RT to 600°C at 15°C/min. Microstructural characterization and phase distribution in sintered composite samples were assessed using SEM [26, 27].

Sintered composite samples were subjected to mechanical testing on a Vickers microhardness analyzer with a 100 g load and a dwell time of 20 seconds [28]. At least five readings were averaged to arrive at the final microhardness value using a strain rate of 0.01 s^{-1}, which is common for materials with lower modulus. The researcher performed quasistatic compression tests, with each sample tested three times to achieve repeatable and dependable results. The compressive stress-strain characteristics were determined by averaging the data from the three tests. The dimensions of the samples used for ASTM E9 solid compressive testing were calculated. Small samples are commonly used for compressive testing since compliant metals, which are often used as thin plates to transmit vertical load to the surfaces, are typically employed [29]. In the compression test, each sample was 20 mm long and 16 mm in diameter ($L/D = 1.25$). Scanning electron microscopy (SEM) was employed to analyze the fractured surfaces of specimen pieces taken from the crushed materials [30, 31].

3. Results and Discussions

3.1. Sintered Composite and Milled Composite Structural Property. The flake-shaped morphology of the AA7178 powder created after the ball-milling process is considered favorable for incorporating $ZrSiO_4$ nanoparticles into the matrix [32, 33]. Ball-milled AA7178/$ZrSiO_4$ nanoparticles powder mixtures are shown in SEM. There were no $ZrSiO_4$ nanoparticle aggregates to be seen, indicating that they had been evenly distributed and integrated into the AA7178 powders. Although most of the $ZrSiO_4$ nanoparticles look fragmented and smaller than the original ones, their estimated length is still sufficient, demonstrating that ball milling did not cause damage.

Figure 2 shows the X-Ray Diffraction pattern for the milled AA7178, and the milled AA7178-$ZrSiO_4$ nanocomposites. The $ZrSiO_4$ nanoparticles peak at $2\theta = 34°$, identical to the graphite *C* height, is readily observed [34–36]. The peak's exceptional sharpness indicates that the two-dimensional Graphene layer providing the tubular pattern of the zirconia has nearly perfect crystallinity. A further indicator of the $ZrSiO_4$ nanoparticles' excellent purity is that the *C* curve was not filtered toward the highest values of 2θ (greater than 34°). At $2\theta = 46°$, also known as the graphite peak, and at $2\theta = 78°$, also known as the graphite peak, are peaks of noticeably lesser intensity [37, 38]. These peaks are not crisp. Hence the crystallinity of the different $ZrSiO_4$ nanoparticles can differ. The enlargement of this peak may indicate that other graphitized carbon types are present [39–41].

Both milled AA7178 samples show aluminum diffraction peaks. There are also a few peaks that are associated with copper and magnesium. Magnesium peaks vanish after 2 hours of $ZrSiO_4$ nanoparticles milling on the AA7178, leaving only copper peaks to be seen. Both the intensity and the width of these peaks are waning. This outcome implies that mechanical alloying was used successfully to produce AA7178. Once the $ZrSiO_4$ nanoparticles are fine-tuned, the remaining *C* peaks vanish, suggesting that few of the *C* content has been liquefied into the aluminum to generate a solid state. For the AA7178-2.5 wt. % after milling, a differential scanning calorimeter was performed. This assumption was tested by a process involving 100% $ZrSiO_4$ nanoparticles.

In Figure 3, the DSC curve is displayed. This low-temperature first peak is associated with the evaporation and subsequent release of humidity from ethanol. A small exothermic peak between 410 and 440°C was observed for the AA7178-$ZrSiO_4$ nanoparticles powder mixture. Al_4C_3 formation may be related to this peak. During sintering, the metastable Al-C solid solution breaks down, forming Al_4C_3 [42].

In contrast, the XRD patterns of milled AA7178-$ZrSiO_4$ nanoparticles did not show any broadening of the aluminum peaks compared to milled AA7178. This shows that aluminum's structure has not absorbed significant carbon material. The aluminum's lattice parameter and crystallite size remained constant throughout all examined situations, indicating that the metal contains negligible amounts of carbon [43, 44]. Milled and sintered AA7178-$ZrSiO_4$ nanoparticle samples exhibited XRD structures devoid of pronounced Al_4C_3 peaks. This confirms that the $ZrSiO_4$ nanoparticles utilized in this analysis are steady when interacting with aluminum and do not break into aluminum carbide [45]. The XRD results show that the $ZrSiO_4$ nanoparticles are the most excellent possible quality and contain no silicon oxide or imperfections in the carbon [46].

Specimens of milled and sintered AA7178-$ZrSiO_4$ nanoparticles, manufactured using the HP process, with (a) 4.5% and (b) 2.5% $ZrSiO_4$ nanoparticles compositions, are

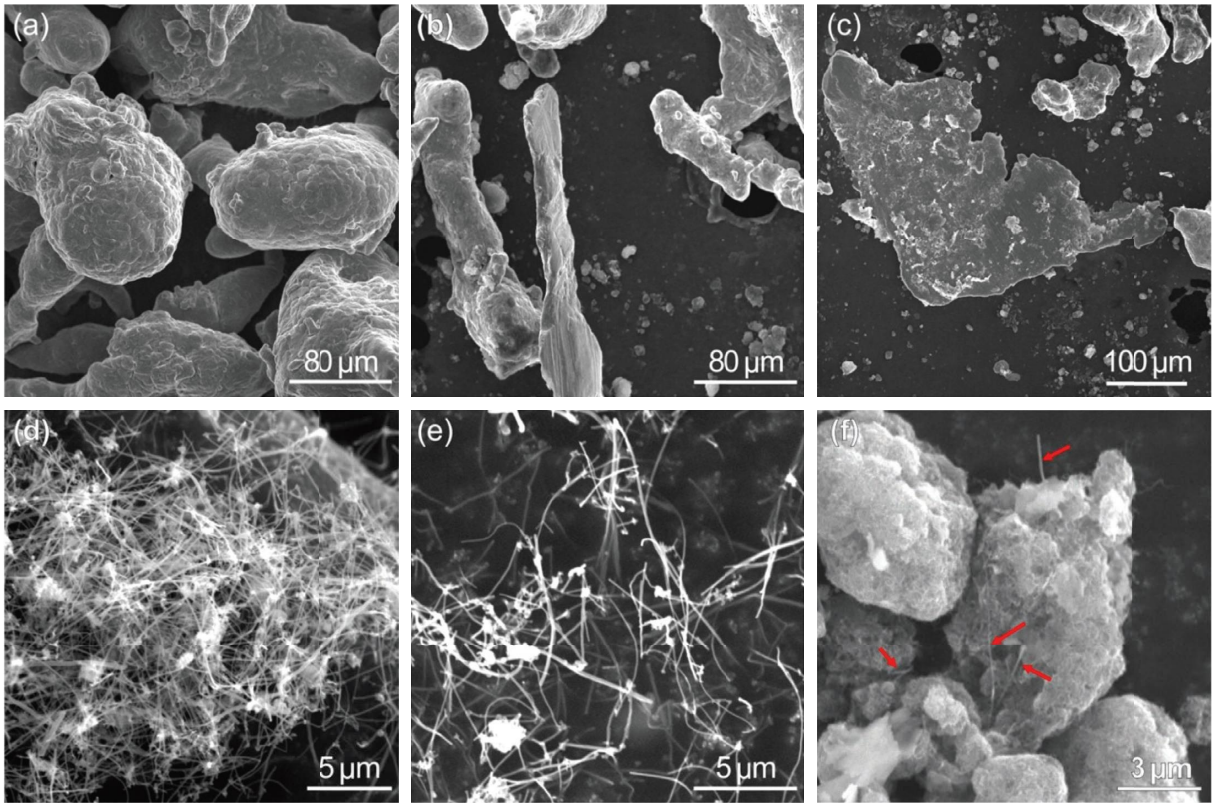

Figure 1: Scanning electron microscopic image of (a) initial AA7178 utilized, (b and c) AA7178 next to ball milling, (d and e) $ZrSiO_4$ nanoparticles utilized, (f) AA7178 and $ZrSiO_4$ nanoparticles next to ball milling.

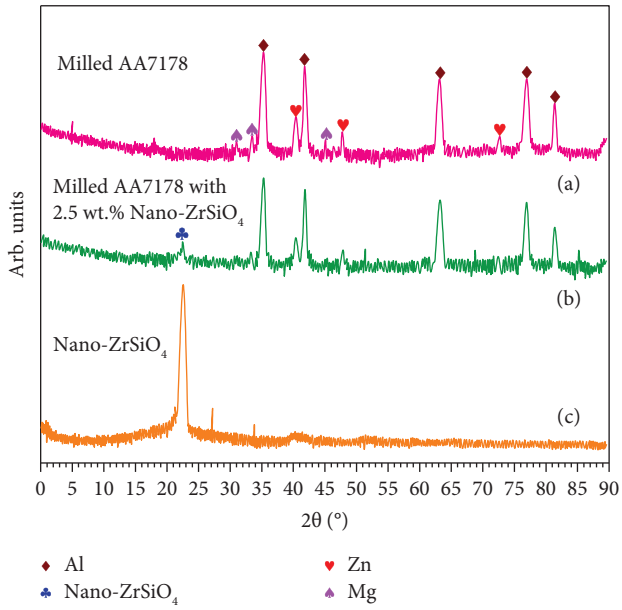

Figure 2: X-ray diffraction pattern of (a) AA7178, (b) 2.5% $ZrSiO_4$ nanoparticles powder mixtures, and (c) AA7178 reinforced with $ZrSiO_4$ nanoparticles.

shown as XRD patterns in Figure 4. Sintered AA7178 in its purest form is displayed in Figure 4(c). While sintering eliminated the oxide peak, the intermetallic phase Al_2O was still present in all sintered specimens (AA7178 and the composite), regardless of the $ZrSiO_4$ nanoparticles amount. The microstructure progression of intermetallic stages in

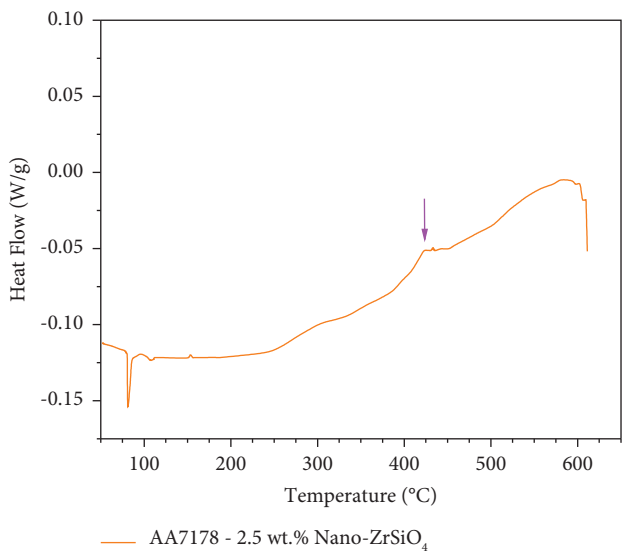

Figure 3: DSC curvature for the composite AA7178-2.5 wt. % $ZrSiO_4$ nanoparticles specimen.

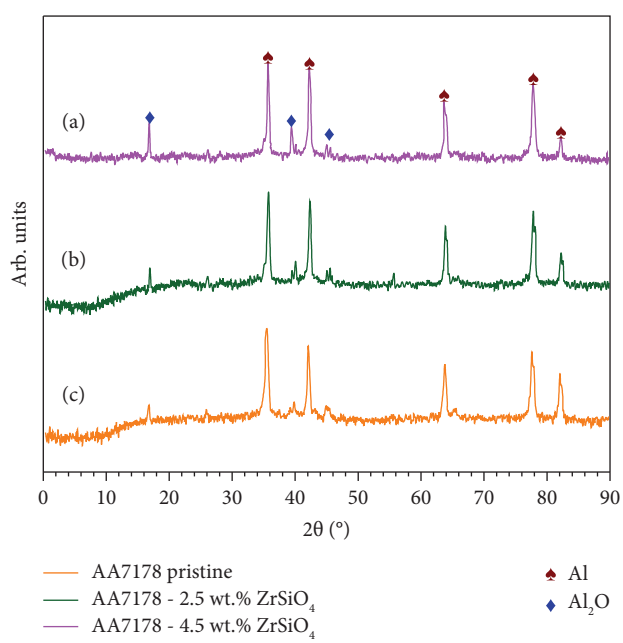

Figure 4: X-ray diffraction pattern of sintered and milled (a) AA7178-4.5 wt. % $ZrSiO_4$ nanoparticles and (b) AA7178-2.5 wt. % $ZrSiO_4$ nanoparticles (HP technique) and the (c) pristine AA7178.

AA7178 is significantly influenced by zirconia, as evidenced by the considerable changes in the intensity of these peaks with increasing $ZrSiO_4$ nanoparticles content.

Each composite material XRD pattern lacked the characteristic $ZrSiO_4$ nanoparticles *C* peak (Figures 4(a) and 4(b)). Due to low concentration of $ZrSiO_4$ nanoparticles on the surface of the specimen under analysis and the small scattering distance among carbon and metal atoms.

Microstructures of the AA7178-2.5% $ZrSiO_4$ nanoparticles composite produced by the two compaction techniques are shown in Figure 5. Both approaches consolidate the metal particles well. All methods can identify the intermetallic Al_2O phase, which can be easily identified by the lines and is found in both the grain borders and the interior regions of the grains. HP techniques appear to favor the formation of Al_2O intermetallic phases in the nanocomposite's microstructure. The DPSD compaction method preserves the flake shape of the initial AA7178 powders. HP causes grain strengthening.

Furthermore, the nanocomposite made using HP techniques exhibits subgrains. For instance, a few subgrains are indicated by red-dashed lines. This result provided support for the hypothesis that the hot-pressing technique led to grain strengthening via two distinct methodologies: (i) demolition of the flake morphologies of the ball-milling utilized, resulting in particle size drop of the first grains generated by the AA7178 and (ii) formation of the particle within these grains. This dynamic recovery and recrystallization cause high levels of plastic strain and heat, which are stamps of HP.

In contrast, the first grains for AA7178 powders are only revealed using the DPDS technique. Given the high oxygen content, these regions seem to belong to Al_2O. These oxides developed in the open air at the hot compaction phase of both production processes. The metallographic processing of this sample likely caused any porosity in this oxide by fracturing such brittle stages, leading to the formation of pores [47]. The argon atmosphere employed in the DPDS process causes varied shapes of the oxides. When HP is given to Al-$ZrSiO_4$ nanoparticles composites in a neutral atmosphere, the amorphous Al_2O_3 transforms into coarse, lump-shaped crystalline Al_2O_3 at matrix grain boundaries. The AA7178 grains must contain the oxide due to the high oxygen content. Additionally, due to the reaction of $ZrSiO_4$ nanoparticles with aluminum to generate brittle aluminum carbides, the oxide is present in the AA7178 grains [48].

3.2. Mechanical Properties. Figure 6(a) depicts the stress-strain relationship under compression for DPDS-created AA7178 nanocomposites with various $ZrSiO_4$ nanoparticles. Adding $ZrSiO_4$ nanoparticles, even at a low concentration of 2.5% by weight, enhances the nanocomposite's mechanical characteristics. Figures 6(a) and 6(b) indicate that for the 4.5% $ZrSiO_4$ nanoparticles with AA7178 nanocomposite, the results improve with increasing $ZrSiO_4$ nanoparticles content. Below the percentage mentioned above, mechanical properties begin to deteriorate noticeably. The observed findings explain the weak interface bonding among the AA7178 and the $ZrSiO_4$ nanoparticles, caused by the silicon oxide clustering and unequal distribution in the AA7178 matrix.

$ZrSiO_4$ nanoparticles have been shown to play an essential role in the compression behavior and modulus of AA7178 nanocomposites. When the concentration of $ZrSiO_4$ nanoparticles in AA7178 is increased, it causes a significant increase in the yield stress, indicating that the

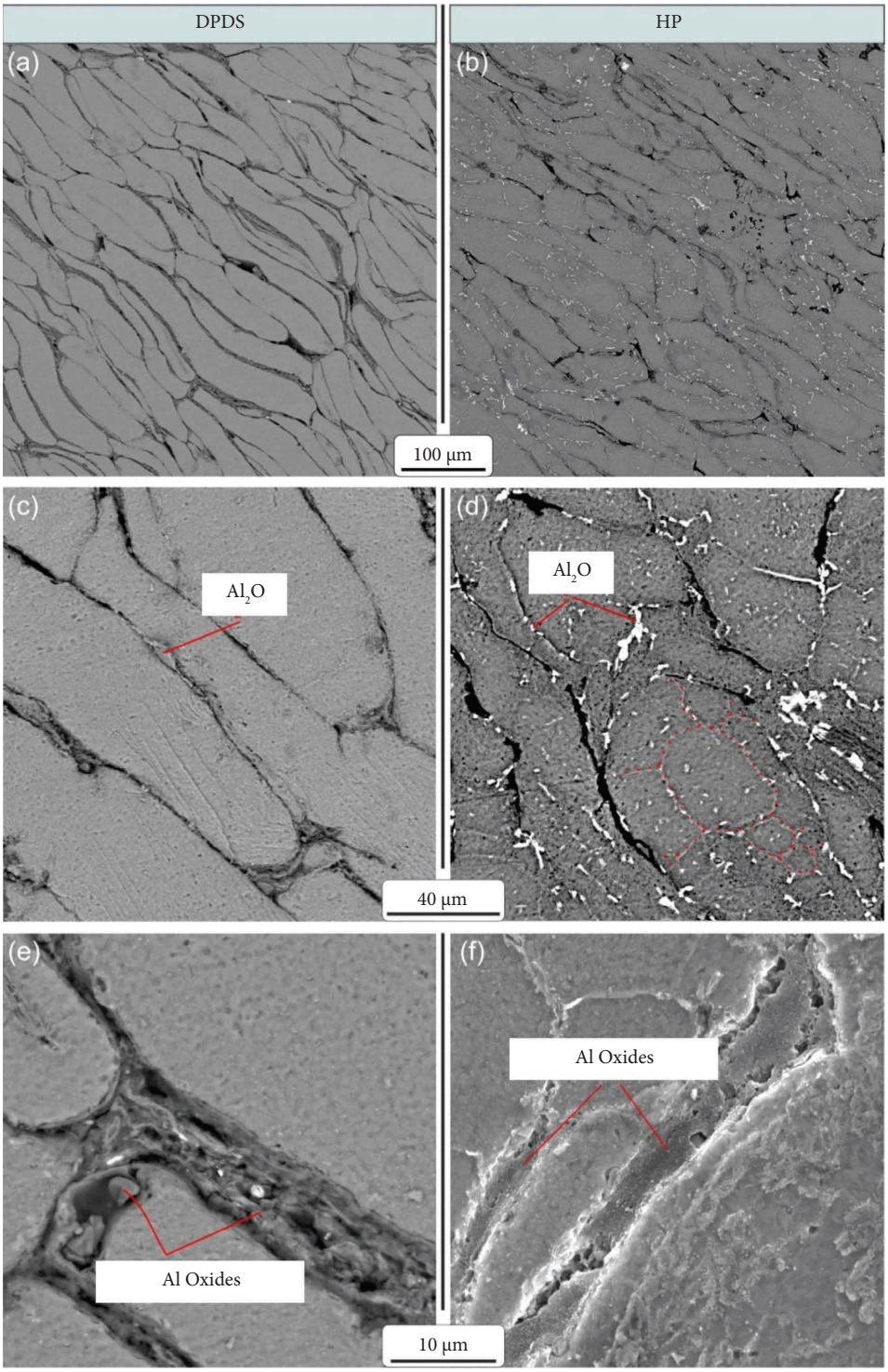

Figure 5: Microstructure of AA7178-2.5 weight. % $ZrSiO_4$ nanoparticles generated via double pressing double sintering (a, c, e), hot pressing (b, d, f).

nanoparticles strengthen the composite. This is because the nanoparticles create barriers to dislocation motion, which causes an increase in the yield stress. In addition, the $ZrSiO_4$ nanoparticles also contribute to the increased modulus of the composite. This is because the nanoparticles are stiffer than the aluminum matrix, and their incorporation into the composite results in a stiffer overall structure. The increased modulus also means that the composite is more resistant to deformation.

However, as the concentration of $ZrSiO_4$ nanoparticles is further increased to 2.5%, the compression behavior of the composite starts to deteriorate. This is because the nanoparticles become clustered, resulting in the formation of large clusters that can cause cracks in the composite. The

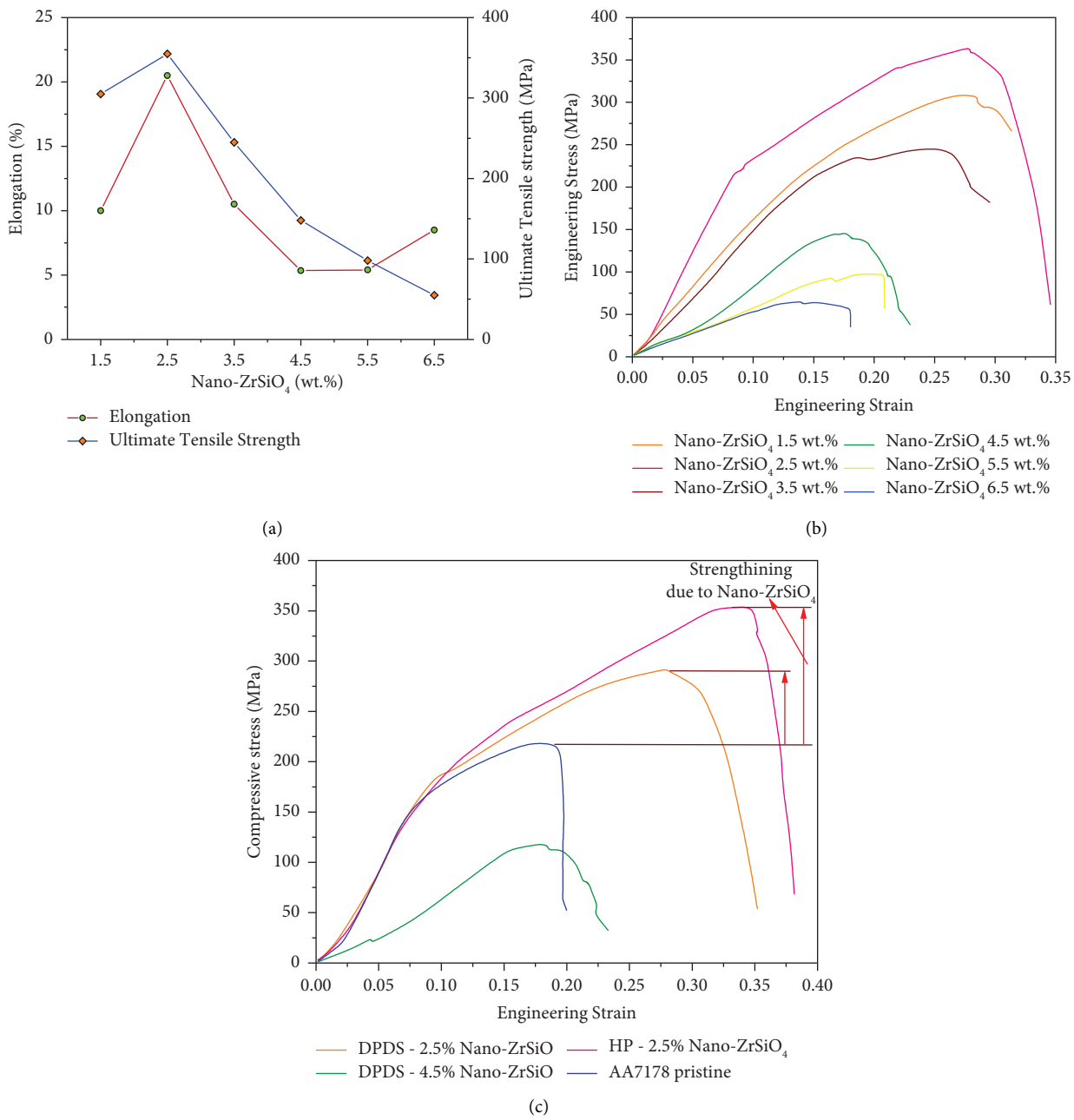

Figure 6: (a) Ultimate tensile strength and elongation values. (b) Compressive stress-strain curvature with various reinforcement of $ZrSiO_4$ nanoparticles with DPDS technique and (c) compressive stress-strain curvature of the AA7178 at various reinforcement with different PM techniques.

cracks act as stress concentrators and reduce the strength of the composite, leading to a decrease in the yield stress and modulus. Therefore, the concentration of nanoparticles should be carefully controlled to achieve the optimal balance between strength and toughness.

Figure 6(b) displays stress and strain curvature and representative images of tested samples for AA7178 and numerous AA7178-$ZrSiO_4$ nanocomposites made under varying conditions. For comparison, the researcher also provides flawless AA7178 (Figure 6(b)). The AA7178-2.5% $ZrSiO_4$ nanoparticles composite produced by the DPDS or HP techniques has ultimate strength and considerably higher yield than pure AA7178. Fracture elongation was also greatly improved from 0.13 for AA7178 to 0.19 for the double pressing double sintering technique and 0.21 for the hot-pressing approach. The improved flexibility of the AA7178 matrix can be accredited to the uniform dispersal of $ZrSiO_4$ nanoparticles throughout the matrix [49].

Young's modulus and other mechanical parameters of the nanocomposite are improved more by the HP compaction method than by the DPDS approach. The matrix material has been refined, leading to a denser composite.

Table 1: Comparison of microhardness for various conditions.

Constituents	Pristine AA7178	Double pressing double sintering		Hot pressing 2.5 wt. % $ZrSiO_4$ nanoparticles
		2.5 wt. % $ZrSiO_4$ nanoparticles	4.5 wt. % $ZrSiO_4$ nanoparticles	
Microhardness $HV_{0.1}$	58	64	51	72

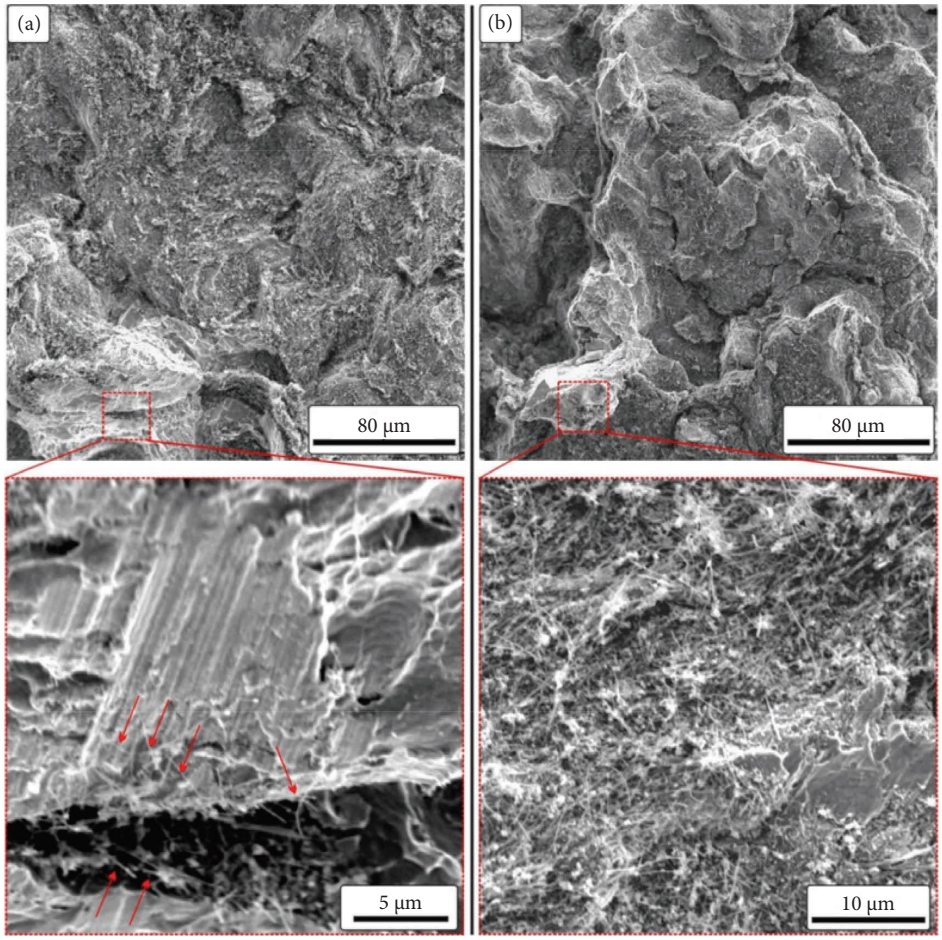

Figure 7: Scanning electron microscope of fracture surfaces: (a) AA7178-2.5% $ZrSiO_4$ nanoparticles and (b) AA7178-4.5% $ZrSiO_4$ nanoparticles generated through DPDS technique.

Compared to the HP method, which yielded composites with a density of 2.65 g/cm^3 (equal to 98%), the DPDS method yielded composites with a thickness of 2.6 g/cm^3 (equivalent to 93.5% of the theoretical value). When comparing AA7178-2.5 wt. % $ZrSiO_4$ nanoparticles produced by DPDS and HP, the strength-ductility effectiveness (compressive strength × elongation) was calculated to be 5.25 GPa for DPDS and 8.17 GPa for HP, showing that the balance among highest strength and elasticity was effectively attained in the case of HP.

The AA7178 matrix and $ZrSiO_4$ nanoparticles may strengthen the resultant nanocomposites through various mechanisms, including grain boundary reinforcement, grain strengthening, stress transfer from AA7178 to $ZrSiO_4$ nanoparticles, and Orowan looping. $ZrSiO_4$ nanoparticles alone reveal essential reinforcing when the aluminum grains are more significant than the strengthening, and the ZrSiO4 nanoparticles are predominantly positioned on the grain restrictions, as is the case here.

Utilizing the increased mechanical properties of the nanotubes requires a successful load transfer from the AA7178 matrix to the $ZrSiO_4$ nanoparticles. Mechanical parameters correlate highly with $ZrSiO_4$-AA7178 interfacial bonding, $ZrSiO_4$ nanoparticles structural integrity, and uniform nanotube dispersion in the metal matrix. Reinforcement of the composites may also result from a favorable mechanism, the contact of dislocations with the nanotubes. A fractographic study of compressed samples was carried out to verify the load transmission.

The mechanical compressive testing findings demonstrate that the composites made with AA7178-2.5 wt. % $ZrSiO_4$ nanoparticles are more complex than pure AA7178.

This is supported by the composite materials' microhardness ratings (Table 1). The AA7178-4.5 wt. % $ZrSiO_4$ nanoparticles nanocomposite is much less mechanically robust, as evidenced by microhardness measurements. The samples passed microhardness testing with flying colors, demonstrating efficient load transmission because of the lack of cracking.

Figure 7 shows the SEM images of the cracked surfaces of AA7178-$ZrSiO_4$ nanocomposites with 2.5 wt. % and 4.5 wt. % $ZrSiO_4$ nanoparticles content, respectively. Load transmission efficiency at the $ZrSiO_4$/matrix contact was demonstrated by $ZrSiO_4$ nanoparticle pull-outs (arrows) on the AA7178 fracture surface. The pull-outs evident during tensile testing provide insight into the load transferring at the $ZrSiO_4$ nanoparticles/matrix interaction and the disposition of $ZrSiO_4$ nanoparticles during the fracturing behavior of the sample. Some places were subjected to shear and tension, even if the overall application of stress was just compressive. Extensive pull-outs indicate a strong connection between the matrix and the $ZrSiO_4$ nanoparticles, enhancing strengthening effects. These exceptionally long pull-outs prove that the silicon oxide was not significantly reduced in length during milling. It is important to note that the distribution of pull-out $ZrSiO_4$ nanoparticles in the broken surfaces of the samples under study was correlated with their existence.

Cracks in an AA7178-4.5 wt. % $ZrSiO_4$ nanoparticles nanocomposite reveal clusters of $ZrSiO_4$ nanoparticles and inhomogeneous distribution in the matrix (Figure 7(b)). Poor mechanical qualities result from aggregate formation, which weakens the interfacial bond among the $ZrSiO_4$ nanoparticles and AA7178 composites. According to the results of other researchers [50, 51], the percentage of $ZrSiO_4$ nanoparticles employed in the reinforcement can be used to estimate the maximum content of the integrated reinforcement, with a lower portion resulting in more distribution of $ZrSiO_4$ nanoparticles in the matrix.

4. Conclusions

An AA7178 composite reinforcing with $ZrSiO_4$ nanoparticles was successfully created employing a mechanical alloy process and milling process, succeeded by two compacting and sintering processes. The produced nanocomposites' mechanical characteristics and corresponding microstructural morphologies were investigated and correlated. Insights like these can be gleaned from the data:

(1) Both compaction methods led to the development of a composite material with improved mechanical properties when compared to pure AA7178 alloy. However, the high-pressure (HP) method resulted in a composite with denser microstructure and smaller grain size, which led to even better mechanical properties. Despite experiencing significant splintering, the structural integration of the $ZrSiO_4$ nanoparticles remained intact. It is likely that the fracturing facilitated the efficient transmission of loads from the aluminum matrix to the $ZrSiO_4$ nanoparticles.

(2) The study demonstrated a direct correlation between the mechanical strength of the composite and the amount of $ZrSiO_4$ nanoparticles added to the matrix, up to a certain point. However, adding more than 2.5 wt. % $ZrSiO_4$ nanoparticles caused a significant reduction in the mechanical properties of the composite due to the clustering of the nanoparticles.

(3) The AA7178-2.5wt. % $ZrSiO_4$ nanocomposite, when produced using the DPDS method, exhibited a compressive strength of 372 MPa, while the same nanocomposite manufactured through the HP approach displayed a higher strength of 445 MPa. However, both methods resulted in the development of nanocomposites with sufficient strength-ductility efficiency, as evidenced by their elongation values of 19% and 21%, respectively.

Data Availability

The data supporting the current study are available from the corresponding author upon request.

Conflicts of Interest

The authors declare that they have no conflicts of interest.

Acknowledgments

The authors would like to sincerely thank those techniques that have contributed to this research.

References

[1] F. Gillani, M. Z. Khan, and O. R. Shah, "Sensitivity analysis of reinforced aluminum based metal matrix composites," *Materials*, vol. 15, pp. 4225–4312, 2022.

[2] H. Abdizadeh, M. Ashuri, P. T. Moghadam, A. Nouribahadory, and H. R. Baharvandi, "Improvement in physical and mechanical properties of aluminum/zircon composites fabricated by powder metallurgy method," *Materials & Design*, vol. 32, no. 8–9, pp. 4417–4423, 2011.

[3] N. Bharat and P. S. C. Bose, "Optimization of tribological behaviour of TiO2nanoparticles reinforced AA7178 alloy matrix using ANN and Taguchi's methodology," *Surface Topography: Metrology and Properties*, vol. 10, no. 2, Article ID 025032, 2022.

[4] T. A. Amibo, S. M. Beyan, M. Mustefa, V. P. Sundramurthy, and A. B. Bayu, "Development of nanocomposite based antimicrobial cotton fabrics impregnated by nano SiO2 loaded AgNPs derived from eragrostis teff straw," *Materials Research Innovations*, vol. 26, no. 7, pp. 405–414, 2021.

[5] R. Saravanan, C. Gnanavel, S. Rajesh, T. Kamatchi, S. Ajith Arul Daniel, and D. K. Nagarathi, "Synthesis of Zinc oxide and CNT in AA7178 aluminium alloy composite impression on characteristics," *Materials Today: Proceedings*, vol. 62, pp. 1973–1976, 2022.

[6] J. R. Xavier, "Improvement of mechanical and anticorrosion coating properties in conducting polymer poly(propyl methacrylate) embedded with silane functionalized silica nanoparticles," *Silicon*, vol. 13, no. 10, pp. 3291–3305, 2021.

[7] A. H. S. Shatha, M. Rajaa Abduljabbar, A. N. Abood, and H. A. Abdulhadi, "Evaluation the effect of shot peening time

on static torsional strength of AA7178-T6," *Journal of Engineering and Applied Sciences*, vol. 13, no. 12, pp. 4476–4481, 2018.

[8] M. Banerjee, T. N. Verma, and P. Nashine, "Experimental and numerical analysis of extrusion process for AA 7178 alloy with varying process parameters," *Materials Today: Proceedings*, vol. 5, no. 2, pp. 6839–6847, 2018.

[9] C. Vidal, V. Infante, and P. Vilaça, "Metallographic characterization of friction stir channels," *Materials Science Forum*, vol. 730, pp. 817–822, 2012.

[10] C. Vidal, V. Infante, and P. Vilaça, "Mechanical characterization of friction stir channels under internal pressure and in-plane bending," *Key Engineering Materials*, vol. 488, pp. 105–108, 2011.

[11] V. Mohanavel and M. Ravichandran, "Optimization of parameters to improve the properties of AA7178/Si3N4 composites employing Taguchi approach," *Silicon*, vol. 14, no. 4, pp. 1381–1394, 2022.

[12] P. Chattoraj, P. Prabhakar, V. Koti et al., S. P. Kumar, Optimization on tribological behaviour of aa7178/nano titanium diboride hybrid composites employing Taguchi techniques," *Journal of Nanomaterials*, vol. 2022, Article ID 1619923, 8 pages, 2022.

[13] S. D. Kumar, M. Ravichandran, A. Jeevika, B. Stalin, C. Kailasanathan, and A. Karthick, "Effect of ZrB2 on microstructural, mechanical and corrosion behaviour of aluminium (AA7178) alloy matrix composite prepared by the stir casting route," *Ceramics International*, vol. 47, no. 9, pp. 12951–12962, 2021.

[14] G. S. V. S. Kumar, A. Kumar, S. Rajesh, R. B. R. Chekuri, and V. P. Sundaramurthy, "Experimental and thermal investigation with optimization on friction stir welding of nylon 6A using Taguchi and microstructural analysis," *Advances in Mechanical Engineering*, vol. 13, no. 10, Article ID 168781402110507, 2021.

[15] V. Mohanavel, K. Yoganandam, V. N. Kumar, A. Chandrashekar, and S. Prasath, "Evaluation of tribological behaviour of AA7178/Gr composites using Taguchi optimization technique," *Materials Today: Proceedings*, vol. 33, pp. 4691–4695, 2020.

[16] V. Mohanavel, "Mechanical and microstructural characterization of AA7178-TiB2 composites," *Materials Testing*, vol. 62, no. 2, pp. 146–150, 2020.

[17] S. D. Kumar, M. Ravichandran, and 'Synthesis, "Synthesis, characterization and Wire electric erosion behaviour of AA7178-10 wt.% ZrB2 composite," *Silicon*, vol. 10, no. 6, pp. 2653–2662, 2018.

[18] S. D. Kumar and M. Ravichandran, "Synthesis, properties and EDM behavior of 10 wt.-% ZrB2 reinforced AA7178 matrix composites," *Materials Testing*, vol. 60, no. 9, pp. 877–884, 2018.

[19] K. Shivananda Murthy, D. P. Girish, R. Keshavamurthy, T. Varol, and P. G. Koppad, "Mechanical and thermal properties of AA7075/TiO2/Fly ash hybrid composites obtained by hot forging," *Progress in Natural Science: Materials International*, vol. 27, no. 4, pp. 474–481, 2017.

[20] A. Lakshmikanthan, S. Bontha, M. Krishna, P. G. Koppad, and T. Ramprabhu, "Microstructure, mechanical and wear properties of the A357 composites reinforced with dual sized SiC particles," *Journal of Alloys and Compounds*, vol. 786, pp. 570–580, 2019.

[21] G. A. Kumar, J. Satheesh, K. V Murthy, H. M. Mallikarjuna, N. Puneeth, and P. G. Koppad, "Optimization of Wear Properties of B4C Nanoparticle-Reinforced Al7075 Nanocomposites Using Taguchi Approach," *Journal of The Institution of Engineers (India): Series D*, vol. 104, pp. 1–12, 2022.

[22] M. Alipour, R. Keshavamurthy, P. G. Koppad, A. Shakiba, and N. C. Reddy, "Investigation of microstructure and mechanical properties of cast Al–10Zn–3.5 Mg–2.5 Cu nanocomposite reinforced with graphene nano sheets produced by ultrasonic assisted stir casting," *International Journal of Metalcasting*, vol. 17, no. 2, pp. 935–946, 2022.

[23] M. H. R. Naik, L. H. Manjunath, V. Koti, A. Lakshmikanthan, P. G. Koppad, and S. P. Kumaran, "Al/Graphene/CNT hybrid composites: hardness and sliding wear studies," *FME Transactions*, vol. 49, no. 2, pp. 414–421, 2021.

[24] K. Shanmuganandam, S. Thanikaikarasan, T. Ahamad, S. Ali, and V. P. Sundramurthy, "Structure, surface nature, thermal stability, and biomass gasification process of NiO/SiO2 and NiO-Pr2O3/SiO2 nanocomposites obtained through facile deposition precipitation method," *Journal of Nanomaterials*, vol. 2022, Article ID 1479808, 9 pages, 2022.

[25] D. R. Belichko, T. E. Konstantinova, G. K. Volkova et al., E. Popov, Effects of YSZ ceramics doping with silica and alumina on its structure and properties," *Materials Chemistry and Physics*, vol. 287, Article ID 126237, 2022.

[26] A. P. Pasupulla, P. Amornphimoltham, T. T. Halabo, H. Abebe, and M. M. Ramakrishna, "Microstructure and characterization of Al 6082 alloy with addition of ZrSiO4and TiC reinforcements," *AIP Conference Proceedings*, vol. 2473, 2022.

[27] L. Wang, B. Ma, X. Ren et al., Z. Jiang, Phase-engineering strategy of ZrO2 for enhancing the mechanical properties of porous cordierite ceramics," *Materials Today Communications*, vol. 30, Article ID 103032, 2022.

[28] H. Zhang, "Preparation of porous ceramic building decoration materials by foaming method and research on nanomechanical properties," *International Journal of Analytical Chemistry*, vol. 2022, Article ID 8339503, 7 pages, 2022.

[29] C. G. Soubelet and M. P. Albano, "Differences in microstructure and mechanical properties between Y-TZP and AL2O3-doped Y-TZP/bioglass ceramics," *International Journal of Applied Ceramic Technology*, vol. 18, no. 6, pp. 2237–2249, 2021.

[30] M. A. Violini, M. F. Hernández, M. Gauna, G. Suarez, M. S. Conconi, and N. M. Rendtorff, "Low (and negative) thermal expansion Al2TiO5 materials and Al2TiO5 - 3Al2O3.2SiO2 - zrTiO4 composite materials. Processing, initial zircon proportion effect, and properties," *Ceramics International*, vol. 44, no. 17, pp. 21470–21477, 2018.

[31] M. T. Souza, G. M. Peñarrieta-Juanito, B. Henriques, F. S. Silva, A. P. Novaes de Oliveira, and J. C. M. Souza, "Lithium-zirconium silicate glass-ceramics for restorative dentistry: physicochemical analysis and biological response in contact with human osteoblast," *Materialia*, vol. 2, pp. 37–45, 2018.

[32] M. F. Zawrah, R. S. Farag, and M. H. Kohail, "Improvement of physical and mechanical properties of geopolymer through addition of zircon," *Materials Chemistry and Physics*, vol. 217, pp. 90–97, 2018.

[33] V. Ramesha, T. B. Prasad, V. Nayak, and V. L. Neelakantha, "A study on mechanical properties of Al-17Si metal matrix composites," *IOP Conference Series: Materials Science and Engineering*, vol. 376, Article ID 012100, 2018.

[34] N. Liao, D. Jia, Z. Yang, Y. Zhou, and Y. Li, "Enhanced mechanical properties, thermal shock resistance and oxidation resistance of Si2BC3N ceramics with Zr-Al addition,"

Materials Science and Engineering: A, vol. 725, pp. 364–374, 2018.

[35] P. Li, "Tribological properties and microstructures of Al2O3-TiC-TiB2 reinforced composites," *Science and Engineering of Composite Materials*, vol. 24, no. 5, pp. 715–720, 2017.

[36] M. Sharifitabar, M. Kashefi, and S. Khorshahian, "Effect of friction stir processing pass sequence on properties of Mg-ZrSiO4-Al2O3 surface hybrid micro/nano-composites," *Materials & Design*, vol. 108, pp. 1–7, 2016.

[37] N. M. Rendtorff, S. Gómez, M. R. Gauna, M. S. Conconi, G. Suarez, and E. F. Aglietti, "Dense mullite-zirconia-zirconium titanate ceramic composites by reaction sintering," *Ceramics International*, vol. 42, no. 1, pp. 1563–1572, 2016.

[38] T. S. Kumar, R. Subramanian, S. Shalini, and P. C. Angelo, "Microstructure, mechanical properties and corrosion behaviour of Al–Si–Mg alloy matrix/zircon and alumina hybrid composite," *Forschung im Ingenieurwesen*, vol. 79, no. 3–4, pp. 123–130, 2015.

[39] S. K. Thandalam, S. Ramanathan, and S. Sundarrajan, "Synthesis, microstructural and mechanical properties of ex situ zircon particles (ZrSiO4) reinforced Metal Matrix Composites (MMCs): a review," *Journal of Materials Research and Technology*, vol. 4, no. 3, pp. 333–347, 2015.

[40] M. Feng, C. Jiang, M. Chen, S. Zhu, and F. Wang, "A general strategy towards improving the strength and thermal shock resistance of glass-ceramics through microstructure regulation," *Journal of Materials Science & Technology*, vol. 120, pp. 139–149, 2022.

[41] F. Stergioudi, A. Prospathopoulos, A. Farazas, E. C. Tsirogiannis, and N. Michailidis, "Mechanical properties of AA2024 aluminum/MWCNTs nanocomposites produced using different powder metallurgy methods," *Metals*, vol. 12, pp. 1315–1318, 2022.

[42] F. Lin, F. Jia, M. Ren et al., "Microstructure, mechanical and thermal properties of ultrafine-grained Al2024–TiC-GNPs nanocomposite," *Materials Science and Engineering: A*, vol. 841, Article ID 142855, 2022.

[43] P. Ashwath, M. A. Xavior, R. Rajendran, A. D. L. Batako, P. Jeyapandiarajan, and J. Joel, "Microwave-assisted T6 heat treating of aluminium alloy-Al2O3 nanocomposites," *MRS Communications*, vol. 12, no. 2, pp. 245–249, 2022.

[44] S. Rokkala, V. K. Ambati, D. K. Mellam, R. Nethala, and B. V. S. A. Kumar, "Predicting impact strength and hardness of aluminium & tungsten carbide nano-composite synthesized by PM," *Materials Today: Proceedings*, vol. 67, pp. 342–350, 2022.

[45] Y. Sun, A. Li, Y. Hu, X. Wang, and M. Liu, "Simultaneously enhanced strength-plasticity of graphene/metal nanocomposites via interfacial microstructure regulation," *International Journal of Plasticity*, vol. 148, Article ID 103143, 2022.

[46] V. Shrivastava, G. Kumar Gupta, H. Jain, D. Mangal, P. Singh, and I. B. Singh, "Novel synthesis approach of making efficient nanocomposite via powder metallurgy route: study of microstructure and mechanical properties," *Manufacturing Letters*, vol. 31, pp. 36–39, 2022.

[47] M. Çelebi, O. Güler, A. Çanakçı, and H. Çuvalcı, "The effect of nanoparticle content on the microstructure and mechanical properties of ZA27-Al2O3-Gr hybrid nanocomposites produced by powder metallurgy," *Journal of Composite Materials*, vol. 55, no. 24, pp. 3395–3408, 2021.

[48] P. Shrivastava, S. N. Alam, T. Maity, and K. Biswas, "Effect of graphite nanoplatelets on spark plasma sintered and conventionally sintered aluminum-based nanocomposites developed by powder metallurgy," *Materials Science-Poland*, vol. 39, no. 3, pp. 346–370, 2021.

[49] M. R. Mattli, P. R. Matli, A. Khan et al., "Study of microstructural and mechanical properties of al/sic/tio2 hybrid nanocomposites developed by microwave sintering," *Crystals*, vol. 11, no. 9, p. 1078, 2021.

[50] V. Gholipour, M. Shamanian, A. Ashrafi, and A. Maleki, "Development of aluminium-nanoclay composite by using powder metallurgy and hot extrusion process," *Metals and Materials International*, vol. 27, no. 9, pp. 3681–3694, 2021.

[51] G. Huang, J. Wu, W. Hou et al., F. Meng, A novel two-step method to prepare fine-grained SiC/Al-Mg-Sc-Zr nanocomposite: processing, microstructure and mechanical properties," *Materials Science and Engineering: A*, vol. 823, Article ID 141764, 2021.

Hindawi
Advances in Materials Science and Engineering
Volume 2023, Article ID 8622525, 7 pages
https://doi.org/10.1155/2023/8622525

Research Article

Experimental Studies on Mechanical Behavior of TIG and Friction Stir Welded AA5083 -AA7075 Dissimilar Aluminum Alloys

Veeraiah Goriparthi,[1,2] **Ramanaiah Nallu**,[2] **Rohinikumar Chebolu**,[2] **Sudhakar Indupuri**,[1] **and Ramesh Rudrapati**[3]

[1]*Department of Mechanical Engineering, Maharaj Vijayaram Gajapathi Raj College of Engineering, Vizianagaram 535005, India*
[2]*Department of Mechanical Engineering, A.U. College of Engineering, Andhra University, Visakhapatnam 530003, Andhra Pradesh, India*
[3]*Department of Mechanical Engineering, Bulehora University, Bule Hora, Ethiopia*

Correspondence should be addressed to Ramesh Rudrapati; rameshrudrapati@gmail.com

Received 28 November 2022; Revised 15 December 2022; Accepted 18 March 2023; Published 14 April 2023

Academic Editor: B. Radha Krishnan

Welding is a suitable and better process to manufacture complex objects for aerospace, naval, and automotive structures. Service conditions and complexity in load acting force the manufactures to make joints between dissimilar materials. Thus, there is a need for efficient welding techniques to form sound joints and an understanding of imperfections and their effects. In this study an attempt has been made to study the joining feasibility of dissimilar aluminum alloys by two different welding techniques, namely, tungsten inert gas welding (TIG) and friction stir welding (FSW). Dissimilar AA5083-O and AA7075-T651 aluminum alloys successfully joined by considered welding techniques. Metallurgical and mechanical characteristics of fabricated weld joints are studied at different weld currents (80–120 amp) for TIG and various rotational speeds (800, 1000, 1100, 1200, and 1400 rpm) with constant traverse speed for FSW. Weld joints made by FSW exhibit superior tensile strength, whereas the joint line microhardness of TIG samples is higher than the FSW ones.

1. Introduction

The need for light weight, low cost, high strength, and altered feature materials are the requirement of industries like aerospace, shipbuilding, and transportation. For instance, structures need high resistance against high temperature for some period of time and excellent resistance to corrosion at other times. Similarly, parts need high wear resistance at some areas and excellent strength at some locations. All these mentioned features are satisfied by aluminium alloys. However, due to incompatibility in material properties like physical, chemical, and mechanical, joining of dissimilar materials or aluminum alloys could be a difficult task. Also, because of variation in thermal expansion coefficient and solidus temperature, there is a chance to fail even during the welding process [1, 2]. Fusion-based and solid state welding techniques as well as other processes such as soldering and brazing can be successfully used to join aluminum alloys. Fusion-based techniques like gas tungsten arc welding (GTAW or TIG) and gas metal arc welding (GMAW or MIG), oxy-hydrogen welding, oxy-acetylene welding, air-acetylene welding, and plasma arc welding are used to join aluminum alloys. Among the mentioned techniques, GTAW is the most popular one to join aluminum alloys. However, poor selection of process parameters results in solidification shrinkage, intermetallic phases, formation of intergranular microcracks and stress corrosion cracking, and unpredictable failure of the joints during the service period [3, 4]. Solid state techniques like friction welding, brazing, soldering, explosion welding, ultrasonic welding, diffusion welding and friction stir welding can mitigate the problems that arise in fusion based processes [5]. In the present study two welding

techniques fusion-based (TIG) and solid state welding (FSW) are considered for joining of AA5083 and AA7075 dissimilar aluminum alloys.

GTWA (TIG) welding is fusion-based; an arc welding process developed in the year 1940 to join magnesium and aluminum alloys. GTAW uses a nonconsumable electrode, and an arc is developed between the electrode and the part to be welded. An insulating gas between the electrode and base material is broken down by a high voltage, and then the arc is developed due to the transfer of current through the electrode. The developed arc generates intense heat and joins the part with or without filler material. An inert gas like helium and argon is used to protect the electrode and molten weld pool from oxidation. The welding process parameters (current, welding speed, and shielding gas flow rate) influence the weld bead quality [6].

Friction stir welding (FSW), a novel technique patented by the welding institute, UK, in the year 1991 seems to be the alternative to conventional welding techniques due to the low cost, reduced weight, lower energy consumption, reduced greenhouse gasses, and better metallurgical properties [7]. FSW is an autogenous and continuous hot shearing process that occurs below solidus temperature of materials to be joined. A nonconsumable rotating tool harder than the materials to be joined plunges into the abutting edges of the plates to be joined and moves along the joint line during the welding process. The base material is placed in the direction of the tool velocity vector as the advancing side (AS), and the material placed in the direction opposite to the tool velocity vector as the retreating side (RS). The tool consists of two distinct parts, namely, shoulder and the unique profiled pin. The frictional heat developed due to tool rotation causes severe plastic deformation of base materials. The tool pin extrudes the softened material, and the shoulder forges it and travels along the joint line to complete the joining process [8–11]. Process parameters tool rotational speed, traverse speed, pin profile, tool tilt angle, alloy placement, and axial pressure have significant influence on weld joint quality and mechanical properties. As the FSW is a solid state process, defects present in fusion-based welding processes are eliminated. Fusion welding processes results three zones such as weld zone (WZ), heat affected zone (HAZ), and base material (BM). However, FSW consists of another additional zone, namely, thermomechanical heat affected (TMAZ) between the weld zone called as the weld nugget (NZ) or stir zone (SZ) and HAZ.

2. Literature Review

AA2024-T3 and AA7075-T6 dissimilar aluminum alloys joined by the TIG welding technique using double tungsten electrodes. They concluded that the usage of double electrodes resulted in a stable arc with an excellent weld bead appearance. However, the weld zone microhardness is lower compared to HAZ on the AA7075 alloy side. Maximum weld joint tensile strength is 44% and 37% lower than the strength of AA7075-T6 and AA2024-T3 base alloys, respectively [12]. Similar findings are observed by Sayer et al., who investigated tig and friction stir welded dissimilar AA5083 and AA2014 aluminum alloys. The obtained weld joints are characterized for tensile and hardness distribution. Weld joint tensile strength is lower than the two base alloys considered. Microhardness at the weld zone decreases sharply, which may be attributed to silicon domination in the weld zone [13]. AA5083 and AA6061 dissimilar aluminum alloys joined by the automated pulse tig welding technique with the aim to study the mechanical properties of weld joints. Nonuniform grain size and porosities presence in the weld zone resulted in hardness variation across the weld zone and a strength of the joint lower than the base alloys [14]. Similarly, Waleed and Subbaiah tig welded AA5083-H111 and AA6061-T6 aluminum alloys using ER4047 (silicon rich) filler wire. Due to usage of silicon rich filler, magnesium-silicon precipitates along the AA6061 side of the weld joint. The presence of microcavities and pores in the weld zone leads to minimum weld joint tensile strength and microhardness values [15]. TIG and FSW technique adopted to join the AA7075-T651 and AA6061-Tl dissimilar aluminum alloys. Microstructural examination reveals the presence of microvoids in the weld zone. The maximum weld zone hardness is lower than the considered alloys in both the techniques [16]. AA5083 and AA7075 aluminum dissimilar alloys successfully joined by AC-TIG welding using five different currents (80 amp to 120 amp). Weld joints fabricated at 100 amp current resulted in maximum tensile strength and elongation percentage compared to welds made at other weld currents [17]. Dissimilar AA5383 and AA7075 aluminum alloys successfully joined using friction stir welding (FSW). A tool rotational speed of 700 rpm and traverse speed 40 mm/min resulted in weld joint tensile strength of 211 MPa [18]. Dissimilar AA5754-H111 and AA7075-T651 aluminum alloys were joined with the FSW process. Defect free joint with maximum tensile strength of 239 MPa is achieved when tool traverse and rotational speeds are 80 mm/min and 1000 rpm, respectively [19]. Placing a softer alloy on the advancing side resulted in maximum weld joint tensile strength in the FSW of dissimilar AA5052-H34 and AA7075 aluminum alloys [20]. AA5083-H111 and AA7075-T651 aluminum alloys successfully joined the FSW process. The defect free joint with the maximum tensile strength (371 MPa) obtained for the weld configuration of AS5083-H111 and RS 7075-T651. Weld joint strength decreases with an increase in TRS [21]. Similar observations were found in the FSW of dissimilar AA5083-H111 and AA7075-T651 aluminum alloys [22]. In another study on FSW of AA5083-H111 and AA7075-T651 aluminum alloys, tool traverse speed significantly influenced the joint formation and grain size. High heat generation at lower traverse speed resulted in tunnel defects, whereas higher traverse speeds enhance the joint tensile strength and decreased the stir zone grain size [23].

The literature review shows that weld process parameters significantly influenced the joint formation and tensile strength. Very limited works on AA5083-O and AA7075-T651 dissimilar aluminum alloys presented in open literature. In the present study, an attempt has been made to study the effect of weld process parameters on joint formation and

mechanical properties of TIG and FSW of dissimilar AA5083-O and AA7075-T651 aluminum alloys.

3. Materials and Methods

Two aluminum alloys used in this research AA5083-O and AA7075-T651 were procured from Perfect Metal works, Bangalore, India. The chemical composition of the plates were tested by using a spectroscope and detailed report is presented in Table 1.

Rolled sheets of two considered base alloys AA5083-O and AA7075-T651 are cut into 100 ∗ 75 ∗ 3 size using water jet cutting process. TIG welding is performed at five different weld currents (80 amp–120 amp) using EWM 500 Tetrix 500 AC/DC machine. Friction stir welding (FSW) of base alloys carried on an NC FSW machine (Make: R.V. Machine tools, Coimbatore). Tool rotational speeds 800 rpm, 1000 rpm, 1100 rpm, 1200 rpm, and 1400 rpm with a constant traverse speed 40 mm/min employed for fabrication of weld joints. A straight square probe profile is used for weld joint fabrication. Samples were cut perpendicular to the joint lines of both fabricated plates for metallographic examination. All the samples were prepared as per the standard metallographic procedure and etched with Keller solution for AA7075-T651 and Poulton solution for AA5083-O. All the fabricated joints were characterized for microhardness measurement across the joint line with 1 mm spacing between indentations, 15 s duration, and 500 g indentation force. According to ASTM E8 samples were prepared for tensile testing. Tensile characteristics of all the weld joints were performed on a computerized universal testing machine (Made: INSTRON 8801) with a strain rate of 10^{-1} S^{-1}.

4. Results and Discussion

4.1. Microstructural Analysis. Tensile characterization of all the fabricated joints reveals that joints fabricated at 100 amp weld current in TIG and at 1100 rpm tool rotational speed in FSW exhibited superior joint strength to those welds made at other process parameters. Hence, metallurgical and mechanical characterization conducted for the weld joints showed superior tensile strength. Microstructural examination in the vertical section of weld fabricated at 100 amp current shown in Figures 1 and 2 in a particular direction grain elongation takes place and highly equiaxed grains in the weld center are observed. At the weld top grains are highly elongated, whereas at the bottom, abnormal grain growth resulted due to generation of severe heat during the TIG welding process [17].

Similarly, the macrostructure and stir zone (SZ) microstructure of the weld joint fabricated at 1100 rpm tool rotational speed presented in Figures 3 and 4, respectively. In FSW heat generation directly affects the dissolution of strengthening precipitates and the dynamic recrystallization of base material grains [7–9]. Tool rotational and traverse speed decides the amount of heat generated during the process [20, 24]. Heat generation is minimum at low rotational speed; further fine grains are expected in SZ. Higher tool rotational speeds result in severe heat generation and coarse grains expected. Insufficient and severe heat generation, respectively, at low and high rotational speeds resulted in fine and coarse grains [20, 21, 25, 26]. Microstructural images of the both weld joints shown a variety of grain orientation and size. The fusion zone microstructure of the TIG weld completely differs with SZ microstructure of the FSW joint. This difference could be attributed to the variation in heat input and dynamic recrystalization in the FSW process. Low grain size and an increase in grain boundaries could be the reason for superior join strength in FSW joints compared to the TIG samples.

4.2. Scanning Electron Microscopy Study (SEM). Weld joints fabricated at 100 amp current in TIG and 1100 rpm rotational speed in FSW are characterized for SEM analysis. SEM micrograph presented in Figure 5 supports the microstructural analysis presented in Figure 2 for the weld joint fabricated by fusion welding technique. Dispersoid dissolution in the fusion zone is responsible for superior strength of weld joint produced at 100 amp current. Figure 5 illustrates microconstituents and nodules presence during the solidification weld metal. Secondary segregated microconstituents during weld metal solidification could be due to the magnesium dilution at later stages of the welding process [17]. Thus, it further helps in reducing solidification cracking which confirmed by the absence of a crack at center of the weldment fabricated at 100 amp.

Similarly, Figure 6 depicts the SEM micrograph of the weld joint fabricated at 1100 rpm tool rotational speed. In FSW heat generation is responsible for the strength of the weld joint and proper bonding between the base materials. Friction between the base material and the tool shoulder affects heat generation. Which are further significantly affected by the process parameters such as rotational speed, traverse speed, pin profile, and base materials. However, among the mentioned parameters, tool rotational speed stood first as having influence on heat generation. At lower rotational speed generated heat is not sufficient to solidify the base materials and joint formation [7–9]. On the other hand, at higher tool rotational speeds, excessive heat generation causes overflow of solidified materials and defect formation. Figure 4 shows the formation dispersion and reprecipitates in SZ of the weld joint produced at 1100 rpm. Dissolution of strengthening precipitates in the weld zone could be the reason behind higher joint tensile strength [10, 11].

4.3. MicroHardness. All the weld joints are characterized for microhardness measurement along the joint line and presented in Figure 7. In TIG-welded joints joint-line hardness increases with the weld current. Weld joints made at minimum weld current (80 amp) resulted in a hardness of 115 Hv, whereas, the highest joint line hardness of 138 Hv was obtained for the welds fabricated at 120 amp. It could be

Table 1: Chemical composition of base alloys and electrode used in TIG.

Base alloys and electrodes	Element (in wt. %)								
	Si	Fe	Cu	Mn	Mg	Cr	Zn	Ti	Aluminum
AA7075-T651	0.04	0.15	1.3	0.02	2.3	0.19	5.4	0.05	Balance
AA5083-O	0.09	0.27	0.01	0.8	4.4	0.07	0.02	0.02	Balance
ER5083	0.09	0.27	0.01	0.8	4.4	0.07	0.02	0.02	Balance

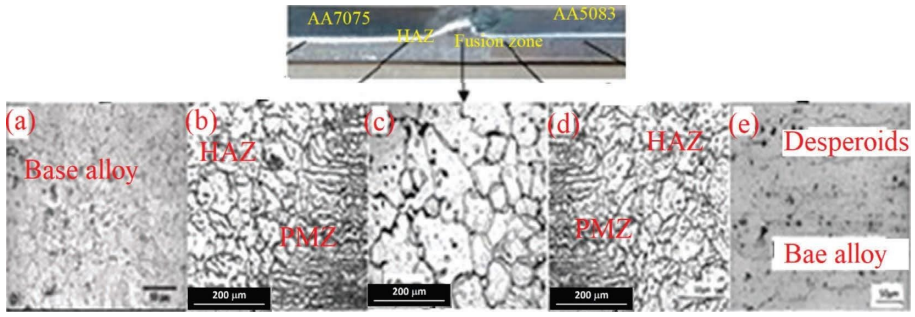

Figure 1: Macrosection of weld joint fabricated at 100 amp.

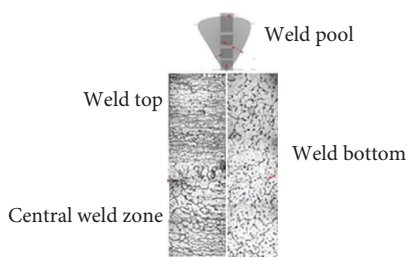

Figure 2: Microstructure of weld fabricated at 100 amp.

Figure 3: Macrostructures of the weld joint fabricated at 1100 rpm.

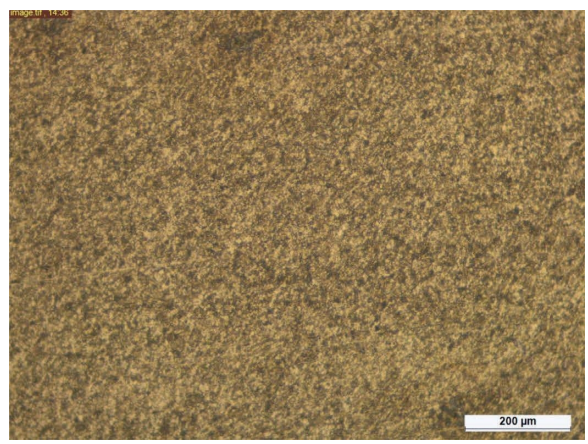

Figure 4: Stir zone microstructure of a weld joint fabricated at 1100 rpm.

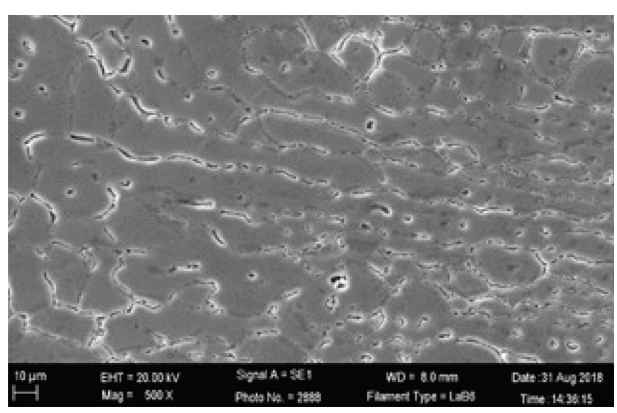

Figure 5: SEM micrograph of the weldment fabricated at 100 amp.

attributed to heat generation during the process resulting in over aging and dissolution of strengthening precipitates [17]. Joint line hardness of FSW samples exhibited lesser values compared to the TIG weld joints. The joint line hardness obtained in all FSW samples is nearly 80 Hv which is almost the same as the base alloy (AA5083-O) hardness. In the FSW tool rotational motion moves the plasticized material from leading to trailing edge. As in the present study the weld configuration is AS 5083 and RS 7075-T651, it confirms that in SZ, the alloy on the advancing side is more dominant [9, 11]. Alloy placement during the FSW process highly affects the hardness distribution and stir zone hardness values [22–26]. In works on similar alloys, the average stir zone hardness is 165 Hv which is almost near to base alloy (AA7075-T651) for the weld configuration AS7075-T651 and RS 5083-O [21]. This could be the reason that the obtained joint line hardness values in FSW samples are lower than the TIG weld joints.

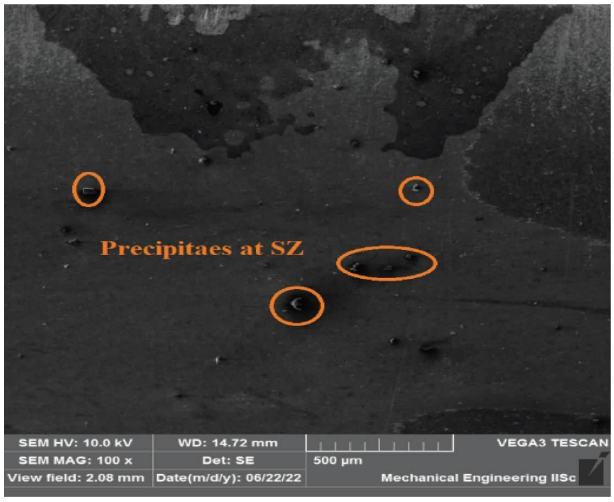

Figure 6: SEM micrograph of the weldment fabricated at 1100 rpm.

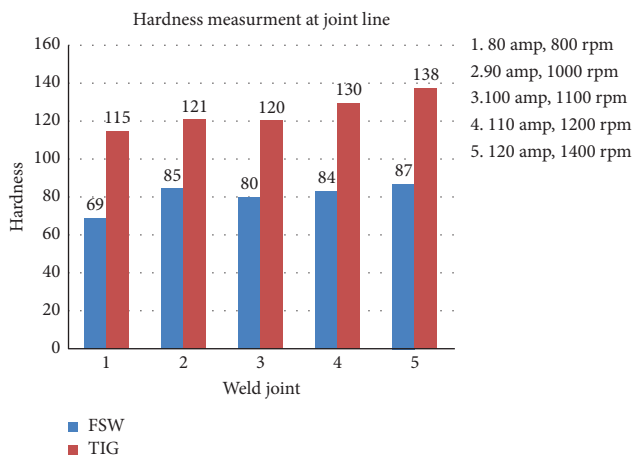

Figure 7: Microhardness at joint line of weldments.

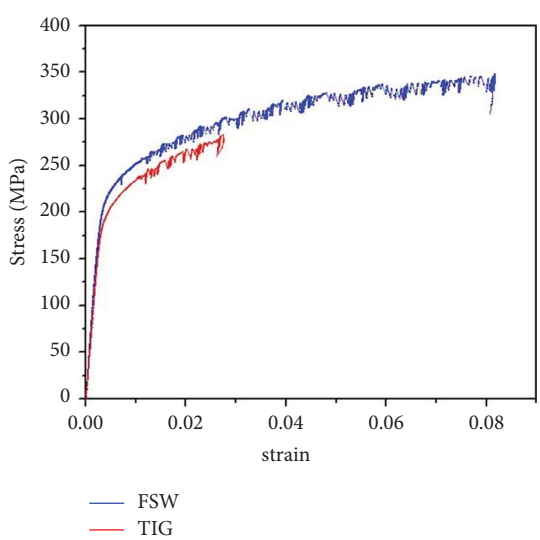

Figure 8: Stress and strain graph for TIG and FSW weld joints.

Table 2: Tensile strength of fabricated weld joints.

FSW tool rotational speed (rpm)	Tensile strength (FSW) in MPa	TIG weld current (amp)	Tensile strength (TIG) in MPa
800	208	80	205
1000	301	90	278
1100	345	100	283
1200	334	110	269
1400	215	120	239

4.4. Tensile Strength. The tensile characterization of the samples fabricated at 100 amp in TIG and 1100 rpm in FSW, as shown in Figure 8 and tensile strength of all the fabricated joints presents in Table 2. Joint tensile strength of 345 MPa and 283 MPa, respectively, obtained for TIG and FSW weld joints. It shows that the strength of FSW joints reaches base alloy (AA5083-O) strength, whereas, the strength of TIG weld joint is lower than the base alloys. In TIG welding temperature during the process is much higher than the recrystallization temperature of the base alloys [17]. Dissolution and strengthening precipitate overaging due to temperature, leads to a decrease in the strength of the joint. In FSW, joining takes place at the solid state because the temperature developed is lower than the melting temperature of base alloys and dynamic recrystallization during the process results in better joint strength. At the lower tool rotational speed, the heat generated is not sufficient to form a sound joint and the higher tool rotational speed generates more heat which further causes a decrease in tensile strength of the weld joint [20–23]. Differences in the strain hardening nature of the base alloys causes fluctuation in the tensile graph. In addition, microdefects like pores and kissing bonds could affect the tensile strength fluctuations.

5. Conclusions

The present study shows that dissimilar AA5083-O and AA7075-T651 aluminum alloys can successfully be joined by TIG and FSW techniques. The following conclusions can be drawn from this investigation.

Weld joints fabricated at 100 amp current in TIG welding resulted in a tensile strength of 283 MPa. Heat input significantly affected the defect formation and tensile joint strength of weld joints. Over aging and grain coarsening affected the joint line hardness. Joints made by the FSW process showed the highest tensile strength of 341 MPa. Defect-free joints can be achieved through FSW with selection of proper process parameters. Joints fabricated at low and high tool rotational speeds resulted with an insufficient and severe heat input, respectively. Insufficient heat input resulted in low tool rotational speeds affected the joint tensile strength. Dissolution and over aging of strengthening precipitates caused minimum strength in TIG welded samples, and dynamic recrystallization resulted in fine and equiaxed grains for the weld joints made with FSW, which showed superior strength.

Data Availability

The data used to support the findings of this study are included within the article.

Conflicts of Interest

The authors declare that there are no conflicts of interest.

References

[1] R. Raja, A. Parthiban, S. Nandha Gopan, and D. Degefa, "Investigate the process parameter on the friction stir welding of dissimilar aluminium alloys," *Advances in Materials Science and Engineering*, vol. 2022, p. 8, 2022.

[2] G. G. Krishna, "Improving joint strength of the friction stir welding of dissimilar aluminium alloy by using coating technique," *Sådhanå*, vol. 47, p. 7, 2022.

[3] M. Nagaaravindaraj, J. Ragavan, B. Muthuselvam, and K. Chandarasekaran, "Influence of process parameters on AA7075 inTIG welding," *International Journal of Advanced Research in Technology, Engineering and Science*, vol. 2, no. 2, pp. 13–18, 2015.

[4] R. Padmanaban, V. Balusamy, and R. Vaira Vignesh, "Effect of friction stir welding process parameters on the tensile strength of dissimilar aluminum alloy AA2024-T3 and AA7075-T6 joints," *Materialwissenschaft und Werkstofftechnik*, vol. 51, no. 1, pp. 17–27, 2020.

[5] R. Rudrapati, "Effects of welding process conditions on friction stir welding of polymercomposites: a review," *Composites Part C: Open Access*, vol. 8, Article ID 100269, 2022.

[6] A. Kumar and S. Sundarrajan, "Optimization of pulsed TIG welding process parameters on mechanical properties of AA 5456 Aluminum alloy weldments," *Materials & Design*, vol. 30, no. 4, pp. 1288–1297, 2009.

[7] Z. Y. Ma, A. H. Feng, D. L. Chen, and J. Shen, "Recent advances in friction stir welding/processing of aluminum alloys: microstructural evolution and mechanical properties," *Critical Reviews in Solid State and Materials Sciences*, vol. 43, no. 4, pp. 269–333, 2017.

[8] R. Palanivel, P. Koshy Mathews, N. Murugan, and I. Dinaharan, "Effect of tool rotational speed and pin profile on microstructure and tensile strength of dissimilar friction stir welded AA5083-H111 and AA6351-T6 aluminum alloys," *Materials & Design*, vol. 40, pp. 7–16, 2012.

[9] C. Hamilton and M. Kopyscianski, "Aleksandra Węglowska, Adam Pietras and Stanisław Dymek, Modeling, microstructure, and mechanical properties of dissimilar 2017A and 5083 aluminum alloys friction stir welds," *Journal of Engineering Manufacture*, vol. 233, no. 2, pp. 1–12, 2017.

[10] P. L. Threadgill, A. J. Leonard, H. R. Shercliff, and P. J. Withers, "Friction stir welding of aluminium alloys," *International Materials Reviews*, vol. 54, no. 2, pp. 49–93, 2009.

[11] M. Ilangovan, S. Rajendra Boopathy, and V. Balasubramanian, "Effect of tool pin profile on microstructure and tensile properties of friction stir welded dissimilar AA 6061–AA 5086 aluminium alloy joints," *Defence Technology*, vol. 11, no. 2, pp. 174–184, 2015.

[12] L. Kaba, M. E. Djeghlal, S. Ouallam, and S. Kahla, "Dissimilar welding of aluminum alloys 2024 T3 and 7075 T6 by TIG process with double tungsten electrodes," *The International Journal of Advanced Manufacturing Technology*, vol. 118, no. 3-4, pp. 937–948, 2022.

[13] S. Sayer, C. Yeni, and O. Ertugrul, "Comparison of mechanical and microstructural behaviors of tungsten inert gas welded and friction stir welded dissimilar aluminum alloys AA 2014 and AA 5083," *Metallic Materials*, vol. 49, no. 2, pp. 155–162, 2011.

[14] P. K. Baghel and D. S. Nagesh, "Mechanical properties and microstructural characterization of automated pulse TIG welding of dissimilar aluminum alloy," *Indian Journal of Engineering and Materials Sciences*, vol. 25, pp. 147–154, 2018.

[15] W. A. Waleed and K. Subbaiah, "E ect of ER4047 filler rod on tungsten inert gas welding of AA5083-H111 and AA6061-T6 aluminum alloys," *Journal of Chemical and Pharmaceutical Sciences*, vol. 7, pp. 210–213, 2017.

[16] C. Patil, H. Patil, and H. Patil, "Experimental investigation of hardness of FSW and TIG joints of Aluminium alloys of AA7075 and AA6061," *Frattura Ed Integrità Strutturale*, vol. 10, no. 37, pp. 325–332, 2016.

[17] G. Veeraiah, N. Ramanaiah, I. Sudhakar, and K. Venkateswarlu, *Influence of AC-TIG weld Current on Dissimilar AA5083 and AA 7075 Aluminium alloy*, 2022.

[18] S. Sivachidambaram, G. Rajamurugan, and D. Amirtharaj, "Optimizing the parameters for friction stir welding of dissimilar aluminium alloys AA5383/AA7075," *ARPN Journal of Engineering and Applied Sciences*, vol. 10, pp. 5434–5437, 2015.

[19] S. Kasman and Z. Yenier, "Analyzing dissimilar friction stir welding of AA5754/AA7075," *The International Journal of Advanced Manufacturing Technology*, vol. 70, no. 1-4, pp. 145–156, 2014.

[20] A. Z. Ahmed, M. K. Abbass, A. H. Ataiwi, S. K. Khanna, B. Jashti, and C. Widener, "Investigation of fatigue behavior and fractography of dissimilar friction stir welded joints of aluminum alloys 7075-T6 and 5052-H34," *International Journal of Materials Science and Engineering*, vol. 2, pp. 115–121, 2014.

[21] I. Kalemba-Rec, M. Kopyściański, D. Miara, and K. Krasnowski, "Effect of process parameters on mechanical properties of friction stir welded dissimilar 7075-T651 and 5083-H111 aluminum alloys," *The International Journal of Advanced Manufacturing Technology*, vol. 97, no. 5-8, pp. 2767–2779, 2018.

[22] I. Kalemba-Rec, C. Hamilton, M. Kopyściański, D. Miara, and K. Krasnowski, "Microstructure and mechanical properties of friction stir welded 5083 and 7075 aluminum alloys," *Journal of Materials Engineering and Performance*, vol. 26, no. 3, pp. 1032–1043, 2017.

[23] M. Saeidi, B. Manafi, M. Besharati Givi, and G. Faraji, "Mathematical modeling and optimization of friction stir welding process parameters in AA5083 and AA7075 aluminum alloy joints," *Proceedings of the Institution of Mechanical Engineers - Part B: Journal of Engineering Manufacture*, vol. 230, no. 7, pp. 1284–1294, 2016.

[24] M. Ramamurthy, P. Balasubramanian, N. Senthilkumar, and G. Anbuchezhiyan, "Influence of process parameters on the microstructure and mechanical properties of friction stir welds of AA2014 and AA6063 aluminium alloys using response surface methodology," *Materials Research Express*, vol. 9, no. 2, p. 026528, 2022.

[25] R. Madhusudhan, M. M. M. Sarcar, N. Ramanaiah, and K. PrasadaRao, "An experimental study on the effect of weld parameters on mechanical and micro structural properties of dissimilar aluminium alloy FS welds," *International Journal of Modern Engineering Research (IJMER)*, vol. 2, no. 4, pp. 1459–1463.

[26] R. Raja, A. Parthiban, S. Jeyakumar, and B. Radha Krishnan, "Investigation of mechanical properties of friction stir welding aluminium alloy AA7475-T651 and AA2219-O," *Materials Today: Proceedings*, vol. 60, pp. 1421–1423, 2022.